Integrating Enhancement Techniques for Thin-Film Silicon Solar Cells

A methodic approach to efficiency optimization

Olav Eringfeld

Delft University of Technology

TU Delft

Integrating Enhancement Techniques for Thin-Film Silicon Solar Cells

A methodic approach to efficiency optimization

Master thesis report for Sustainable Energy Technology

by

Olav Eringfeld

to obtain the degree of Master of Science
at the Delft University of Technology,
to be defended publicly on Monday May 27th, 2024 at 15:30 AM.

Student number:	4560981	
Project duration:	August 12, 2023 – May 27, 2024	
Thesis committee:	Prof. dr. ir. J. A.(Arno)H.M.Smets,	TU Delft, supervisor
	Dr.ir. R.(Rudi) van Santbergen	TU Delft
	Dr.ir. D.(Dennis) van der Born,	TU Delft
Daily supervisor:	ir. G.(Govind) Padmakumar	TU Delft

An electronic version of this thesis is available at `http://repository.tudelft.nl/`.

Faculty of Electrical Engineering, Mathematics & Computer Science

Else Kooi Laboratory

TU Delft

PVMD Delft University of Technology

HyET Solar Flexible light weight solar modules

Acknowledgement

Over the last 9 months, I have spent a lot of time and effort trying to contribute to the scientific community by helping in the development of an innovative solar cell concept. In this thesis, only a part of the total amount of experiments, measurements and discussion are shown and executing the experiments has not always gone without setbacks. The work shown in this thesis would not have been possible without the help and support of my supervisor, Arno Smets, who has always been available for feedback and discussions and has provided me with a lot of knowledge. I also want to thank Govind Padmakumar for providing me with the know-how on operating the equipment in EKL and the measurement setups in the ESP lab and the countless discussions we have had on the experiments. Furthermore, I want to thank Paula Perez Rodriguez, Sreejith Koorthedath Pullayikody and Federica Saitta for the time and knowledge they shared with me during the experiments we performed. I want to thank Martijn Tijssen, Tim Velzeboer, Stefaan Heirman, Bernardus Zijlstra and Engin Özkol for all their help with fixing errors on equipment, broken machinery and help with learning all the equipment in the EKL laboratory and the ESP lab. I would also like to thank all my fellow master's thesis students for the time we have worked together as part of the PVMD group. I would also like to take time to express my gratitude towards my parents and my brother for their continuous support during my time at TU Delft to help me finish my master's degree. Finally, I would like to thank Rudi Santbergen and Dennis van der Born for making time to take part in my thesis committee.

Delft, 27th of May 2024
Olav Florens Rudolph Eringfeld

Abstract

Renewable energy sources, such as thin-film silicon solar cells, show a lot of potential as the technology promises low production temperatures, low cost and low material usage. Other benefits are the flexible and very lightweight modules that can be fabricated, which enable a wide variety of applications. Other benefits include the low-temperature coefficient and low toxicity of the materials used to create thin-film silicon solar cells. The downside of using thin-film silicon modules is the relatively low power conversion efficiency inherent to the amorphous and nanocrystalline silicon. Another downside of amorphous silicon solar cells is their significant initial degradation, known as the Staebler-Wronski effect. This initial degradation will stabilize after time but does limit the ultimate conversion efficiency, especially for single-junction devices.

Hydrogenated amorphous silicon (a-Si:H) and nano-crystalline silicon (nc-Si:H) solar cells can be added in series to form a tandem device, thus increasing the efficiency of thin-film silicon solar cells. Although the current will be limited for 2-terminal tandem devices, a significant increase in open circuit voltage can be achieved resulting in higher efficiencies. To achieve highly efficient thin-film silicon solar cells a combination of good optical, electrical and material properties need to be combined. Extensive research has been done to achieve such high-efficiency devices focussed on the silicon deposition conditions, glass texturing for effective light scattering and light incoupling through anti-reflection coatings. Further research is focused on Transparent Conductive Oxides (TCO) improvements and the creation of triple or quadruple junctions.

Firstly, this thesis will focus on a literature study on amorphous silicon with a high-energy bandgap, deposition conditions in PECVD chambers and an i-SiO_x buffer layer. A top cell of amorphous silicon with a high-energy bandgap can improve the conversion efficiency of a-Si:H/nc-Si:H solar cells by increasing its overall V_{oc}. The amorphous silicon is processed at high pressure (3-9$mbar$) and high power densities (150-400mW/cm^2) in a VHF-PECVD chamber at 40.68MHz. To improve the poor blue response of these solar cells, a buffer layer of i-SiO_x is explored as such a buffer layer has proven itself under normal deposition power densities (28mW/cm^2) and pressure (0.7$mbar$).The i-SiO_x did not prove to be effective in improving the blue response. A narrow range of deposition conditions around 5$mbar$ and 25W is found to give high-bandgap energy solar cells with a good blue response.
Secondly, literature findings on a bilayer TCO configuration of IOH (Hydrogenated Indium Oxide) and i-ZnO (intrinsic Zinc-Oxide) to improve nc-Si:H single junction solar cells are provided. Prior studies on the use of a back reflector made out of different ZnO(Zinc-Oxides) are presented. Findings in literature on micro and nano-textured glass are presented and a comparison is made in an experiment to justify the use of a specific texture. Further experiments are carried out to measure the effect of implementing the bilayer TCO and an i-ZnO back reflector and an experiment on the performance and reproducibility of a-Si on MST (modulated surface textured) glass substrates is performed. ITO textured glass is chosen as the best performing substrate and a thick 1μ i-ZnO layer as part of a bilayer TCO is shown to be most effective at light scattering. The i-ZnO as part of a bilayer TCO can also significantly improve the spectral response of a-Si:H solar cell on MST textured glass. Furthermore, the i-ZnO as a back reflector is shown to be more effective when its thickness is increased.
Thirdly, a study is performed on the functioning of the a-Si:H/nc-Si:H tandem cells with respect to the thickness of the p-layer in the tunnel recombination junction (TRJ). An experiment is carried out to improve the reproducibility of a-Si:H/nc-Si:H solar cells by increasing the thickness of p-layer in the TRJ. The conclusion is made that the glass texturing is more influential than the thickness of the p-layer in this experiment. Further investigation of the p-layer at the front interface of the device is done by an experiment on both MST and Asahi substrates. It is shown that thicker front p-layers do not improve the reproducibility of tandem solar cells, but a trend of more parasitic absorption is seen. Finally, a study on micro and nano-textured glass for a-Si:H/nc-Si:H solar cells is shown. The chosen ITO substrate is finally chosen to demonstrate the progress of ongoing research on the performance of a-Si:H/nc-Si:H solar cells. The bilayer TCO vs a single layer TCO is used in combination with and without a SiN_x ARC. The electrical performance of the solar cells deposited in the final experiment is likely limited by poor IOH depositions and a large contribution of parasitic absorption is shown for the samples with the SiN_x ARC. Either interaction of SiN_x with the IOH or a poor IOH deposition are the most likely causes. Good 1-R curves are obtained for the solar cells on ITO textured glass substrates, especially the sample with the bilayer TCO and SiN_x ARC.

Contents

List of Figures vi

List of Tables x

1 Introduction 1
- 1.1 The need for solar energy . . . 1
- 1.2 Motivation for thin-film silicon solar cells . . . 2
- 1.3 The goal of this research . . . 3
- 1.4 Structure of the report . . . 4

2 Fundamentals of silicon solar cells 5
- 2.1 Fundamental principles . . . 5
  - 2.1.1 Light . . . 5
  - 2.1.2 Solar spectrum . . . 5
  - 2.1.3 Semiconductor physics . . . 6
  - 2.1.4 Electromagnetic waves and optics . . . 11
- 2.2 The fundamental working principle of a solar cell . . . 13
  - 2.2.1 Absorption, generation, separation and collection . . . 13
  - 2.2.2 Equivalent circuit of a solar cell . . . 14
- 2.3 Thin film solar cells . . . 15
  - 2.3.1 a-Si:H . . . 15
  - 2.3.2 nc-Si:H . . . 16
- 2.4 Tandem solar cells . . . 17
- 2.5 Losses and recombination . . . 18
  - 2.5.1 Losses in solar cells and recombination processes . . . 18
- 2.6 Thin film processing techniques . . . 18
  - 2.6.1 Glass texturing . . . 18
  - 2.6.2 Plasma Enhanced Chemical Vapour Deposition (PECVD) . . . 19
  - 2.6.3 Magnetron Sputtering . . . 20
  - 2.6.4 Electron Beam Evaporation & Thermal Evaporation . . . 20
- 2.7 Characterisation methods . . . 21
  - 2.7.1 JV characterisation . . . 21
  - 2.7.2 External Quantum Efficiency (EQE) measurement . . . 22
  - 2.7.3 Reflectance measurement . . . 24
  - 2.7.4 Raman spectroscopy . . . 24
  - 2.7.5 Spectral Ellipsometry . . . 25
  - 2.7.6 Scanning Electron Microscope (SEM) . . . 25
- 2.8 Solar cell design . . . 26

3 High-bandgap hydrogenated amorphous silicon solar cell depositions by VHF-PECVD 28
- 3.1 Literature review . . . 28
  - 3.1.1 High bandgap amorphous silicon solar cells . . . 28
  - 3.1.2 Record a-Si:H/nc-Si:H solar cells . . . 28
  - 3.1.3 Ion bombardment . . . 29
  - 3.1.4 Intrinsic Silicon-oxide buffer layer . . . 30
- 3.2 Experiments . . . 30
  - 3.2.1 Very high-frequency processing of high-bandgap amorphous silicon solar cells . . . 30
  - 3.2.2 experiment 1: buffer layer thickness between p-i interface . . . 31
  - 3.2.3 experiment 2: power and pressure series . . . 32

3.3 Results and discussion . . . 33
3.3.1 Very high-frequency processing of high bandgap amorphous silicon solar cells . . 33
3.3.2 Series 1 of experiment 2, power and pressure series for high bandgap a-Si:H solar cells processed in a VHF-PECVD chamber. . . . 35
3.3.3 Series 2 of experiment 2, power and pressure series for high bandgap a-Si:H solar cells processed in a VHF-PECVD chamber. . . . 38
3.3.4 Series 3 of experiment 2, power series for high bandgap a-Si:H solar cells processed in a VHF-PECVD chamber. . . . 40
3.4 conclusion . . . 41

4 High-efficiency single junction a-Si:H and nc-Si:H solar cells for tandem applications 42
4.1 Literature review . . . 42
4.1.1 Micro and nano-features on glass substrates . . . 42
4.1.2 Record a-Si:H/nc-Si:H solar module . . . 43
4.1.3 IOH and i-ZnO as Bilayer TCO . . . 43
4.1.4 i-ZnO as back reflector . . . 43
4.2 Experiments . . . 43
4.2.1 Experiment 3: Micro and nano-textured glass substrates for nc-Si:H solar cells . . 44
4.2.2 Experiment 4: Shunt and front TCO configuration for a-Si:H solar cells on MST textured glass substrates. . . . 45
4.2.3 Experiment 5: Thickness of i-ZnO as part of a bilayer TCO for nc-Si:H solar cells on MST textured glass substrates . . . 46
4.2.4 Experiment 6: Thickness variation of an i-ZnO back reflector for nc-Si:H solar cells on MST textured glass substrates . . . 47
4.3 Results and discussion . . . 48
4.3.1 Experiment 3: Micro and nano-textured glass substrates for nc-Si:H solar cells. . . 48
4.3.2 Experiment 4: Shunt and front TCO configuration for a-Si:H solar cells on MST textured glass substrates. . . . 51
4.3.3 Experiment 5: Thickness of i-ZnO as part of a bilayer TCO for nc-Si:H solar cells on MST textured glass substrates . . . 53
4.3.4 Experiment 6: Thickness variation of an i-ZnO back reflector for nc-Si:H solar cells on MST textured glass substrates . . . 55
4.4 conclusion . . . 57

5 Efficiency and reproducibility improvements of a-Si:H/nc-Si:H tandem solar cells 59
5.1 Literature review . . . 59
5.1.1 Silicon oxide tunnel recombination junction . . . 59
5.1.2 Texture for a-Si:H/nc-Si:H tandem solar cells . . . 59
5.1.3 Anti-reflection coating . . . 59
5.2 Experiments . . . 60
5.2.1 Experiment 7: p-SiO_x thickness in the Tunnel Recombination Junction of a-Si:H/nc-Si:H solar cells on MST textured glass substrates . . . 60
5.2.2 Experiment 8: Front p-SiO_x thickness MST vs Asahi comparison . . . 61
5.2.3 Experiment 9: Anti-reflection coating and bilayer comparison of a-Si:H/nc-Si:H solar cell comparison on ITO textured glass substrates . . . 62
5.3 Results and discussion . . . 63
5.3.1 Experiment 7: p-SiO_x thickness in the Tunnel Recombination Junction of a-Si:H/nc-Si:H solar cells on MST textured glass substrates . . . 63
5.3.2 Experiment 8: Front p-SiO_x thickness MST vs Asahi comparison . . . 65
5.3.3 Experiment 9: Anti-reflection coating and bilayer comparison of a-Si:H/nc-Si:H solar cell comparison on ITO textured glass substrates . . . 68
5.4 conclusion . . . 73
5.5 recommendations . . . 74

References **78**

A Appendix A - JV-curves **78**

B Appendix B - Processing parameters **81**
B.1 Chapter 1 experiments . . . 81
B.1.1 Experiment 1 . . . 81
B.1.2 Experiment 2 . . . 81
B.2 Chapter 2 experiments . . . 82
B.2.1 Experiment 3 . . . 82
B.2.2 Experiment 4 . . . 82
B.2.3 Experiment 5 . . . 83
B.2.4 Experiment 6 . . . 83
B.3 Chapter 3 experiments . . . 84
B.3.1 Experiment 7 . . . 84
B.3.2 Experiment 8 . . . 85
B.3.3 Experiment 9 . . . 86

C Appendix C - Anti-reflection coating parameters **87**
C.1 Data SiN_x . . . 87
C.1.1 n (refractive index) data . . . 87
C.1.2 k (extinction coefficient) data . . . 87

D Appendix D - Normalised Raman spectroscopy plots **88**
D.0.1 Normalised Raman plots Experiment 3 . . . 88
D.0.2 Normalised Raman plots Experiment 5 . . . 90
D.0.3 Normalised Raman plots Experiment 6 . . . 92
D.0.4 Normalised Raman plots Experiment 7 . . . 93
D.0.5 Normalised Raman plots Experiment 8 . . . 95
D.0.6 Normalised Raman plots Experiment 9 . . . 98

E Appendix E - Images **101**
E.0.1 Image of the MST textured samples next to the Asahi samples from experiment 8. 101

List of Figures

1.1 A depiction of how global warming is related to anthropogenic (man-made) emissions from the IPCC (International Panel for Climate Change [1]. . . . 1
1.2 A depiction of anthropogenic (man-made) emissions from the IPCC (International Panel for Climate Change) [1]. . . . 2
1.3 A comparison of the total finite (fossil) energy sources and yearly potential of renewable energy sources [11]. . . . 2
1.4 An artist render of Hyet thin-film silicon modules on a Vopak terminal [17] 3
1.5 An artist render of HYET thin-film silicon modules compared to c-Si modules on a rooftop [19] 3

2.1 The solar spectrum AM0 and AM1.5G and AM1.5D from [22]. . . . 6
2.2 The structure of crystalline Silicon from [21]. . . . 6
2.3 The structure of n-type crystalline Silicon (a) and p-type crystalline Silicon (b) from [21]. 7
2.4 Density of states for a single hydrogen atom (a), two hydrogen atoms close to each other (b) and the splitting of the n1 state (c) from [23]. . . . 7
2.5 Splitting of the quantized energy level into discrete energy states around r_0, the equilibrium interatomic distance [23]. . . . 8
2.6 Simplified splitting of the three energy levels into discrete energy states around r_0, the equilibrium interatomic distance [23]. . . . 8
2.7 Splitting of the quantized energy levels into discrete energy states around a_0, the equilibrium interatomic distance [23]. . . . 9
2.8 Simplified bandgap of a n-type semiconductor (a) and a p-type semiconductor (b)[23]. . 10
2.9 Space charge region in a PN junction[23]. . . . 10
2.10 Band diagram of a PN junction[23]. . . . 11
2.11 Snell's law from [21]. . . . 12
2.12 A band diagram of a PN junction semiconductor. . . . 13
2.13 Generation, separation and collection of charge carriers from [21]. . . . 14
2.14 The equivalent circuit of a solar cell, including shunt and series resistances from [21]. . 14
2.15 The absorption coefficient for a-Si:H, nc-Si:H (here shown as μc-Si) and c-Si [24]. . . . 15
2.16 The atomic structure of Crystalline silicon, amorphous silicon and hydrogenated amorphous silicon from [25] 16
2.17 The bandgap of Amorphous silicon [27] 16
2.18 Growth of nc-Si:H from [29]. . . . 17
2.19 Spectral utilisation of a micromorph solar cell, note that the a-Si:H has higher spectral utilisation when compared to the nc-Si:H (dashed line) [30]. . . . 17
2.20 Schematic representation of Asahi VU, ITO and MST glass texture used throughout this thesis 19
2.21 Schematic representation of a PECVD chamber and its components [33]. . . . 20
2.22 Schematic representation of a Magnetron Sputtering chamber and its components [33]. 20
2.23 Schematic representation of the PVD techniques in the Provac tool. . . . 21
(a) Schematic representation of Electron Beam Evaporation [34]. . . . 21
(b) Schematic representation of Thermal Evaporation [34]. . . . 21
2.24 An example of an IV curve under breakdown voltage, reverse bias and forward bias [35]. 22
2.25 A typical JV curve with power density P on a second y-axis for c-Si solar cells for illustration purposes [36]. . . . 22
2.26 Schematic example of an EQE setup [37]. . . . 23
2.27 Bias voltages in a tandem solar cell, where the white circle indicates the voltage over the entire cell and the white square indicates the reverse bias on the current limiting cell [38]. 24
2.28 An illustration of the basic principle of Spectral Ellipsometry 25
2.29 A schematic cross-section of a Scanning Electron Microscope [42]. . . . 26
2.30 ITO textured thin-film silicon solar cell 27
2.31 Different levels op dopant concentration for the p-nc-SiOx layers on a Asahi substrate . 27
2.32 A schematic cross-section of the solar cell back contacts 27

3.1 A schematic cross-section of the record module sized a-Si:H/nc-Si:H cell developed at TEL [44]. . . . 29
3.2 A bimodal distribution, which can be applied to the ion energy distribution of RF- and VHF-PECVD chambers [46]. . . . 30
3.3 A comparison of the spectral response of a low-bandgap a-Si:H single junction and a tandem cell of a low-bandgap a-Si:H top cell and a nc-Si:H bottom cell, both processed on Asahi Vu substrates. . . . 31
3.4 A schematic cross-section of the a-Si single junction device structure used in the VHF deposition . . . 31
3.5 A schematic cross-section of a the p-i interface with an i-SiO_x buffer in (a) and without an i-SiO_x buffer layer in (b). . . . 32
(a) . . . 32
(b) . . . 32
3.6 The EQE of a high power and pressure deposition, showcasing the poor blue response. 34
3.7 The EQE and 1-R measurements of the samples with increasing i-SiO_x buffer layer thicknesses. . . . 35
3.8 Plasma state based on visual observations where ”Good plasma”, ”Flickering plasma” and ”no plasma” are indicators . . . 36
3.9 EQE and 1-R measurements of the [9$mbar$/40W],[8$mbar$/30W] and [7$mbar$/30W] samples from series 1. . . . 37
3.10 EQE and 1-R measurements of the [6$mbar$/25W],[5$mbar$/20W],[4$mbar$/20W] and [3$mbar$/15W] samples from series 1. . . . 38
3.11 EQE and 1-R measurements of the [7$mbar$/35W] and [6$mbar$/30W] samples from series 2. . . . 39
3.12 EQE and 1-R measurements of the [5$mbar$/25W],[4$mbar$/25W] and [3$mbar$/20W] samples from series 2. . . . 40
3.13 EQE and 1-R measurements of the [5$mbar$/20W],[5$mbar$/25W] and [5$mbar$/28W] samples from series 3. . . . 41

4.1 The textures with nano-features (EAZO), micro-feature (EG) and double texture (MST) and their parameters used by Tan et al. [4]. . . . 43
4.2 Top down AFM (Atomic force measurement) and SEM (Scanning Electron Microscope) images of the ITO,i-ZnO and MST texture used, not that the scale on the i-ZnO AFM is twice as small as on the ITO or MST textures [54] . . . 44
4.3 A schematic cross-section of the nc-Si:H solar cell design used in experiment 3. . . . 45
4.4 A cross-section of the shunted a-Si:H solar cell with a possible shunt location shown by the red arrow. . . . 46
4.5 A schematic cross-section of the a-Si:H solar cell design used in experiment 4 . . . 46
4.6 A schematic cross-section of the nc-Si:H solar cell design used in experiments 5 and 6 47
4.7 JV curves of the MST, i-ZnO and ITO textures from experiment 3. . . . 49
4.8 EQE measurements of the MST, i-ZnO and ITO textures from experiment 3. . . . 50
4.9 EQE measurements together with -2V reverse bias of the MST, i-ZnO and ITO textures from experiment 3. . . . 51
4.10 JV curves of the a-Si:H solar cells on MST textured glass substrates with different i-ZnO thickness as part of bilayer TCO from experiment 4. . . . 52
4.11 EQE measurements of the a-Si:H solar cells on MST textured glass substrates with different i-ZnO thickness as part of bilayer TCO from experiment 4. . . . 53
4.12 JV curves of the nc-Si:H solar cells on MST textured glass substrates with different i-ZnO thickness as part of bilayer TCO from experiment 5. . . . 54
4.13 EQE measurements of the nc-Si:H solar cells on MST textured glass substrates with different i-ZnO thickness as part of bilayer TCO from experiment 5. . . . 55
4.14 JV curves of the nc-Si:H solar cells on MST textured glass substrates with different back reflector thickness experiment 6. . . . 56
4.15 EQE measurements of the nc-Si:H solar cells on MST textured glass substrates with different back reflector thickness of experiment 6. . . . 57

5.1 A schematic cross-section of the refractive index grading of a glass, SiN_x and IOH stack. 60
5.2 A schematic cross-section of the a-Si:H/n-Si:H solar cell used in experiment 7. 61
5.3 A schematic cross-section of the a-Si:H/nc-Si:H solar cell used in experiment 8, note that the same design was applied on the Asahi substrates. 62
5.4 A schematic cross-section of the a-Si:H/nc-Si:H solar cell design used in experiment 9, note the SiN_x is not shown between the glass and IOH interface as not all samples have the anti-reflection coating. 63
5.5 JV curves of the a-Si:H/nc-Si:H solar cells with p-window (TRJ) thickness variations of experiment 7. 64
5.6 EQE measurements of the a-Si:H/nc-Si:H solar cells with p-window (TRJ) thickness variations of experiment 7 65
5.7 EQE measurements of the Asahi substrates with varying front p-layer thickness. 66
5.8 EQE measurements of the MST substrates with varying front p-layer thickness. 67
5.9 EQE measurements of the reference cell on an Asahi substrate from the same run. . . 67
5.10 JV curves of the a-Si:H/nc-Si:H solar cells from experiment 9. 68
5.11 EQE measurements of the a-Si:H/nc-Si:H solar cell on an ITO textured glass substrate with a bilayer TCO. 69
5.12 EQE measurements of the a-Si:H/nc-Si:H solar cell on an ITO textured glass substrate with a bilayer TCO and the SiN_x ARC. 70
5.13 EQE measurements of the a-Si:H/nc-Si:H solar cell on an ITO textured glass substrate with a monolayer IOH TCO. 71
5.14 EQE measurements of the a-Si:H/nc-Si:H solar cell on an ITO textured glass substrate with a monolayer IOH TCO and the SiN_x ARC. 72
5.15 The 1-R curves of the a-Si:H/nc-Si:H solar cells on ITO textured glass, with monolayer, bilayer and with and without the SiN_x ARC. The 1-R of the Asahi reference cell is also shown as a comparison. 73

A.1 JV-curves of the Asahi substrates with varying front p-layer thickness from experiment 8. 78
A.2 JV-curves of the MST substrates with varying front p-layer thickness from experiment 8. 79
A.3 JV-curve of the reference a-Si:H/nc-Si:H tandem cell from the run in which experiment 8 was done. 79
A.4 JV-curve of the reference a-Si:H/nc-Si:H tandem cell from the run in which experiment 9 was done. 80
A.5 EQE-measurement of the reference a-Si:H/nc-Si:H tandem cell from the run in which experiment 8 was done. 80

C.1 N data and the target line as the black dotted line, measured by Leo Adachi on the SiN_x. 87
C.2 K data and the target line as the black dotted line, measured by Leo Adachi on the SiN_x. 87

D.1 Normalised Raman plot of ITO texture from experiment 3. 88
D.2 Normalised Raman plot of iZnO texture from experiment 3. 88
D.3 Normalised Raman plot of MST texture from experiment 3. 89
D.4 Normalised Raman plot of the extra MST texture from experiment 3. 89
D.5 Normalised Raman plot of the 500nm iZnO sample from experiment 5. 90
D.6 Normalised Raman plot of the 1000nm iZnO sample from experiment 5. 90
D.7 Normalised Raman plot of the 1500nm iZnO sample from experiment 5. 91
D.8 Normalised Raman plot of the 2000nm iZnO sample from experiment 5. 91
D.9 Normalised Raman plot of the 60nm iZnO as back reflector sample from experiment 6. 92
D.10 Normalised Raman plot of the 2400nm iZnO as back reflector sample from experiment 6. 92
D.11 Normalised Raman plot of the 500nm iZnO as back reflector sample from experiment 6. 93
D.12 Normalised Raman plot of the 14nm p-layer in the TRJ sample from experiment 7. . . . 93
D.13 Normalised Raman plot of the 18nm p-layer in the TRJ sample from experiment 7. . . . 94
D.14 Normalised Raman plot of the 22nm p-layer in the TRJ sample from experiment 7. . . . 94
D.15 Normalised Raman plot of the 1x front p-layer on Asahi from experiment 8. 95
D.16 Normalised Raman plot of the 1x front p-layer on MST from experiment 8. 95
D.17 Normalised Raman plot of the 1.5x front p-layer on Asahi from experiment 8. 96
D.18 Normalised Raman plot of the 1.5x front p-layer on MST from experiment 8. 96

D.19 Normalised Raman plot of the 2x front p-layer on Asahi from experiment 8. 97
D.20 Normalised Raman plot of the 2x front p-layer on MST from experiment 8. 97
D.21 Normalised Raman plot of ITO texture with bilayer TCO from experiment 9. 98
D.22 Normalised Raman plot of ITO texture with bilayer and ARC TCO from experiment 9. . 98
D.23 Normalised Raman plot of ITO texture with single layer TCO from experiment 9. 99
D.24 Normalised Raman plot of ITO texture with single layer TCO and ARC from experiment 9. 99
D.25 Normalised Raman plot of reference a-Si:H/nc-Si:H cell on Asahi from experiment 9. . . 100

E.1 Image showing a metallic like deposition on the front side of the MST textured substrates from experiment 8. 101

List of Tables

3.1 Table with the processing conditions for the i-SiO_x buffer layer of the samples with different i-SiO_x thickness buffer layers. . . . 32
3.2 Table with the processing conditions for the intrinsic amorphous silicon absorber layer of the samples with different i-SiO_x thickness buffer layers. . . . 32
3.3 Table with the processing conditions for the intrinsic amorphous silicon absorber layer of series 1 of experiment 2. . . . 33
3.4 Table with the processing conditions for the intrinsic amorphous silicon absorber layer of series 2 and 3 of experiment 2. . . . 33
3.5 Table with an overview of the processing conditions and key electrical parameters obtained from experiment 1. . . . 34
3.6 Table with an overview of the processing conditions of series 1 of experiment 2. . . . 36
3.7 Table with an overview of the electrical performance of Series 1. . . . 37
3.8 Table with an overview of the processing conditions of series 2 of experiment 2. . . . 38
3.9 Table with an overview of the electrical performance of Series 2. . . . 39

4.1 Table with an overview of the processing conditions of the i-ZnO layer used in Chapter 2. 44
4.2 Table with an overview of the processing conditions of the i-nc-Si:H absorber layer used for the texture experiment 3. . . . 44
4.3 Table with an overview of the processing conditions of the i-a-Si:H absorber layer used for the texture experiment 4. . . . 46
4.4 Table with an overview of the processing conditions of the i-nc-Si:H absorber layer used for the texture experiment 5. . . . 47
4.5 Table with an overview of the processing conditions of the i-nc-Si:H absorber layer used for the texture experiment 6. . . . 47
4.6 Table with an overview of the processing conditions and key electrical parameters obtained from experiment 1, the X is crystallinity in % and η shows the efficiency. . . . 48
4.7 Table with an overview of the key electrical parameters obtained from $0V$ bias and $-2V$ reverse bias (RB) measurements of samples from experiment 3, the X is crystallinity in % and η shows the efficiency. . . . 50
4.8 Table with an overview of the key electrical parameters obtained measurements of samples from experiment 4, η shows the efficiency. . . . 51
4.9 Table with an overview of the key electrical parameters obtained measurements of samples from experiment 5, the X is crystallinity in % and η shows the efficiency. . . . 54
4.10 Table with an overview of the key electrical parameters obtained measurements of samples from experiment 6, the X is crystallinity in % and η shows the efficiency. . . . 55

5.1 Table with an overview of the processing conditions of the i-ZnO layer used in Chapter 3. 60
5.2 Table with an overview of the processing conditions of the i-a-Si:H absorber layer used in experiment 7. . . . 61
5.3 Table with an overview of the processing conditions of the i-nc-Si:H absorber layer used in experiment 7. . . . 61
5.4 Table with an overview of the processing conditions of the i-a-Si:H absorber layer used in experiment 8. . . . 62
5.5 Table with an overview of the processing conditions of the i-nc-Si:H absorber layer used in experiment 8. . . . 62
5.6 Table with an overview of the processing conditions of the i-a-Si:H absorber layer used in experiment 9. . . . 63
5.7 Table with an overview of the processing conditions of the i-nc-Si:H absorber layer used in experiment 9. . . . 63
5.8 Table with an overview of the key electrical parameters obtained measurements of samples from experiment 7, the X is crystallinity in % and η shows the efficiency. . . . 64
5.9 Table with an overview of the key electrical parameters obtained measurements of samples from experiment 8, the X is crystallinity in % and η shows the efficiency. . . . 66

5.10 Table with an overview of the key electrical parameters obtained measurements of samples from experiment 9, the X is crystallinity in % and η shows the efficiency. 68

B.1 Table with an overview of the full processing conditions of experiment 1, including all doped layers. 81
B.2 Table with an overview of the full processing conditions of experiment 2, including all doped layers. 81
B.3 Table with an overview of the full processing conditions of experiment 3, including all doped layers. 82
B.4 Table with an overview of the full processing conditions of experiment 4, including all doped layers. 82
B.5 Table with an overview of the full processing conditions of experiment 5, including all doped layers. 83
B.6 Table with an overview of the full processing conditions of experiment 6, including all doped layers. 83
B.7 Table with an overview of the full processing conditions of experiment 7, including all doped layers. 84
B.8 Table with an overview of the full processing conditions of experiment 8, including all doped layers. 85
B.9 Table with an overview of the full processing conditions of experiment 9, including all doped layers. 86

1 Introduction

Clean and renewable energy sources are urgently needed to reduce the emissions of greenhouse gasses if global warming and its potential risks are to be minimized as stated by the IPCC in their 2023 report [1]. Solar energy generated by photovoltaics (PV) has emerged as one of the most promising renewable energy sources as it is abundantly available and the technology is cost-competitive [2],[3]. Thin-film silicon solar cells can contribute to generating more renewable energy as Silicon (Si) is abundantly available as well as most other materials, such as Oxygen, Zinc, Aluminium, Silver, Carbon and Hydrogen used to fabricate thin-film silicon modules except for Tin (Sn). Another benefit of thin-film silicon solar cells is that Silicon as well as the other materials are non-toxic [4].

1.1. The need for solar energy

A trend of global warming has been observed since the industrialisation in the mid-18th century, the period of 2006-2015 being 0.87 degrees warmer than the period of 1850-1900 [1]. The warming does not take place homogeneously as land regions heat up more than oceans. Certain areas, such as the Arctic, are even warming at several times the average pace. Another trend that is being observed is an increase in the severity and recurrence of weather extremes. Emissions caused by human activity are a major contributor to global warming and the resulting climate change as is illustrated by the ”Estimated anthropogenic warming line” that is compared to ”Observed monthly global mean surface temperature” [1].

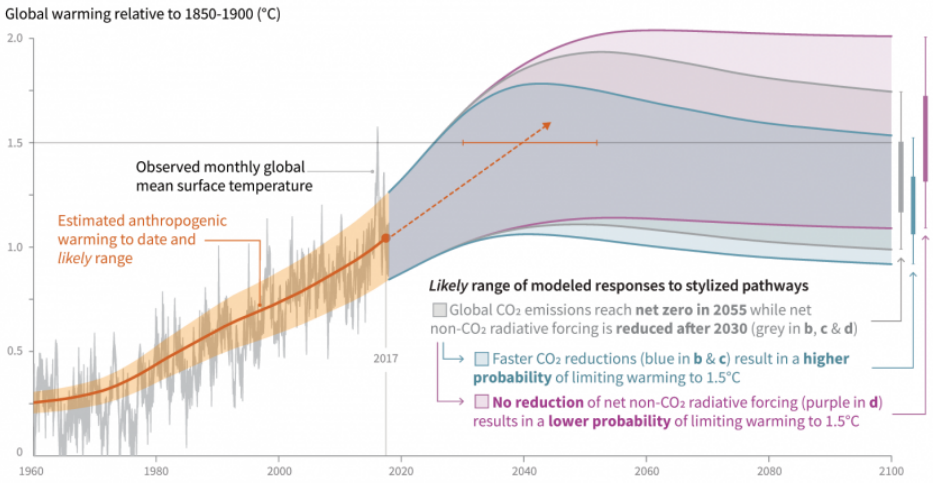

Figure 1.1: A depiction of how global warming is related to anthropogenic (man-made) emissions from the IPCC (International Panel for Climate Change [1].

Serious risks are associated with global warming and climate change such as extreme temperatures, droughts and sea level rise [5]. Industrial processes and energy-related emissions from fossil fuels account for a large part of the total share of CO_2 emitted in earth’s atmosphere as illustrated in Figure 1.2 [6]. Since 1900 there has been an almost continuous increase in the amount of Carbon emissions from energy combustion and industries as noted by the International Energy Agency [6]. To reduce the emission of greenhouse gasses, clean and renewable energy sources are needed on a large scale if serious reductions in the emission of greenhouse gasses are to be achieved and thus the risks are to be minimized.

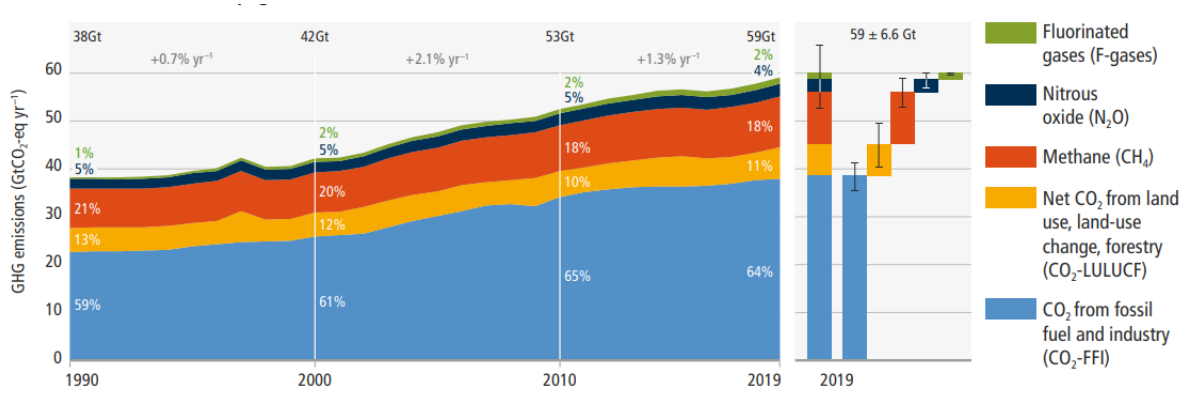

Figure 1.2: A depiction of anthropogenic (man-made) emissions from the IPCC (International Panel for Climate Change) [1].

Solar energy is the most abundant renewable energy source and its yearly potential of 23000 Terawatts-years(TW-YR) is significantly larger than the 16 TW-YR used yearly as shown in 1.3. Several ways of harnessing solar do exist such as Concentrating Solar Power (CSP), Solar Heating and Cooling (SHC) and Photovoltaics on which this thesis will focus [7]. Solar energy can be harnessed by the photovoltaic effect by using the energy in the form of photons to directly generate electrical power in so-called solar modules, which can be placed on rooftops, solar parks and in some cases in agri-PV. This technology is mature nowadays as the theoretical limits of 29.8%, as calculated by the Yablonovitch limit, for single-junction c-Si devices are approached more closely every year with reported efficiencies of 26.8% [8],[9]. Besides the abundance of solar energy and its mature harnessing technologies it has also become the most cost-effective way of generating electricity as stated by the IEA in [10].

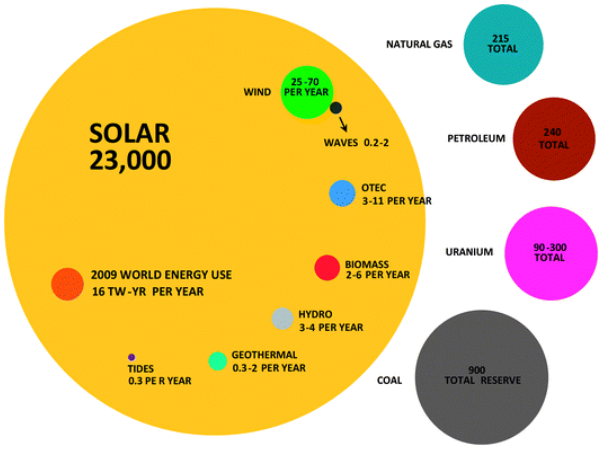

Figure 1.3: A comparison of the total finite (fossil) energy sources and yearly potential of renewable energy sources [11].

1.2. Motivation for thin-film silicon solar cells

The solar PV industry is currently dominated by crystalline silicon modules with a market share of 95% in production in 2021 as reported by Fraunhofer ISE [12]. Thin-film techniques currently thus only have a small market share, however, the potential of thin-film technologies is in their versatile deployment and very large-scale production potential for silicon-based thin-film solar modules.

Typical crystalline silicon solar cells are fabricated from silicon wafers in the range of 160-240 μm ($10^{-6}m$) thick, with up to 50% of the silicon being lost as kerf losses due to the cutting process [13],[14]. An efficiency of 26.6% was demonstrated by Yoshikawa et al for a 180 cm^2 heterojunction interdigitated back contact (HJ-IBC) c-Si cell [9].

One of the advantages of thin-film technologies such as hydrogenated amorphous silicon solar cells (a-Si:H) and hydrogenated nano-crystalline silicon solar cells (nc-Si:H) are that they use significantly

less material when compared to c-Si solar cells. Typical thicknesses of the absorber layer in a-Si:H are in the range of 300 nm ($10^{-9}m$), for nc-Si:H a typical cell is 2.5 μm ($10^{-6}m$). This results in far lower usage of high purity Silicon per generated kWh. The efficiency of the thin film solar cells are however limited due to the nature of the amorphous and nano-crystalline material as will be explained in Section 2.3. A record efficiency of a thin-film silicon solar cell (a-Si:H top cell and nc-Si:H bottom cell) was demonstrated by AIST of 12.69% [15]. If taken into account the energy yield per kilogram of silicon the thin-film techniques show a lot of potential when compared to c-Si, making it a suitable candidate for TW production [16].

Another advantage of thin-film technologies is that they are lightweight and flexibility if the cells are produced on flexible substrates. This makes thin-film solar cells applicable on structures where conventional c-Si modules can not be placed as demonstrated in an artist render by the manufacturer Hyet Solar in Figure 1.4.

Figure 1.4: An artist render of Hyet thin-film silicon modules on a Vopak terminal [17]

A last advantage of the thin-film techniques is the efficient utilisation of available area as shown in another artist's render by Hyet Solar in Figure 1.5. The better utilisation of the available roof area could negate the lower efficiencies that are typically achieved in thin-film silicon solar cells. If the promised efficiencies can be achieved by Hyet Solar in a cost-effective manner their thin-film silicon technology could be able to compete with the c-Si modules that dominate the market currently [18].

Figure 1.5: An artist render of HYET thin-film silicon modules compared to c-Si modules on a rooftop [19]

1.3. The goal of this research

This research aims to make highly efficient thin-film silicon solar cells on a lab scale as a technology demonstrator to showcase the potential of the production line of HYET solar that is being set up. This thesis will focus on the performance part of tandem solar cells made from Silicon that are processed in a p-i-n (superstrate) configuration. The main focus of the research is to improve solar cells deposited on glass substrates, combining the efforts of other researchers at Delft University of Technology. Ongoing experiments are performed on anti-reflection coatings, TCO's, glass texture and the silicon layers that make up the solar cells. The goal of this research is to combine those research efforts to make an a-Si:H/nc-Si:H tandem solar cell with the highest efficiency possible. Research on improving the efficiency and stability of these tandem cells is necessary to prove the competitiveness of these types of solar

cells. Several ways of achieving higher efficiencies and understanding the mechanics of tandem solar cells will be researched:

Q1: Can high open-circuit voltage amorphous silicon solar cells be processed efficiently by using a VHF-PECVD chamber at 40.68MHz?

Q2: What is the optimal texture and TCO combination that can be used to process high-efficiency a-Si:H and nc-Si:H single junction solar cells?

Q3: What is the optimal texture, TCO and ARC combination for a high-efficiency a-Si:H/nc-Si:H solar cell deposited using RF-sputtering and RF/VHF-PECVD processes?

1.4. Structure of the report

This report is made up of four chapters. Chapter 2 will provide an overview of the fundamental working principles of solar cells and the characterization methods used throughout this report. Chapter 3 will provide a concise literature study on PECVD processes, after which the setup of the experiments in Chapter 3 will be shown. This chapter will focus on creating high-bandgap amorphous silicon single-junction solar cells processed in a VHF-PECVD chamber. The results and discussion on the outcome of the experiments be presented, followed by a conclusion. Chapter 4 will show a concise literature study on textured glass substrates and the use of i-ZnO as part of a bilayer TCO and as a back reflector. This chapter will focus on improving short-circuit current densities of nano-crystalline single-junction solar cells and amorphous silicon single-junction solar cells. The setup of the experiments in Chapter 4 will be provided, after which the results and a discussion on the outcome of these experiments will be presented. Chapter 5 will focus on improving the reproducibility and performance of a-Si:H/nc-Si:H tandem solar cells, for which a concise literature study will be shown. The setup of the experiments carried out in Chapter 5 will be provided and the results will be shown together with a discussion. Finally, a conclusion and recommendations are presented.

2

Fundamentals of silicon solar cells

Solar panels enable the direct conversion of sunlight into usable electricity through the photovoltaic effect (PV). Several types of solar cells can be identified, such as crystalline silicon (c-Si) solar cells, thin film silicon (TF-Si) solar cells, III-V solar cells, copper indium gallium selenide (CIGS) solar cells, quantum-dot solar cells, cadmium telluride (CdTe) solar cells and perovskite solar cells. Currently, c-Si solar cells take up over 90% of the global PV market. However, they need thick layers of several hundreds of μm of silicon wafers. Thin film technologies require far less material as the entire solar cell can be made with just several μm of silicon [4]. The use of fewer raw materials and the maturity of thin film deposition techniques have also made TF-Si solar cells more cost-effective than c-Si cells concerning the Levelized Cost of Energy (LCOE) [20]. They also do not require any toxic materials for their production and they can be made into lightweight and flexible modules [4]. This thesis tries to improve the efficiency of a so-called micromorph thin film solar cell, which is a combination of an amorphous silicon (a-Si:H) top cell and a nanocrystalline silicon (n-Si:H) bottom cell.

2.1. Fundamental principles

In this section, some of the underlying principles of the working of a solar cell will be explained. These principles are essential to understanding the scope of this thesis.

2.1.1. Light

To describe the different processes that are happening inside a solar cell, it is important to realise that light can be described both as a wave and as a particle. This duality principle means that for some concepts the wave description is used and for some the particle description. If light is described as a particle, it is seen as a photon, which can be split into an electron-hole pair. The electron and hole can be separated in the solar cell to generate electrical power. The energy of photons, out of which light consists, can be characterised by the following formula:

$$E = hv = \frac{hc}{\lambda} \tag{2.1}$$

In this equation, *E* is the energy of a photon in electronvolt (eV), v is the frequency of the photon,λ is the wavelength in nm, *h* is Planck's constant and *c* is the speed of light in vacuum. Both definitions for light will be used throughout this thesis. It is also important to note that the energy of photons is inversely proportional to their wavelength, meaning that smaller wavelengths carry more energy than larger wavelengths.

2.1.2. Solar spectrum

To describe the radiation from the sun, the concept of a black body is often used, since is around 6000K this spectrum will be used to describe its spectral radiation. Not all the waves emitted from the sun will reach the earth's surface, therefore a distinction is made between several solar spectra. The AM0 spectrum describes the irradiance outside of the earth's atmosphere and is 1361 W/m^2 according to. For terrestrial applications, the AM1.5 Global and the AM1.5 Direct and circumsolar solar spectrum are used to describe how much radiation per wavelength is incident on the earth's surface. The solar irradiance on Earth is generally described by the AM1.5 Global spectrum which takes into account that the atmosphere absorbs part of the irradiance and is 1000 W/m^2 [21].

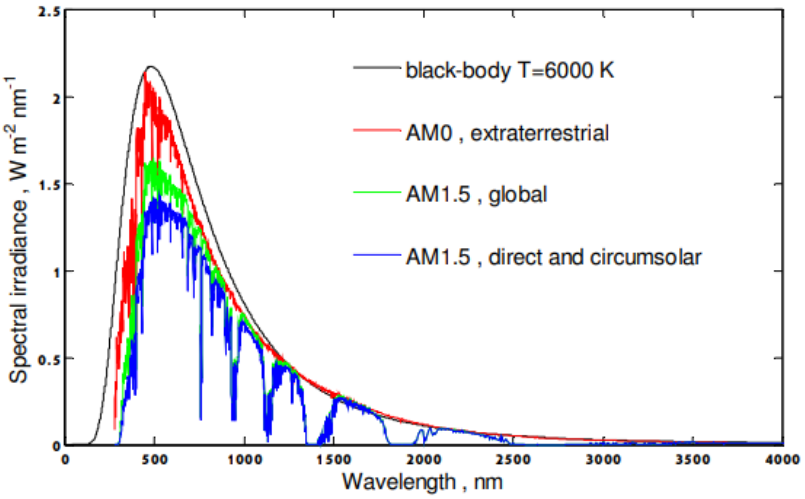

Figure 2.1: The solar spectrum AM0 and AM1.5G and AM1.5D from [22].

Figure 2.1 shows the spectral irradiance of a black-body, AM0, AM1.5G and AM1.5D spectrum. The standard testing conditions (STC) are used to compare the performance of solar cells, these are at 25°C and 1000 W/m^2 of irradiance.

2.1.3. Semiconductor physics

Atomic structure and conduction

Silicon has the atomic number 14, which means it has 14 electrons in three different cells orbiting the nucleus. Out of the 14 electrons, 2 are in the first shell and 8 are in the second shell. This leaves four electrons to occupy the third shell, these electrons are called the valence electrons [21]. Since a Silicon atom has 4 valence electrons it can be covalently bonded to four other Silicon atoms in a crystal lattice. If the crystal lattice consists of only silicon it is called intrinsic crystalline Silicon (i-c-Si) A two-dimensional representation of this structure can be seen in Figure 2.2 (a) for a temperature of $0K$.

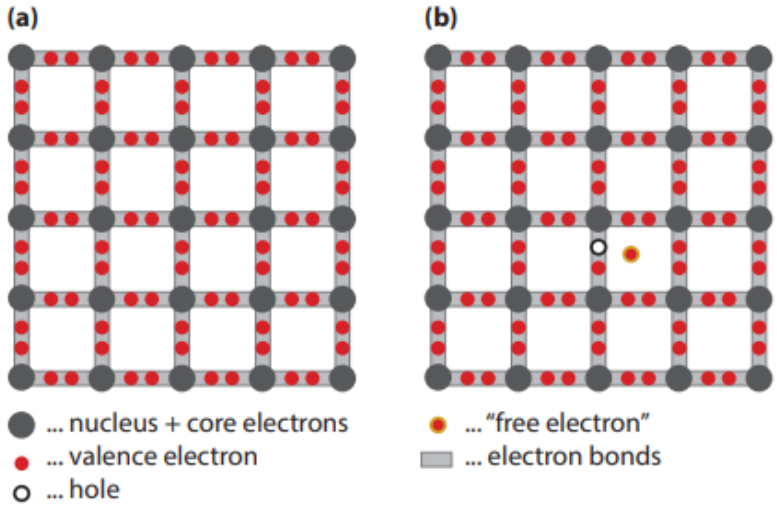

Figure 2.2: The structure of crystalline Silicon from [21].

If the temperature is above 0 K as shown in 2.2 (b), the bonds will absorb thermal energy and electrons will break free from their covalent bonds. When an electron breaks its covalent bond, it leaves behind a hole. The hole that is created can be occupied by other valence band electrons. This process of another valence electron taking up the place of the hole can be seen as the hole moving through the

crystal lattice. The electron that is excited to the conduction band can contribute to the current flow, as it is now in the conduction band and made from the crystal lattice [21].

doping

The concentration of electrons and holes can be influenced by doping the crystalline silicon structure with an element that has three of five valence electrons. Widely used dopants for c-Si are Boron (three valence electrons) and Phosphorus (five valence electrons), the addition of these dopant atoms leads to n-type crystalline silicon (n-c-Si) and p-type crystalline silicon (p-c-Si) as can be seen in Figure 2.3.

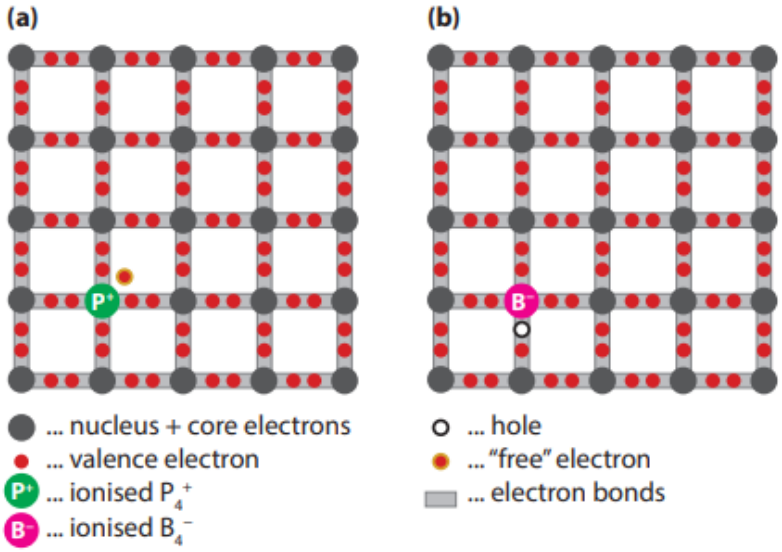

Figure 2.3: The structure of n-type crystalline Silicon (a) and p-type crystalline Silicon (b) from [21].

Density of states

The theory of density of states is very important for understanding the working principles of solar cells as it describes the formation of energy bands. The formation of energy bands can be explained by Figure 2.4. The graph shows a single hydrogen atom in Figure 2.4 (a), where the probability density function for the lowest electron energy state for a hydrogen atom without interaction is shown. In Figure 2.4 (b) the same probability density function is shown, but this time for two hydrogen atoms. The overlap between the two probability density functions means that the energy level is split into two discrete energy levels as can be seen in Figure 2.4 (c) [23].

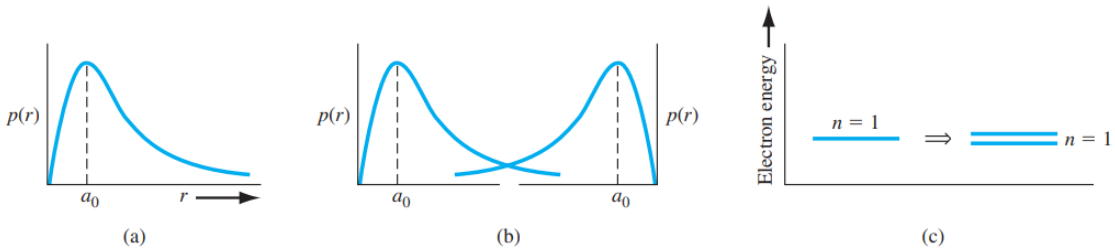

Figure 2.4: Density of states for a single hydrogen atom (a), two hydrogen atoms close to each other (b) and the splitting of the n1 state (c) from [23].

If hydrogen-type atoms are now arranged in a periodic structure and are brought very close to each other, the initial quantized energy level will split into discrete energy levels as seen in 2.5. At r_0, the equilibrium interatomic distance, a band of allowed energy states has formed which is split up in discrete energy levels. The splitting of the energy states follows from the Pauli exclusion principle theorem that states that the number of quantum states stays the same when atoms are arranged together, however

since electrons can not have the same quantum number the electrons will split into bands of energy so that each electron can occupy a quantum state [23].

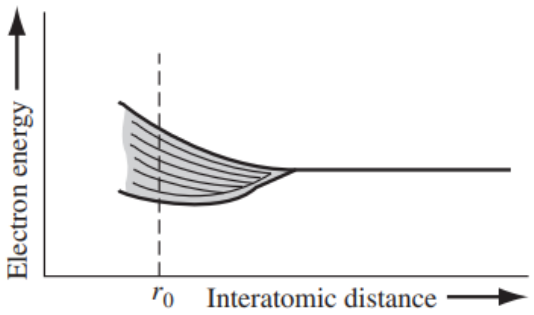

Figure 2.5: Splitting of the quantized energy level into discrete energy states around r_0, the equilibrium interatomic distance [23].

Density of states for Silicon

The density of states theorem can be applied to silicon as well, however, since the electrons are arranged in three discrete energy shells around the nucleus there are also three energy states as shown in Figure 2.7.

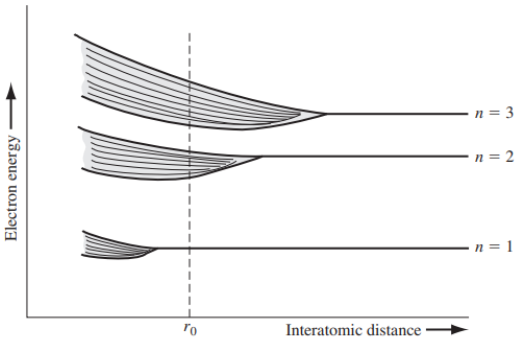

Figure 2.6: Simplified splitting of the three energy levels into discrete energy states around r_0, the equilibrium interatomic distance [23].

For silicon, the first two shells are fully occupied and close to the nucleus, which means they will not interact with other atoms. The outer four electrons in the third shell are weakly bounded, leading them to be involved in chemical reactions. When silicon atoms are brought very close to each other, the quantized energy level in the third shell will split into discrete energy levels as well as can be seen in Figure 2.7 where *Eg* denotes the energy band gap [23].

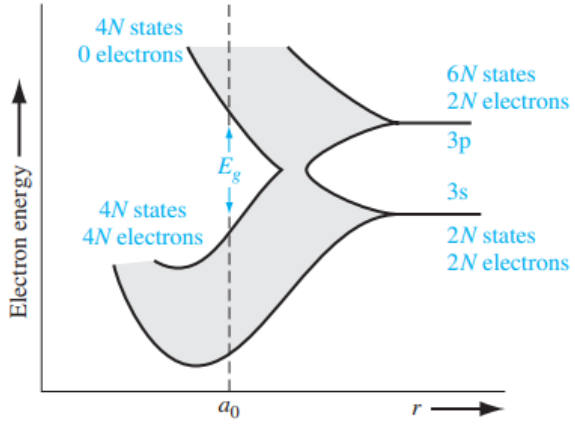

Figure 2.7: Splitting of the quantized energy levels into discrete energy states around a_0, the equilibrium interatomic distance [23].

Bandgaps

As shown in Figure 2.7 an energy band gap is formed, in which the top of this energy band is the conduction band and the bottom is the valence band. The energy difference between the valence band and the conduction band is measured in electronvolts (eV) and is given by 2.2.

$$E_G = E_C - E_V \tag{2.2}$$

This formula describes the amount of energy that is needed to excite an electron from the valence to the conduction band. Equation 2.1 can be used to calculate what the largest wavelength is that can be absorbed if the bandgap is known.

Fermi level

The electrochemical potential of electrons in a material can be described by the Fermi energy, which is the average energy of the electrons in a certain material [21].
In intrinsic semiconductors, the amount of electrons in the conduction band is equal to the amount of electrons in the valence band [23]. Since every electron in the conduction band leaves a hole behind, the concentration of holes and electrons is thus also equal. These concentrations can be denoted by n_i (electron concentration) and p_i (hole concentration). The equilibrium electron concentration can be given by equation 2.3.

$$n_0 = N_c exp\left[\frac{-(E_c - E_F)}{kT}\right] \tag{2.3}$$

In this formula n_0 is the electron concentration, N_c is the effective density of states function in the conduction band, E_c is the energy level of the conduction band and E_F is the energy level of the Fermi level. k is the Boltzmann constant and T is the temperature in Kelvin.
A similar formula can be given for the concentration of holes in the valence band as given by equation 2.4.

$$p_0 = N_v exp\left[\frac{-(E_F - E_v)}{kT}\right] \tag{2.4}$$

In this formula p_0 is the hole concentration and N_v is the effective density states function in the valence band, finally E_v is the energy level of the valence band.
The formulas to describe both the electron concentration in the conduction band and the hole concentration in the valence are given and since $n_i = p_i$ is it possible to determine the intrinsic carrier concentration of the semiconductor. This formula can be derived by combining Equation 2.3 and Equation 2.4 as shown in Equation 2.5

$$n_i{}^2 = N_c N_v exp\left[\frac{-(E_c - E_v)}{kT}\right] = N_c N_v exp\left[\frac{-(E_g)}{kT}\right] \tag{2.5}$$

For intrinsic semiconductors, the Fermi level is situated halfway through the bandgap and shown as E_{Fi} as shown in 2.8. As the semiconductor material is doped, the Fermi level changes towards the valence band (p-type) and towards the conduction band (n-type).

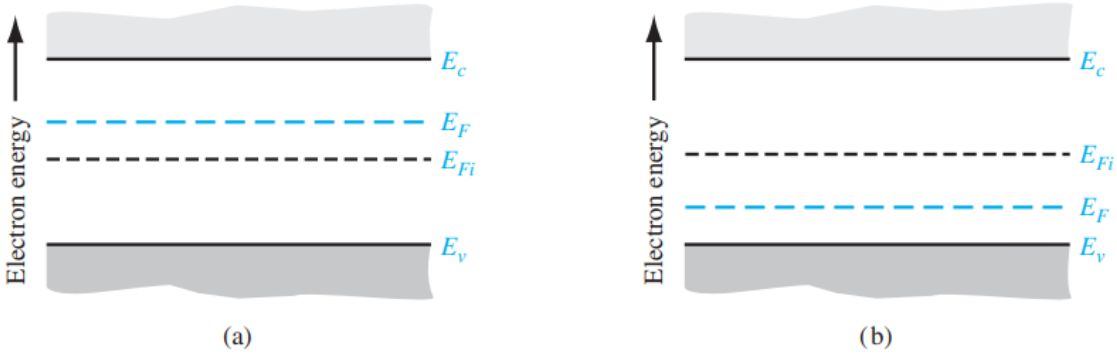

Figure 2.8: Simplified bandgap of a n-type semiconductor (a) and a p-type semiconductor (b)[23].

PN junction

When a p-type and n-type semiconductor are bonded together they form a PN junction along with a metallurgical junction at the place where the materials are joined [23]. In the metallurgical junction, there will be an area that is called the space charge region and is shown in Figure 2.9.

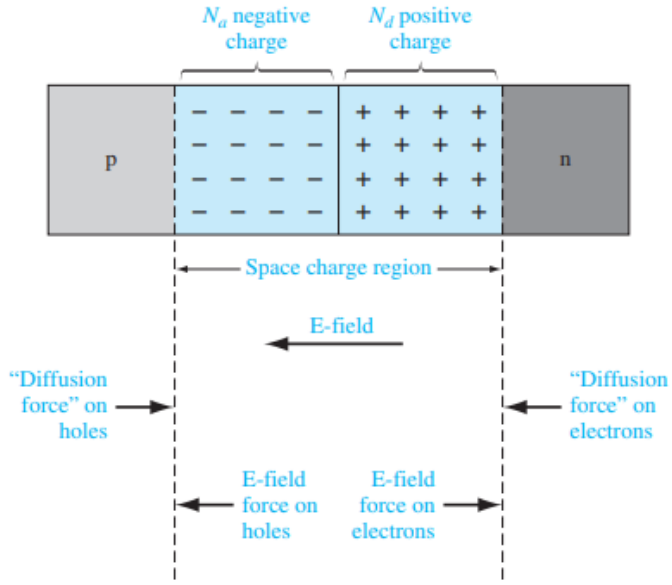

Figure 2.9: Space charge region in a PN junction[23].

As shown in Figure 2.9 the area in the p-type material is negatively charged and the n-type material is positively charged. This happens as the majority charge carriers from the n-type material (electrons) diffuse to the p-type material and thus leave behind positively charged donor atoms. At the p-type material, the opposite reactions happens as the majority charge carriers (holes) will move from the p-type material to the n-type material, thus leaving behind negatively charged donor atoms [23]. This creates an electric field since there is a positively charged region as well as a negatively charged region, where the electrons move opposite the direction of the electric field. The force acting on the electrons due to the electric field is called drift, the drift forces move the electrons towards the n-type region. Diffusion on the other hand forces the electrons towards the p-type region [23].

Band diagram
The bandgaps of p-type and n-type material are different as shown in 2.8, when they are combined in a PN junction the Fermi levels have to align. This creates the band bending as shown in Figure 2.10, where the energy levels of the conduction band, the valence band and the Fermi levels are shown.

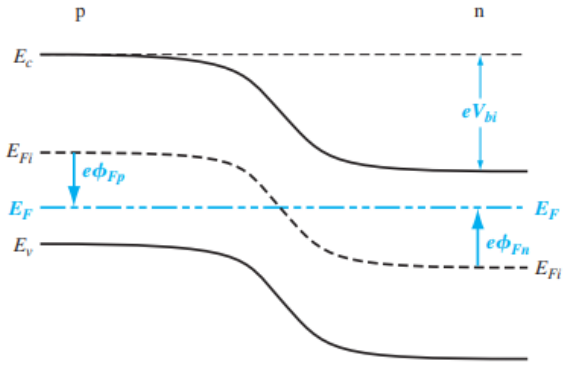

Figure 2.10: Band diagram of a PN junction[23].

2.1.4. Electromagnetic waves and optics

Light is an electromagnetic wave and can be characterized by the Maxwell equations, the equation for electromagnetic waves can be seen in Equation 2.6.

$$\left(\frac{\partial^2}{\partial x^2}+\frac{\partial^2}{\partial y^2}+\frac{\partial^2}{\partial z^2}\right)\mathbf{E}-\frac{n^2}{c_0^2}\left(\frac{\partial^2\mathbf{E}}{\partial t^2}\right)=0 \tag{2.6}$$

In this equation *E* is the electric field, *c0* is the speed of light in vacuo and *n* is the refractive index [21]. When this equation is solved for the *z* direction, which is perpendicular to the surface of the medium and a constant wavelength is taken the electric field can be written as 2.7[21].

$$\mathbf{E}(\mathbf{r},t)=\mathbf{E}_0e^{ik_zz-i\omega t} \tag{2.7}$$

In this formula k_z is the wave number as seen in Equation 2.8 [21].

$$k_z=\frac{n\omega}{c} \tag{2.8}$$

The angular frequency in Equation is 2.8 is defined in Equation 2.9 [21].

$$\omega=2\pi v=\frac{2\pi}{T} \tag{2.9}$$

There is an interaction when electromagnetic waves reach the interface between different types of materials, this interaction is described by Snell's law as can be seen in Equation 2.10.

$$n_1\sin(\theta_i)=n_2\sin(\theta_t) \tag{2.10}$$

Snell's law describes the interaction of the incident light between the incident light and the transmitted and reflected light on the interface of 2 materials with different refractive indexes, as seen in Figure 2.11. In this equation *n1* and *n2* are the refractive indexes of the respective media, furthermore Θ_i, Θ_r and Θ_t are the angles of incident, reflected and transmitted light respectively.

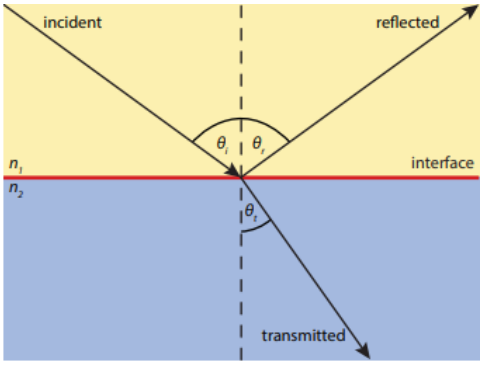

Figure 2.11: Snell's law from [21].

For solar cells, textured surfaces are used to scatter light to help with the absorption of incident photons. Since light is partially absorbed and reflected it can be described by Fresnel equations as seen in Figure 2.11 for *s* polarized light and in Figure 2.12 for *p* polarized light. Here the distinction is made between light that is perpendicular polarised to the electric field (*s* polarized) and light that is parallelly polarized (*p* polarized)[21].

$$\begin{aligned} t_s &= \left(\frac{E_{0t}}{E_{0i}}\right)_s = \frac{2n_1 \cos\theta_i}{n_1 \cos\theta_i + n_2 \cos\theta_t}, \\ r_s &= \left(\frac{E_{0r}}{E_{0i}}\right)_s = \frac{n_1 \cos\theta_i - n_2 \cos\theta_t}{n_1 \cos\theta_i + n_2 \cos\theta_t}, \end{aligned} \tag{2.11}$$

$$\begin{aligned} t_p &= \left(\frac{E_{0t}}{E_{0i}}\right)_p = \frac{2n_1 \cos\theta_i}{n_1 \cos\theta_t + n_2 \cos\theta_i}, \\ r_p &= \left(\frac{E_{0r}}{E_{0i}}\right)_p = \frac{n_1 \cos\theta_t - n_2 \cos\theta_i}{n_1 \cos\theta_t + n_2 \cos\theta_i}. \end{aligned} \tag{2.12}$$

For unpolarized light, like solar irradiation, the formula can be simplified to Equation 2.13. This equation describes the amount of light that is reflected on the interface and is taken as the average between the squared values of r_s and r_p [21].

$$R = \frac{1}{2}\left(r_s^2 + r_p^2\right) \tag{2.13}$$

Since there is a conservation of energy, the sum of the Reflectance (R) and Transmission (T) must equal 1. Therefore, the formula can be rewritten to Equation 2.14 [21].

$$T = 1 - R = \frac{n_2 \cos\theta_t}{n_1 \cos\theta_i}\frac{1}{2}\left(t_s^2 + t_s^2\right) \tag{2.14}$$

For the situation where $\theta_t = \theta_i = 0$ the reflection coefficient can be simplified as there is no distinction between polarisation, therefore the formula becomes:

$$R = \left|\frac{n_1 - n_2}{n_1 + n_2}\right|^2 \tag{2.15}$$

For the formulas in this chapter so far, it has been assumed the media are not absorbing the light, thus only the Reflectance and Transmission have been explained. Solar cells however need to absorb light to excite charge carriers, therefore another important parameter in solar cells is absorption. The absorption can be defined by the complex electric permittivity $\tilde{e}$ as seen in Equation 2.16.

$$\tilde{\epsilon} = \epsilon' + i\epsilon'' \tag{2.16}$$

The refractive index will also change, as it is defined as the square root of $\tilde{e}$ and it is also complex as seen in 2.17 [21].

$$\tilde{n} = \sqrt{\tilde{\epsilon}} = n + i\kappa \tag{2.17}$$

κ is in equation 2.17 the imaginary part of the refractive index and can also be rewritten from Equation 2.8 to Equation 2.18

$$\tilde{\kappa_z} = \frac{\tilde{n}\omega}{c} = \frac{n\omega}{c} + i\frac{\kappa\omega}{c} = \kappa'_z + i\kappa''_z \tag{2.18}$$

To find the absorption Equation 2.18 can be substituted in Equation 2.7 to find Lambert Beer's law, which describes the intensity of electromagnetic field [21].

$$I(z) = I_0 exp(-\alpha z) \tag{2.19}$$

2.2. The fundamental working principle of a solar cell

Solar cells work on the principle of the photovoltaic effect, this effect occurs when a junction of two different materials is exposed to electromagnetic radiation, which in turn generates a potential difference at the junction [21]. The potential can be clarified by the so-called band diagram as depicted in Figure 2.12.

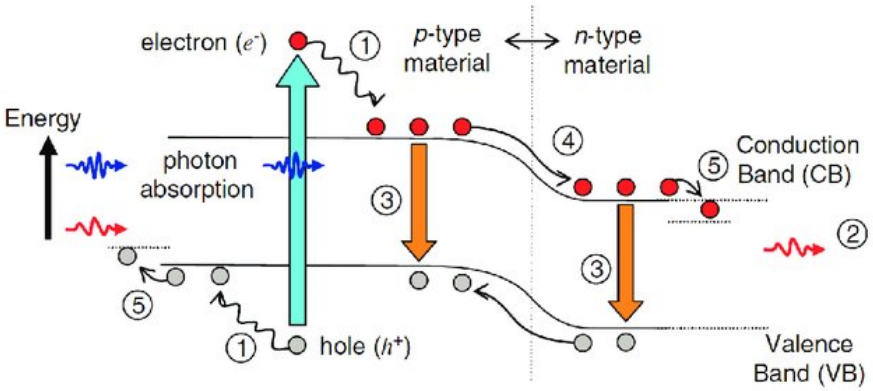

Figure 2.12: A band diagram of a PN junction semiconductor.

2.2.1. Absorption, generation, separation and collection

First, photons need to be absorbed by the solar cell. If a photon is successfully absorbed, it can generate an electron-hole pair in the absorber layer if the energy of the photon is larger than the bandgap (E_g) of the semiconductor. The bandgap is the energy between a semiconductor's valence band and the conduction band. If the energy of the photon is larger than the bandgap, the excited electron will be excited up to the conduction band, however, the excess energy is lost as phonon emission and is lost as heat. This process is called thermalization and this principle is the underlying reason why multi-junction solar cells are so well researched, as they can reduce the energy loss due to thermalization. Photons with energy lower than the band gap will not be converted in an electron-hole pair and can thus not be converted into electrical energy.

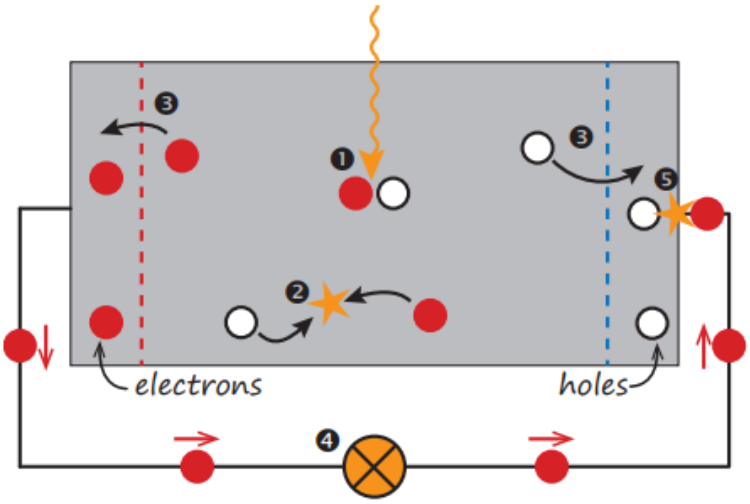

Figure 2.13: Generation, separation and collection of charge carriers from [21].

Second, the generated charge carriers need to be separated to prevent recombination. Recombination processes can take place in radiative and non-radiative forms and need to be limited to a minimum as the electron-hole pair is lost in the process. Charge carrier diffusion lengths play an important role in this process, as the longer the charge carrier has to travel, the larger the chance for recombination becomes. Therefore the solar cell has an optimal thickness between the absorption and generation of charge carriers and the diffusion lengths of charge carriers. Figure 2.13 shows how holes and electrons are generated, separated and collected in a solar cell.

Finally, the charge carriers need to be collected in an external circuit with a pair of electrodes. The electrodes enable the electrons to flow through an external circuit where they can do work before recombining in the solar cell.

2.2.2. Equivalent circuit of a solar cell

After the absorption, generation, separation and collection of the electron-hole pair, the charge carriers have to pass through an electrical circuit as shown in 2.14.

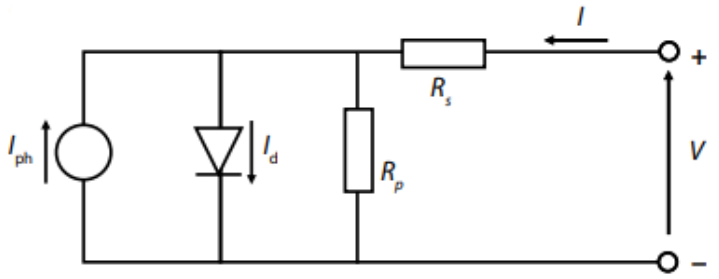

Figure 2.14: The equivalent circuit of a solar cell, including shunt and series resistances from [21].

In the figure, I_{ph} is the photogenerated current, I_d the current over the diode of the solar cell and R_s and R_{sh} are the series and shunt resistance respectively. Note that the R_s wants to be kept as low as possible, whereas R_{sh} should be as high as possible to avoid the electrons from taking shunt paths.

2.3. Thin film solar cells

Thin-film silicon solar cells are produced using a process called plasma-enhanced chemical vapour deposition (PECVD), in this process thin layers of a-Si:H and nc-Si:H are deposited on glass substrates in different configurations. In this research, we mainly use a p-i-n structure which is called the superstrate configuration. The use of this configuration is necessary as diffusion lengths of charge carriers in a conventional pn junction are too small for thin-film silicon solar cells. In a p-i-n structure, the intrinsic layers act as the absorber layer, where the p and n-type layers generate an electric field which helps to collect the charge carriers.

Thin-film silicon solar cells have several advantages compared to conventional wafer-based solar cells [4].

- They are made of abundant and non-toxic materials.
- They can be made under low processing temperatures.
- The processing techniques are very mature.
- The energy yield in kWh per installed kW is higher for Thin-film silicon solar is higher than for c-Si and other thin-film technologies.
- The cells can be made on flexible substrates.

The reason why the amorphous and nano-crystalline silicon solar cells can be very thin is because they have a higher absorption coefficient, especially for higher energy photons as shown in Figure 2.15.

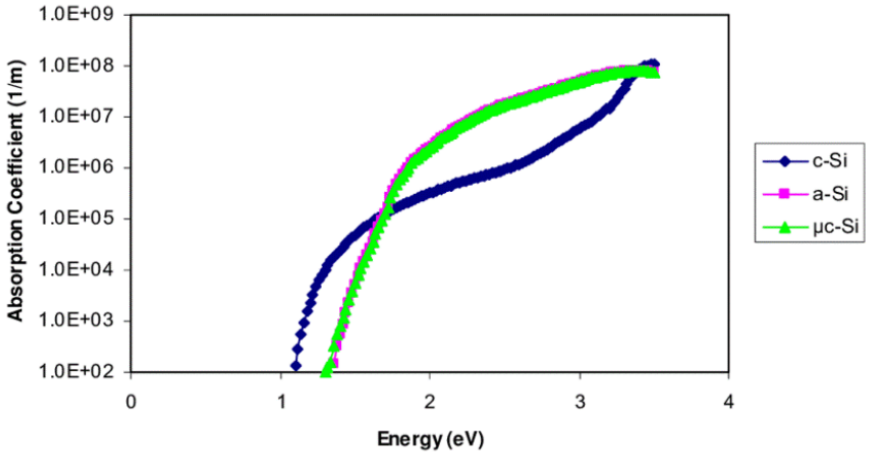

Figure 2.15: The absorption coefficient for a-Si:H, nc-Si:H (here shown as μc-Si) and c-Si [24].

2.3.1. a-Si:H

Hydrogenated amorphous silicon (a-Si:H) will be used as the top cell of the micromorph solar cell. In crystalline silicon, the atoms are structured in a crystal lattice as can be seen in figure 2.18 (a). In amorphous silicon, the atoms are disorganized in the atomic structure and so-called dangling bonds are present, these dangling bonds are recombination centres and therefore hydrogen is used to passivate these bonds as seen in 2.18 (c) [25].

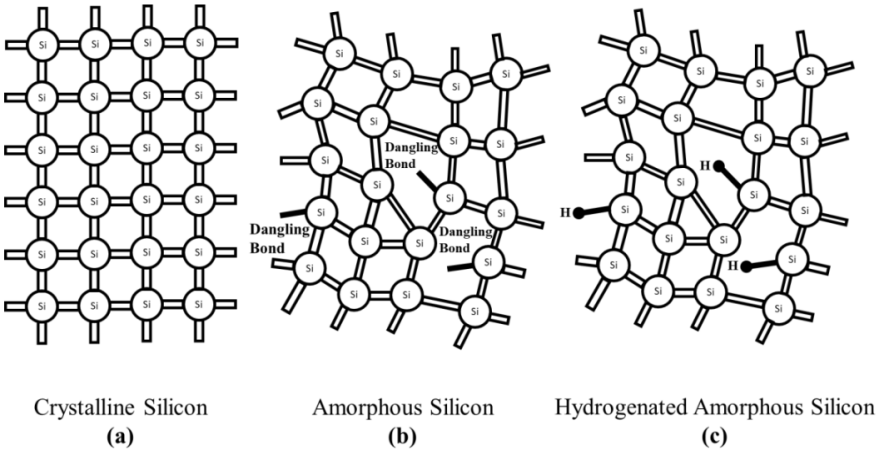

Figure 2.16: The atomic structure of Crystalline silicon, amorphous silicon and hydrogenated amorphous silicon from [25]

The highly disordered atomic structure allows amorphous silicon to have a high absorption coefficient for photons that exceed the bandgap energy, however, the high density of band-tail and defect states shortens the diffusion distance and increases recombination [26]. The bandgap of amorphous silicon also makes it a good material for the top cell, its bandgap of around $1.7eV$ can be tuned by alloying it, thus making it a versatile choice.

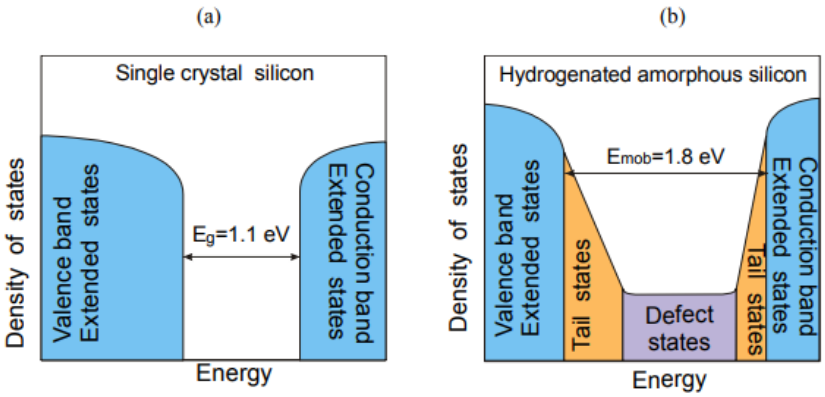

Figure 2.17: The bandgap of Amorphous silicon [27]

2.3.2. nc-Si:H

Hydrogenated nano-crystalline silicon (nc-Si:H) will be used as the bottom cell of the micromorph solar cell. Nc-Si:H is a mix of small crystallines that are surrounded by a-Si:H. The ideal ratio for high-efficiency thin film solar cells is 60% nano-crystals and 40% amorphous silicon according to [28]. In the nc-Si:H there are also dangling bonds that cause recombination, hydrogen is used here as well to passivate these bonds.

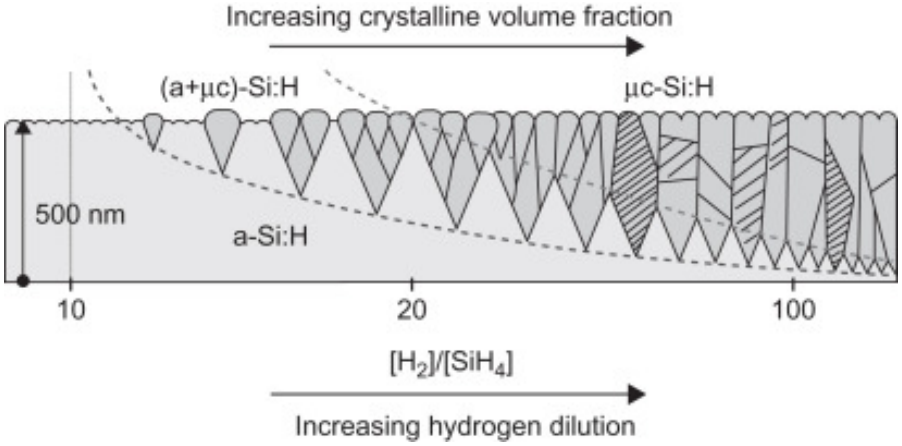

Figure 2.18: Growth of nc-Si:H from [29].

The nc-Si:H is used for the bottom cell as the bandgap of the material is lower, thus allowing it to absorb a wider range of the solar spectrum, its bandgap is around 1.1eV.

2.4. Tandem solar cells

Multiple absorber layers can be used in solar cells to increase their efficiency, so-called multi-junctions. In this thesis, the focus will be on a tandem cell, which consists of a-Si:H top cell and nc-Si:H bottom cell. The use of multi-junctions is that each cell can focus on a different part of the solar spectrum. The top cell will absorb the more energetic shorter wavelengths and will thus be able to reach higher voltages at the cost of lower currents. The bottom cell can absorb the less energetic longer wavelengths and it can utilise a larger part of the solar spectrum at the cost of lower voltages. This can be seen in Figure 2.19, where the spectral utilisation of the a-Si:H top cell is shown between 350nm and 700nm and the nc-Si:H bottom cell between 700nm till 1150nm. The dashed line in Figure 2.19 shows the lower spectral utilisation of a single junction nc-Si:H cell.

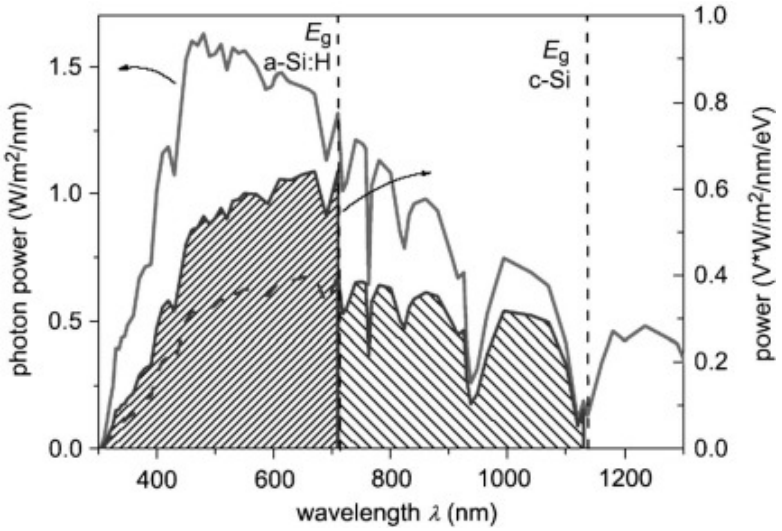

Figure 2.19: Spectral utilisation of a micromorph solar cell, note that the a-Si:H has higher spectral utilisation when compared to the nc-Si:H (dashed line) [30].

The cells will be 2 terminal devices, meaning the current will go through the entire cell. Therefore the cells need to be current matched, as the lowest current would otherwise be limiting the total current and thus the efficiency of the cell. On the contrary, the voltages can be added up in 2 terminal devices.

2.5. Losses and recombination

2.5.1. Losses in solar cells and recombination processes

Several loss mechanisms are present in solar cells, they can either prevent electron-hole pairs from being generated. Examples of these mechanisms are non-absorption, parasitic absorption and optical losses. After the generation of an electron-hole pair thermalization can take place and finally the electron-hole pair can recombine in several recombination processes.

Non-absorption
Non-absorption happens when the energy of incident photons is too low to be absorbed by the solar cell, this is the case for long wavelengths that do not have enough energy to overcome the energy bandgap of the semiconductor material.

Parasitic absorption
Parasitic absorption happens when incident photons are absorbed by layers that are not able to generate electron-hole pairs, thus the energy of the photons is lost.

Optical losses
Optical losses occur at the interfaces of the solar cells where part of the incident photons are reflected due to the difference in refractive indexes of the layers. The photons absorbed by the solar cell should be converted into electron-hole pairs, however, light trapping never fully happens. Ideally, the absorber layer of a solar cell is thick to absorb as much light as possible. On the other hand, the absorber layer can not be made too thick, otherwise, an increase in the recombination processes can be observed, leading to a decrease in collected charge carriers. Different wavelengths require different thicknesses as described in 2.19, resulting in a mismatch of absorber thickness for a range of wavelengths. To improve the path the light travels through the solar cell, texturing can be used.

Thermalization of excess energy
When photons with higher energy than the energy bandgap of the semiconductor material are absorbed, the excess energy is lost in a process called thermalization. To reduce the energy lost to thermalization, multijunction solar cells are used.

Radiative recombination
Radiative recombination mostly happens in direct bandgap materials, in this case, the generated electron-hole pair recombines and is emitted as a photon. This process is essentially the opposite of the generation of an electron-hole pair as described in 2.13.

Shockley-Read-Hall recombination
Shockley-Read-Hall recombination takes place through impurities or defects in the lattice of a semiconductor material. The impurities/defects introduce trap states in the bandgap of the semiconductor at which electrons can be trapped, a hole can then more easily recombine with the electron leading to the loss of the electron-hole pair.

Auger recombination
Auger recombination mostly happens in indirect bandgap materials, as not only a transfer of energy, but also a change of momentum must take place. Auger recombination requires three particles to happen, either two electrons and a hole or two holes and an electron. Excess energy will get transferred to the third particle, which in this case is an electron, which will get excited. The excited electron will lose energy as it relaxes in the vibration of the lattice where it is dissipated as heat.

2.6. Thin film processing techniques

2.6.1. Glass texturing

Several glass textures, such as Asahi VU, ITO and MST substrates, have been used throughout this thesis. The samples processed during this thesis were made on glass and not on flexible foil due to the complexity of the production process on a lab scale for flexible substrates. Asahi VU substrates already have a Transparent Conductive Oxide (TCO) on them, which is Fluorine Tin Oxide (FTO). The

textures influence the scattering of light as well as the electrical performance of the solar cells as the thickness of the TCO and Semiconducting layers change. As can be seen in Figure 2.20 the Asahi UV texture is made of small spikes, the ITO texture is made of large craters and the MST texture is made of a combination of large craters and smaller features. The ITO texture and MST texture are made at TU Delft by depositing a sacrificial ITO or i-ZnO layer that is then etched. Since the material structure of the ITO/iZnO is inhomogeneous, the etching rates of the material are inhomogeneous as well which causes the craters to be formed.

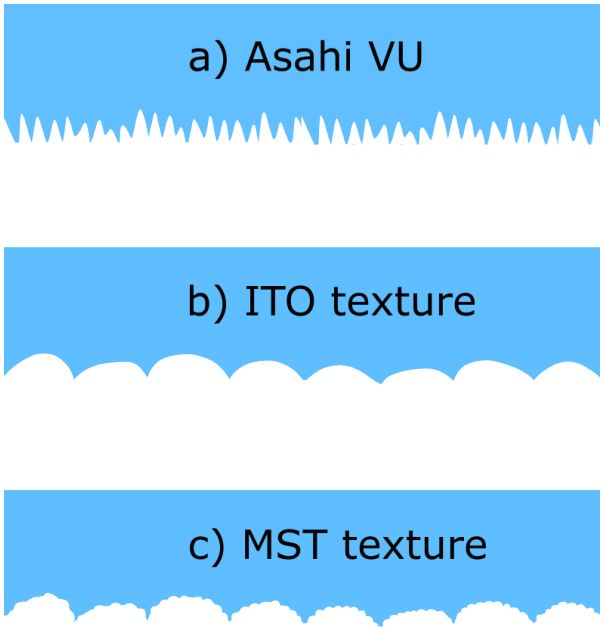

Figure 2.20: Schematic representation of Asahi VU, ITO and MST glass texture used throughout this thesis

2.6.2. Plasma Enhanced Chemical Vapour Deposition (PECVD)

The silicon layers of the solar cells are produced using a process called Plasma Enhanced Chemical Vapour Deposition in a cluster tool called AMIGO from Elettrorava. The cluster tool has six chambers of which four are used for the deposition of silicon layers. In chamber one the p-layers are deposited, in chamber two the n-layers, in chamber three the intrinsic a-Si layers and finally in chamber 4 the intrinsic nc-Si layers. Different chambers separate the deposition processes to reduce cross-contamination between the different layers. In a PECVD deposition chamber, the precursor gasses SiH_4 (Silane) and H_2 (Hydrogen) are mixed in a ratio R which is formulated in formula 2.20:

$$R = \frac{H_2}{SiH_4} \tag{2.20}$$

The precursor gasses are then discharged, this process is initiated by electron-collisional dissociation of the silane gas. The silane is dissociated in reactive neutral species, mostly radicals, which are SiH_3, SiH_2,SiH,Si and H [31]. Radicals can diffuse to the surface of the substrate, however, as the bonds to this surface are weak the radicals can easily be pulled off by interaction with other weakly bounded radicals. If the radicals are bonded to dangling bonds, strong Si-Si bonds can be formed and deposition takes place. Based on the power, pressure and ratio R the deposition conditions can be differed to deposit either a-Si:H, nc-Si:H or a mixture of both [32]. A schematic representation of a PECVD chamber can be seen in Figure 2.21

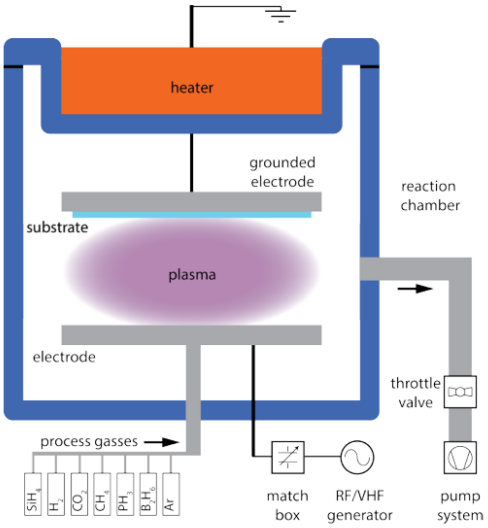

Figure 2.21: Schematic representation of a PECVD chamber and its components [33].

2.6.3. Magnetron Sputtering

The Transparent Conductive Oxide layers (TCO's) are produced using a process called Sputtering, which is a Physical Vapor Deposition (PVD) technique, in chamber 6 of the Amigo cluster tool and the Zorro cluster tool. In this process, an alternating electric field is applied by a Radio Frequency (RF) generator between the target and substrate. An inert gas, Argon, is injected into the chamber and it is partially ionised by the electric field. The positive Argon ions are pulled towards the target, where they collide and species (atoms, molecules and nanoparticles) are thus sputtered towards the substrate where they are deposited. A schematic representation of a Sputtering chamber can be seen in Figure 2.22.

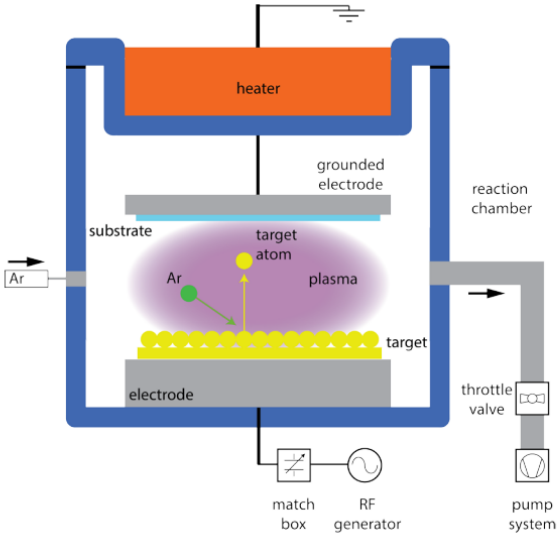

Figure 2.22: Schematic representation of a Magnetron Sputtering chamber and its components [33].

2.6.4. Electron Beam Evaporation & Thermal Evaporation

The contacts of the solar cell are produced using a process called electron beam evaporation and thermal evaporation in the Provac cluster tool. The electron beam evaporation technique uses high-energy electrons to heat a filament, which causes thermionic emission of electrons. These electrons

can be accelerated to provide the required energy to evaporate the source material, which is done through a $10kV$ voltage drop with a $1A$ current. This electron beam is pulled around to the source to prevent the source from melting, a schematic representation of the described evaporation process can be seen in Figure 2.23a. The thermal evaporation technique uses a large DC current to directly heat a resistive crucible that heats the target material. The presence of a high vacuum helps to evaporate the metal and carry the evaporated metal to the substrate [34]. A schematic representation of this process is shown in Figure 2.23b.

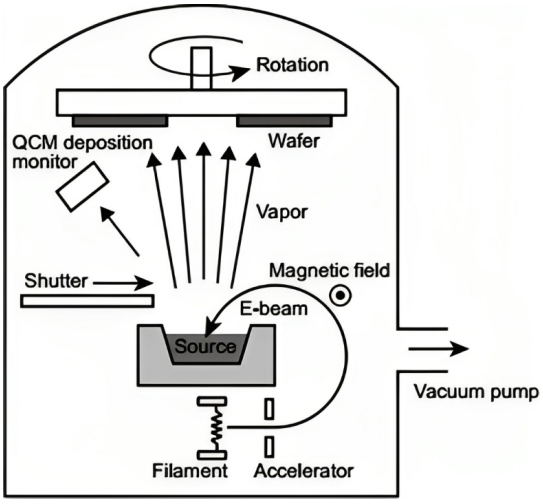

(a) Schematic representation of Electron Beam Evaporation [34].

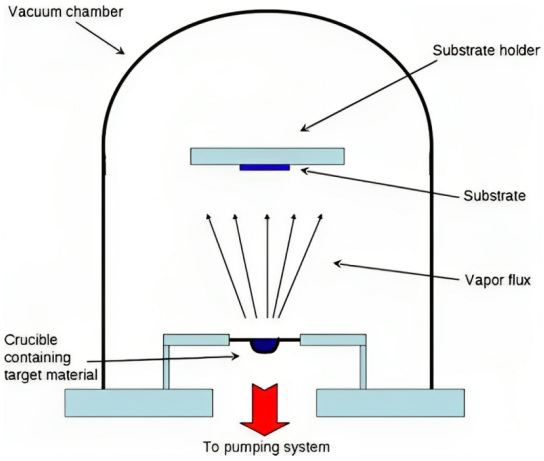

(b) Schematic representation of Thermal Evaporation [34].

Figure 2.23: Schematic representation of the PVD techniques in the Provac tool.

2.7. Characterisation methods

To analyse the performance of the solar cells produced in the lab, several characterisation techniques are used that will be explained.

2.7.1. JV characterisation

A measurement tool called WACOM, a class AAA solar simulator, is used to obtain the performance of the produced solar cells with JV curves. The tool consists of a Halogen and Xenon lamp which are used to simulate the AM1.5 solar spectrum with the help of specific filters. For the specific setup used, two calibration photo-diodes are used to calibrate the setup before doing the measurements. The actual measurements are then performed on a separate stage with 30 pins for the solar cells and 2 pins for the front contacts. The stages are cooled with a Julabo water cooler to keep the samples at $25C^{\circ}$ per the Standard Testing Conditions(STC). For single junction solar cells, in this case, a-Si:H and nc-Si:H, a voltage range of -0.1V to 1V is used. For multi-junction solar cells, a voltage range of -0.1V to 1.5V is used. With the size of the solar cells, either 0.000016m^2 or 0.000025m^2 the current density can then be determined. The characterisation tool plots the current density over the predetermined voltage range to give a JV curve. With the data points provided by the JV measurement, the setup can determine the J_{sc}, V_{oc}, Fill factor (FF), η (Efficiency), R_s (Series resistance) and R_s (Shunt resistance). An example of an IV curve can be found in Figure 2.24, here the I (current) can be easily rewritten to J (current density) by dividing the current over the area of the cell.

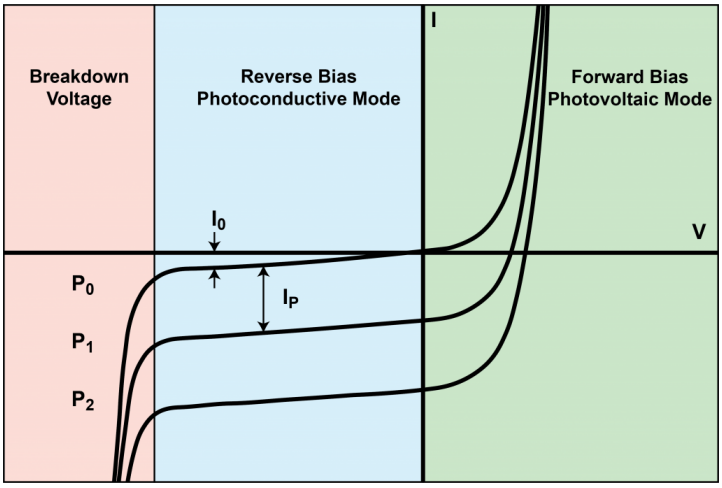

Figure 2.24: An example of an IV curve under breakdown voltage, reverse bias and forward bias [35].

Figure 2.24 show the characteristics of a photodiode in different conditions. P_0 shows the photodiode in the dark under different voltages where I_0 is the dark current. P_1 and P_2 show the IV curve under illumination where I_p is the photogenerated current. In many cases, the JV curve is shown as a positive curve instead of a negative curve as shown in Figure 2.25. From the JV curve, several useful characteristics of the solar cell be determined, such as the V_{oc}, V_{mpp} (maximum powerpoint voltage), J_{sc}, J_{mpp} (maximum powerpoint current density) and FF.

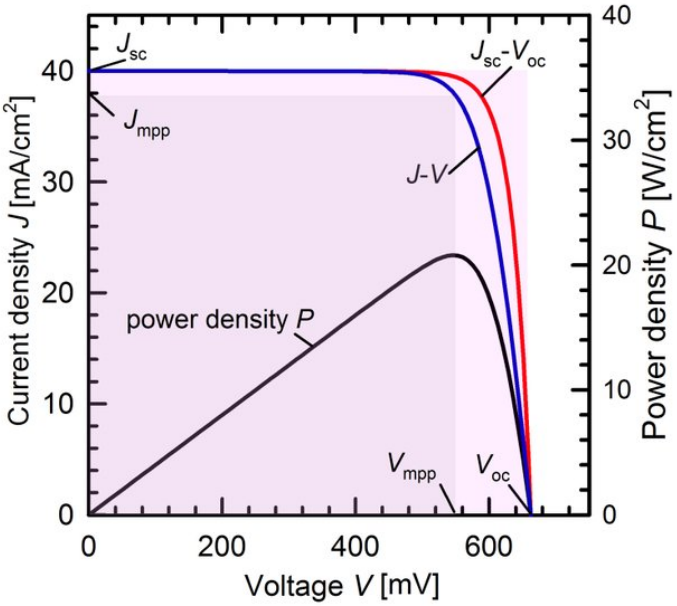

Figure 2.25: A typical JV curve with power density P on a second y-axis for c-Si solar cells for illustration purposes [36].

2.7.2. External Quantum Efficiency (EQE) measurement

The external quantum efficiency (EQE) is the amount of free electrons that are generated by incident photons and collected by an external circuit, divided by the total amount of photons incident on the solar cell [21]. This same equation can be given in formula form as in 2.21.

$$EQE(\lambda_0) = \frac{I_{\text{ph}}(\lambda_0)}{e\Phi_{\text{ph}}(\lambda_0)} \tag{2.21}$$

In this formula, I_{ph} is the number of collected electrons in the external circuit, e is the elementary charge and Φ_{ph} is the photon flux incident on the solar cell. As can be seen from equation 2.21 the EQE of a

solar cell is dependent on the wavelength and therefore is measured with monochromatic light, which is light of a single wavelength (λ). The photo-current per wavelength can then be determined and if a single junction solar cell is measured under short circuit current conditions the J_{sc} of the solar cell can be calculated by taking the integral of the EQE and the photon flux per wavelength as shown in 2.22.

$$J_{sc} = -e \int_{\lambda_1}^{\lambda_2} EQE(\lambda)\Phi_{AM1.5}(\lambda)d\lambda \tag{2.22}$$

The setup used for this thesis is the small EQE setup at the ESP lab on the TU Delft campus, a schematic example of an EQE setup can be seen in figure 2.26. A Xenon arc lamp is used as a light source, which is then filtered by a computer-controlled monochromator. Lock-in amplifiers are used in combination with current/voltage amplifiers to filter the signal by comparing it with a reference signal. The light is also put through a chopper wheel with a frequency of $123Hz$ as this is a frequency with relatively low amounts of background noise.

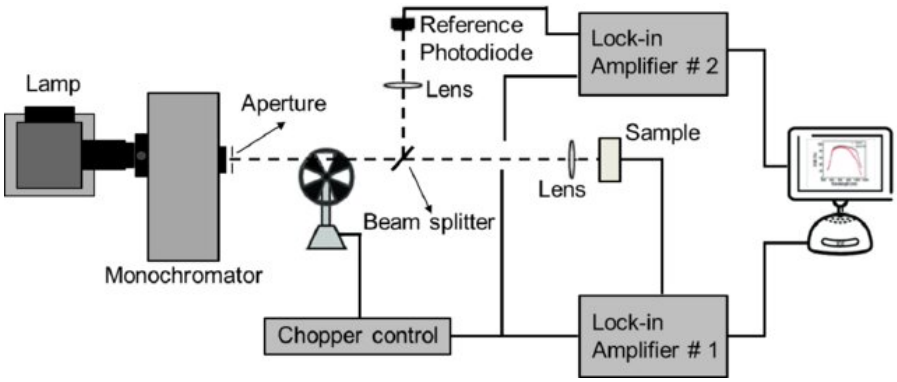

Figure 2.26: Schematic example of an EQE setup [37].

In the setup, a small reference photodiode is used to calibrate the machine before using it to minimise deviations that could be caused by slight changes in lamp wear or temperature for example. The computer will measure the EQE in predetermined steps of $15nm$ over a wavelength range from $300nm$ to $810nm$ for a-Si:H and from $300nm$ to 1140 nm for nc-Si:H and Micromorph tandem cells.
A ring with eight bias lights is also present in the setup for the measurement of tandem solar cells, these lamps emit light at different wavelengths to bias one of the two cells in a tandem device. Since the cells are connected in series the cell with the lowest current will be measured (current limiting cell). This principle is used when the top cell is to be measured, in that case, the bottom cell will be illuminated with a lot of bias light so that it will have a larger current than the top cell. The current limiting top cell will thus be measured albeit in reverse bias when the voltage over the entire device is kept at $0V$ as shown in 2.27 [38]. If the cell is measured in reverse bias the J_{sc} of the cell will be overestimated as the Dark current will increase the total current density. To compensate for this the entire device can be measured in forward bias to measure the actual current density of the cell.

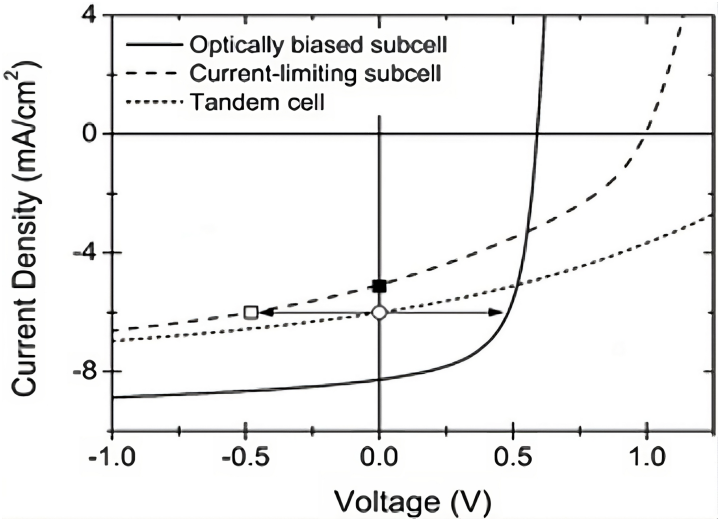

Figure 2.27: Bias voltages in a tandem solar cell, where the white circle indicates the voltage over the entire cell and the white square indicates the reverse bias on the current limiting cell [38].

2.7.3. Reflectance measurement

The reflectance is measured using a Perkin Elmer Lambda 1050+ spectrometer, which uses a set consisting of a tungsten-halogen and deuterium lamp to create a spectrum from 175 nm up to 3300nm. The machine makes use of a variety of optical components, such as lenses, filters, mirrors and gratings to precisely produce a monochromatic beam. The monochromatic beam will enter the integrating sphere, which is a chamber coated in Spectralon, a highly reflective and scattering material. In the integrating sphere, the light will be reflected and scattered in all directions to create a homogeneous magnetic field, which allows the tool to accurately determine the light intensity at different wavelengths. A solar cell can be represented as a block of light-absorbing material where a fraction of the light will be reflected due to the mismatch in the reflective index of air and the solar cell. Another part of the light will be absorbed by the solar cell and converted into charge carriers, if no back contact is present some of the light can be transmitted by the solar cell. Since the sum of the Reflectance, Transmittance and Absorptance should equal 1, this can be written in as formula 2.23.

$$R + T + A = 1 \tag{2.23}$$

Formula 2.23 can be simplified if a back contact is added and therefore it can be assumed that no light is transmitted as shown in Formula 2.24 [39].

$$R + A = 1 \tag{2.24}$$

The machine can be used both for transmittance (T) and Reflectance (R). For the use in solar cells with metallic back contacts only the Reflectance is useful as it can be used to quantify the amount of light that is absorbed (A) in the solar cell.

2.7.4. Raman spectroscopy

Raman measurements are done using a Renishaw inVia Raman spectroscope. This measurement tool sends out monochromatic radiation (photons) with energy hv_0, where v_0 is the initial frequency and h is Planck's constant. When photons with energy hv_0 interact with a sample most of them will be scattered back with the same frequency, this is called Rayleigh radiation. However, some of the photons with energy hv_0 will transfer energy to the molecule on which scattering occurs. After virtual absorption, the scattered photon will bounce back with energy $h(v_0 - v_m)$. The molecule on which scattering occurs will transition to an excited state and will now have additional energy v_m. When this molecule is then hit with another photon it can scatter this new photon back with energy $h(v_0 + v_m)$ as it takes the added energy from the excited molecule as this transitions back. The Raman spectroscope can measure these differences in molecular energy as the photons hit the molecule, get excited and transfer back, so-called Raman radiation. As these differences are specific to certain molecules, the composition of

the molecules can thus be determined [40]. The Raman radiation here is the principle on which the structure of the solar cell can be determined. Every peak in the output of the Raman spectroscope corresponds to a specific molecular bond vibration.
add some text on calculating the crystallinity of the samples

$$X = \frac{A_{510} + A_{518}}{(0.8 * A_{480}) + A_{510} + A_{518}} \tag{2.25}$$

2.7.5. Spectral Ellipsometry

To determine several important material parameters such as refractive index n, extinction coefficient k and thickness of deposited thin films. As explained in 2.1.4 light is an electromagnetic wave and is constructed of both an electric field as well as a magnetic field. For spectral ellipsometry only the electric field is considered as shown in 2.28.

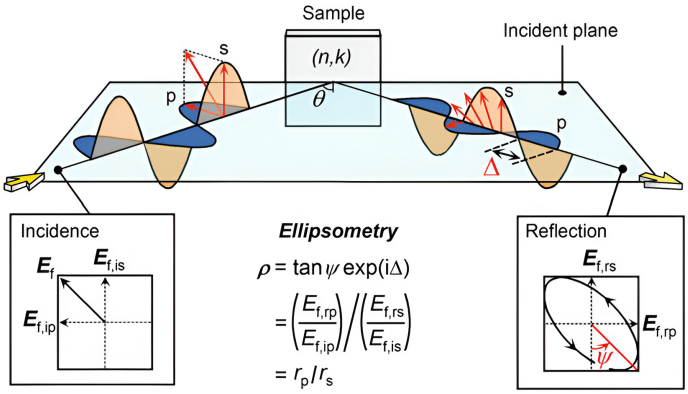

Figure 2.28: An illustration of the basic principle of Spectral Ellipsometry

Polarized light is used, which means there is an s-polarized (perpendicular) and a p-polarized (parallel) component on the plane of incidence, in this case, the sample. When light hits the plane of incidence there is a shift of both the amplitude ratio and phase difference between the s and p-polarizations [41]. From these values, the n and k data can be obtained, which can be useful for making estimates of bandgaps in combination with Tauc plots E_g and the n and k can be used to design anti-reflection coatings as preferably a gradual increasing value of n will reduce reflections as can be derived from Snell's law as seen in 2.10.

2.7.6. Scanning Electron Microscope (SEM)

A Hitachi Regulus 8230 is used to obtain cross-sections of the solar cells, this tool shoots a narrow beam of high-energy electrons at the surface of a specimen through a high accelerating voltage. The high-energy electrons interact with the surface of the specimen, causing interactions between the electrons and the specimen. These interactions can be measured as signals in the form of secondary electrons and backscattered electrons, which can be measured by detectors in the setup as shown in Figure 2.29. The signals from the detectors can be transformed into images which can be used to analyse properties of the deposited solar cells [42].

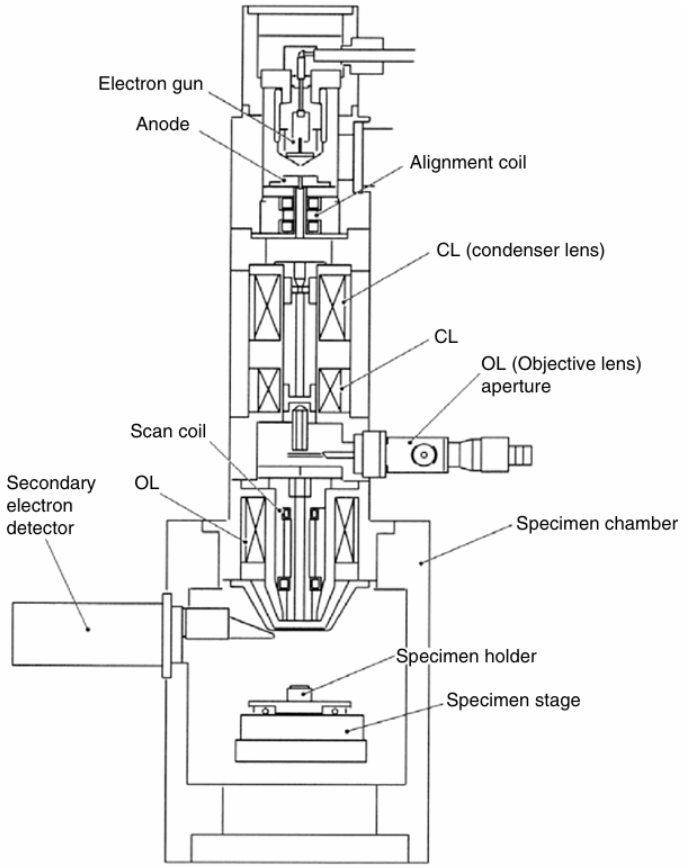

Figure 2.29: A schematic cross-section of a Scanning Electron Microscope [42].

2.8. Solar cell design

Schematic cross-sections of the solar cells will be used to illustrate which layers are used in specific experiments to make clear which layer in the solar cell is varied. As shown in Figure 2.30 a schematic cross-section of a tandem a-Si/nc-Si:H solar cell is depicted on an ITO textured sample, note that the thickness of the layers is not to scale.

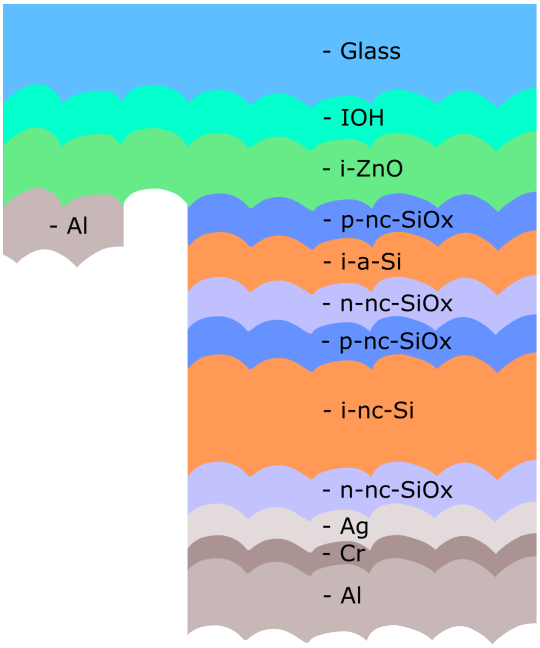

Figure 2.30: ITO textured thin-film silicon solar cell

Another important note is that both p-nc-SiOx and n-nc-SiOx are constructed out of several levels of increasing or decreasing doping levels as shown in 2.31. To keep an overview not all the layers will therefore be shown unless required for explanation.

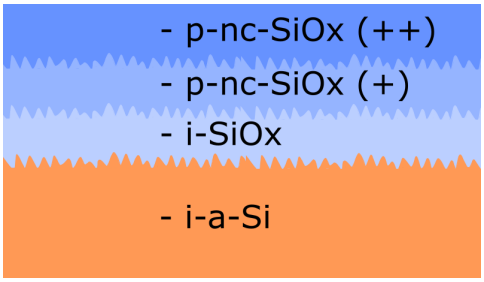

Figure 2.31: Different levels op dopant concentration for the p-nc-SiOx layers on a Asahi substrate

A back contact consisting of three layers is put on the devices to complete the total structure, for all cell 500nm Silver (Ag), 30nm Chromium (Cr) and 800nm of Aluminium (Al) was used.

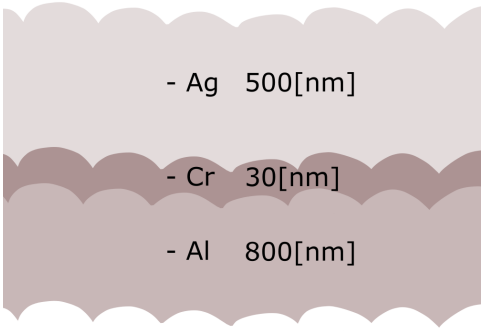

Figure 2.32: A schematic cross-section of the solar cell back contacts

3

High-bandgap hydrogenated amorphous silicon solar cell depositions by VHF-PECVD

In this Chapter high-bandgap amorphous silicon solar cells will be discussed, which can be used as the top cell in a tandem device which uses an a-Si:H top cell and a nc-Si:H bottom cell. High bandgap a-Si:H top cells can improve the efficiency of such tandem devices as they can generate higher open-circuit voltages with minimum loss in obtained current densities. Processing high-bandgap amorphous silicon by changing the excitation frequency used in the PECVD chamber is a novel way of achieving higher bandgap and thus open-circuit voltage which hasn't been widely reported in literature. Researching this novel approach could lead to better-performing high-bandgap amorphous silicon top cells. To explore the possibilities of this novel way of making amorphous silicon solar cells with a high-energy bandgap under high pressure, experiments are performed to evaluate the performance potential of this method. This chapter aims to answer the question of what conditions are best to process high bandgap amorphous silicon solar cells. First, a literature review will discuss previous research done on achieving high open-circuit voltages by making amorphous silicon solar cells with a high-energy bandgap. Second, several experiments are shown that highlight known ways of protecting the sensitive p-layer in thin film silicon solar cells and novel ways of making high bandgap amorphous silicon. Third, a conclusion is presented based on the results and the research question is answered.

3.1. Literature review

In this section a concise overview of high-bandgap amorphous silicon will be given, alongside the record a-Si:H/nc-Si:H cell and module will be discussed. An overview of important parameters for deposition using PECVD reactors will be shown as well as a brief explanation of the use of an i-SiO_x buffer layer.

3.1.1. High bandgap amorphous silicon solar cells

High bandgap amorphous silicon solar cells can improve the efficiency of thin-film silicon multi-junction solar cells by increasing the overall voltage a cell produces. Several ways of achieving amorphous silicon solar cells with high V_{oc} have been explored such as depositions at lower pressures of around 1 $mbar$ and low dilution ratios have been reported to achieve V_{oc}'s over 1 $Volt$. Another approach is to process with high pressures of 7-10$mbar$ which have also been reported to achieve V_{oc}'s over 1 $Volt$ [43]. Regular a-Si:H solar cells processed on the PECVD cluster tool yield V_{oc}'s of around 0.85V which can be considered a baseline value.

3.1.2. Record a-Si:H/nc-Si:H solar cells

The world record p-i-n module-sized a-Si:H/nc-Si:H solar cell developed by TEL solar, with a stabilised efficiency of 12.34% reportedly used a 40.68MHz frequency to deposit both the a-Si:H top cell and the nc-Si:H bottom cell. The intrinsic amorphous silicon absorber layer of this record efficiency exists out of two layers named L1 and L2 as shown in Figure 3.1. A high pressure (2$mbar$) and high hydrogen dilution regime was used to reduce the defect density and increase both V_{oc} and FF for initial and stabilised efficiency. The L1 layer was deposited with a power density of around 20.8mW/cm^2. The L2 layer was deposited at 0.7$mbar$ and is supposed to help generate high current densities. The L1 layer was deposited with a power density of around 20.8mW/cm^2, the bottom cell was processed with a lower power density of 10.8mW/cm^2. A relatively high V_{oc} of 0.918 $Volt$ was reported for the a-Si:H top cell when deposited as a single-junction device with a total initial obtained J_{sc} of 16.15 mA/cm^2 [44]. A total thickness of the i-a-Si:H top cell was reported of 230 nm and the bottom cell with a thickness

of around 2μ has a crystallinity grading as is shown in 3.1 by ϕ_c. The total cell delivers a high V_{oc} of 1.444 $Volt$, combined with an initial J_{sc} of 13.69 mA/cm^2.

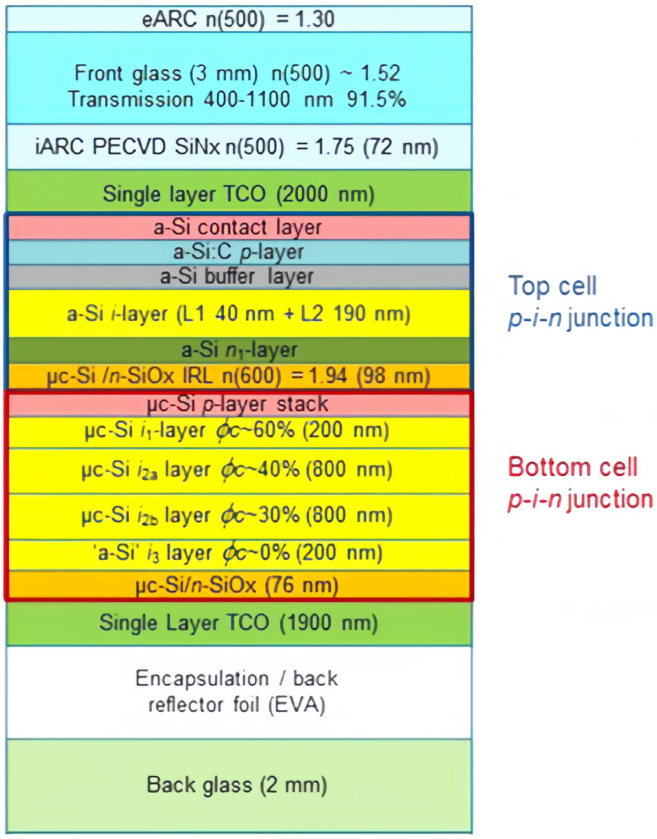

Figure 3.1: A schematic cross-section of the record module sized a-Si:H/nc-Si:H cell developed at TEL [44].

The world record p-i-n lab scale a-SiH/nc-Si:H solar cell was processed by AIST in Japan, with a stabilised efficiency of 12.69%. This cell uses an a-Si:H absorber layer processed at an excitation frequency of $60MHz$ with a power density of $30mW/cm^2$. This solar cell does not use a high-bandgap top cell, as the V_{oc} of the top a-Si:H top cell was reported to be 0.876 $Volt$.

3.1.3. Ion bombardment

A good understanding of the processing method is important to explain the obtained results from the experiments. In PECVD reactors Ions (electrically charged particles) are accelerated through the application of an electric field, thus giving the ions a "*considerable amount of energy*" as reported in [45]. Neutral particles, also present in the plasma, will not be accelerated as they are not charged and thus not affected by an electric field. The ions present in the plasma will have the most kinetic energy as they are bombarding the surface of the substrate present in the deposition chamber. When highly energetic Ions impact priorly deposited films, such as (p)-type layers they can "*enhance or induce processes such as surface species migration, displacement of surface and bulk atoms, and sputtering*" [45]. For a-Si:H films binding energy values of several eV are found and Ions with energy higher than $5eV$ are found to be sufficiently energetic to change the deposited films. In PECVD chambers many different ions are present, all of which impact the surface with different amounts of energy depending on applied power, applied frequency (RF vs VHF) and the pressure in the deposition chamber. Both RF-PECVD and VHF-PECVD chambers have bimodal ion energy distributions, which essentially means that there are two peaks in the ion energy distribution as illustrated in 3.2 where E is the ion energy on the x-axis and the $f(E)$ shows how many times an ion with a specific amount of energy is present. This distribution as well as the position of the peaks are dependent on pressure, applied power and applied frequency and can therefore be tuned when changed [45].

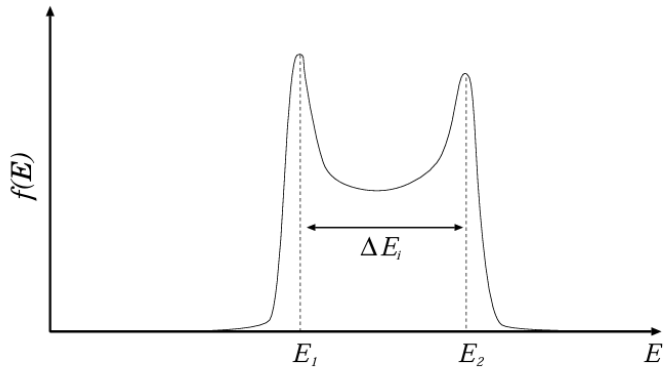

Figure 3.2: A bimodal distribution, which can be applied to the ion energy distribution of RF- and VHF-PECVD chambers [46].

When the ion energy distribution in the plasma can be changed, also the energy with which ions hit the substrate in the deposition chamber can thus be changed. In general, higher applied power leads to more energetic impacts of the ion bombardment, whereas higher pressure and higher applied frequency decrease the energy of the ion bombardment, also known as quenching [45].

3.1.4. Intrinsic Silicon-oxide buffer layer

An i-SiOx (intrinsic silicon-oxide) has been explored as a buffer layer between the p-i interface for a-Si:H solar cells. The main advantages of using such as buffer layer can be found in improved J_{sc} (short-circuit current density) and gains in the spectral response of the blue region for a single chamber configuration. The buffer layer is understood to prevent boron cross-contamination at the p-i interface and is shown to be a wide bandgap material, thus avoiding parasitic absorption. The importance of the p-i layer to the V_{oC} of a-Si:H solar cells is mentioned, however, no decisive reasoning is given [47]. Boron cross-contamination is also suspected to play a role in the processing of high bandgap a-Si:H via the use of a VHF-PECVD chamber. Even though at the PECVD cluster tool of TU Delft a multi-chamber setup is used which should limit cross-contamination, the effect of boron in the intrinsic absorber layer still seemed to be present. Therefore it was decided to test if an i-SiOx buffer layer with varying thicknesses could also work when the i-a-Si:H absorber layer is deposited using a VHF-PECVD chamber in a p-i-n (superstrate) configuration.

3.2. Experiments

In this section, an overview of experiment 1, performed on the i-SiO_x buffer layer, will be discussed. Furthermore, three series of experiment 2, a power and pressure series for the high-energy bandgap amorphous silicon will be discussed.

3.2.1. Very high-frequency processing of high-bandgap amorphous silicon solar cells

Asahi substrates with a commercially available FTO TCO are used and the intrinsic absorber layer of the solar cells is made using a VHF-PECVD chamber at 40.68MHz. The process is used to deposit high-bandgap amorphous silicon solar cells, in most cases a-Si:H is usually processed at a radio frequency (RF) of 13.56 MHz. This set of experiments was conducted after finding out there might be potential in processing high-bandgap a-Si H solar cells under high pressure and power. However, at early attempts of processing high-bandgap a-Si:H solar cells a poor spectral response in the blue region was observed as shown in 3.6. As can be seen in Figure 3.3, a-Si H single junctions absorb light between 300-800nm. For a tandem cell with a comparable a-Si:H top cell the absorption of light is far lower between 600-800nm as there is no metallic contact behind the silicon absorber layer of the top cell in tandem configurations. For top cells in tandem devices therefore the absorption in the 300-600nm wavelength range is crucial for good device performance.

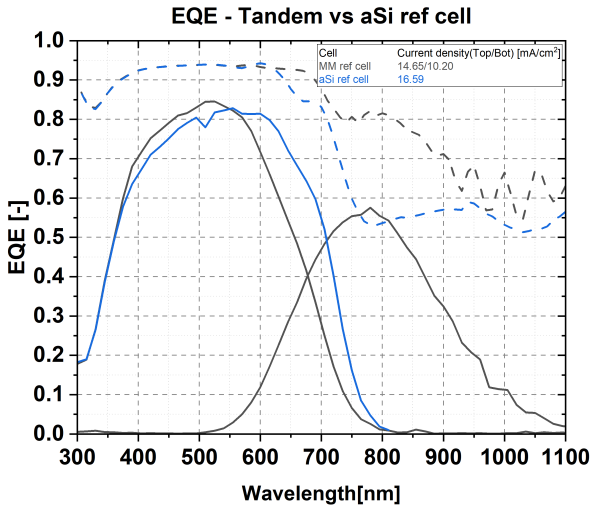

Figure 3.3: A comparison of the spectral response of a low-bandgap a-Si:H single junction and a tandem cell of a low-bandgap a-Si:H top cell and a nc-Si:H bottom cell, both processed on Asahi Vu substrates.

In this set of experiments first, an i-SiO_x layer is tested as a buffer layer with varying thicknesses between the p-i interface to improve the blue response of the high bandgap amorphous silicon solar cells as this has been shown to work for a-Si:H cells processed under RF conditions [47]. The second set of experiments explores the possibilities of improving the blue response of the solar cells by varying the deposition conditions of the solar cells by changing the power and pressure used in the deposition chamber. The solar cell structure used is a p-i-n (superstrate) configuration as shown in 3.4 with Asahi VU substrates, which have Fluorine doped Tin Oxide (FTO) as TCO. P and N layers of nc-SiOx are used as these layers are more transmissive than nc-SiC layers [4].

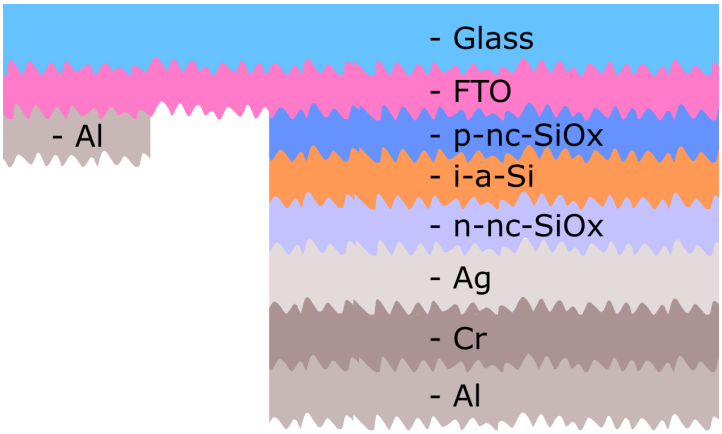

Figure 3.4: A schematic cross-section of the a-Si single junction device structure used in the VHF deposition

3.2.2. experiment 1: buffer layer thickness between p-i interface

To improve the spectral response of the blue region of processed high-bandgap a-Si:H solar cells an i-SiO_x buffer layer was proposed. In previously performed experiments the i-SiOx buffer layer has proven to work for single chamber deposition processes [47]. An experiment was conducted to test whether the buffer layer would work for the processing conditions used to create the VHF high bandgap a-Si:H. An i-SiO_x buffer layer of varying thickness was used to try and prevent boron tailing in the intrinsic absorber layer of the amorphous silicon solar cells.

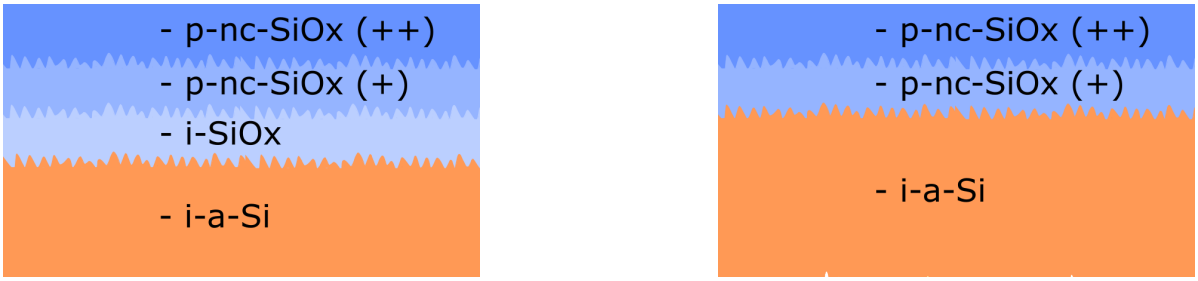

Figure 3.5: A schematic cross-section of a the p-i interface with an i-SiO_x buffer in (a) and without an i-SiO_x buffer layer in (b).

In this experiment, it was decided to deposit buffer layers varying from 3-27 nm with an interval of 6nm. The thickness of the buffer layer could impact the suspected boron-tailing in the intrinsic amorphous silicon absorber layer and might therefore improve the blue response of the solar cell.

Pressure [$mbar$]	RF Power [W]	SiH4 flow [$Sccm$]	CO2 flow [$Sccm$]	H2 flow [$Sccm$]
2.2	12	0.8	2	170

Table 3.1: Table with the processing conditions for the i-SiO_x buffer layer of the samples with different i-SiO_x thickness buffer layers.

Table 3.2 shows the processing parameters used for the intrinsic amorphous silicon absorber layer for the solar cells deposited for experiment 1.

Pressure	VHF Power	Power density	SiH4 flow	H2 flow	Substrate
[$mbar$]	[W]	[mW/cm^2]	[$Sccm$]	[$Sccm$]	-
4	40	400	6	60	Asahi

Table 3.2: Table with the processing conditions for the intrinsic amorphous silicon absorber layer of the samples with different i-SiO_x thickness buffer layers.

All doped layers are processed under the same conditions, the full list of deposition conditions for this experiment can be found in Appendix B.1.

3.2.3. experiment 2: power and pressure series

A power and pressure series was made to see if the ion bombardment in the plasma of the deposition chamber could have been too energetic. A possible cause of the loss of absorption in the blue region could be that during deposition the ion bombardment releases previously deposited boron atoms back into the plasma. This could happen when the ions that are accelerated towards the substrate have too much energy. A consequence of this could be that when the i-a-Si is deposited, parts of the p-doped layer are etched away thus damaging the p-layer and bringing boron back into plasma. Boron that is once again present in the plasma can then be deposited again, resulting in a boron tail of continuously decreasing concentrations of boron in the supposedly intrinsic amorphous silicon absorber layer. The boron tail will make the i-a-Si slightly doped, so it will be slightly p-doped. When the intrinsic absorber layer is p-doped, there will be more holes, which will mean higher recombination rates and thus a lower EQE. Performing depositions with lower power might reduce the force of the ion bombardment and thus reduce the amount of boron atoms that break free which could reduce the boron tailing. All doped layers are processed under the same conditions, the full list of deposition conditions for this experiment can be found in Appendix B.2. Table 3.3 shows the processing parameters used for the intrinsic amorphous silicon absorber layer for the solar cells deposited for series 1 of experiment 2. In the first series, the lowest power densities are used for which a plasma can be ignited. For reference, the 4$mbar$ that was initially used, the power density was brought back to 200mW/cm^2 from the original 400mW/cm^2.

Pressure	VHF Power	Power density	SiH4 flow	H2 flow	Substrate
[$mbar$]	[W]	[mW/cm^2]	[$Sccm$]	[$Sccm$]	-
9	40	400	6	60	Asahi
8	30	300	6	60	Asahi
7	30	300	6	60	Asahi
6	25	250	6	60	Asahi
5	20	200	6	60	Asahi
4	20	200	6	60	Asahi
3	15	150	6	60	Asahi

Table 3.3: Table with the processing conditions for the intrinsic amorphous silicon absorber layer of series 1 of experiment 2.

Table 3.4 shows the processing parameters used for the intrinsic amorphous silicon absorber layer for the solar cells deposited for series 2 and 3 of experiment 2. Here a slight increase in the power density is shown, where the power density increased again from 200mW/cm^2 to 250mW/cm^2 for the 4$mbar$ sample.

Pressure	VHF Power	Power density	SiH4 flow	H2 flow	Substrate
[$mbar$]	[W]	[mW/cm^2]	[$Sccm$]	[$Sccm$]	-
7	35	350	6	60	Asahi
6	30	300	6	60	Asahi
5	25	250	6	60	Asahi
4	25	250	6	60	Asahi
3	20	200	6	60	Asahi
5	28	280	6	60	Asahi

Table 3.4: Table with the processing conditions for the intrinsic amorphous silicon absorber layer of series 2 and 3 of experiment 2.

3.3. Results and discussion

In this section, the results of the experiments on the response of the VHF amorphous silicon solar cells will be discussed. First, the results of the i-SiO_x buffer layer experiment will be shown with a possible explanation for the obtained results. Secondly, the results of the power and pressure series experiment for the VHF amorphous silicon solar cells will be discussed.

3.3.1. Very high-frequency processing of high bandgap amorphous silicon solar cells

Initial high bandgap depositions using a VHF frequency plasma yielded working solar cells, however, their poor spectral response (EQE) in the blue region limits their use for tandem solar cells. The current density obtained by one of these solar cells of 11.63 mA/cm^2 is shown in 3.6 (add processing parameters and electrical performance of cell). In contrast to [48] no SIMS (Secondary Ion Mass Spectrometry) was performed as no such machine in a working state is present at TU Delft. However, by using EQE measurements, spectral losses in the blue region can still be shown and used as a metric to test deposition conditions.

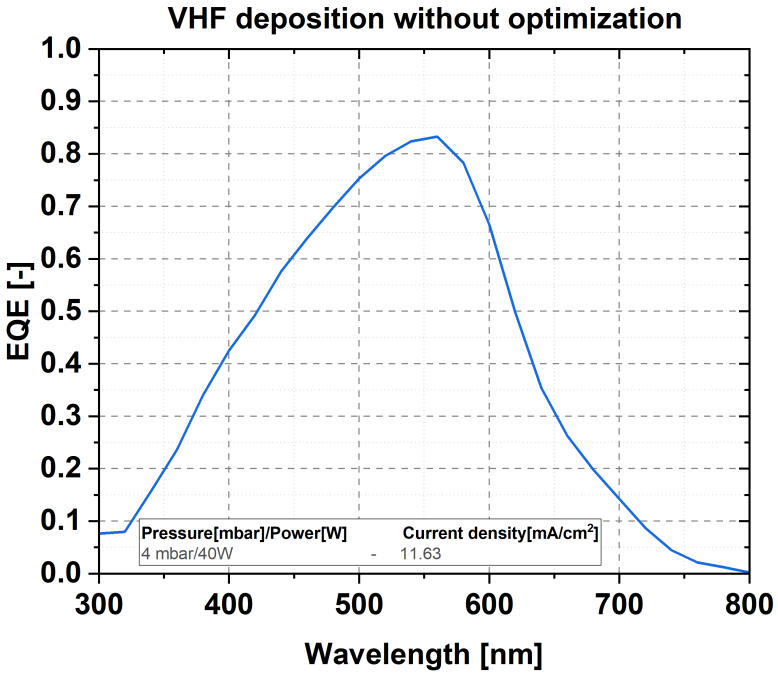

Figure 3.6: The EQE of a high power and pressure deposition, showcasing the poor blue response.

Pressure [$mbar$]	VHF Power [W]	i-SiO$_x$ thickness [nm]	VoC [V]	Jsc [mA/cm^2]	FF[$-$]
4	40	3	0.93	14.03	0.63
4	40	9	0.93	14.74	0.67
4	40	15	0.93	13.69	0.62
4	40	21	0.94	14.00	0.62
4	40	27	0.93	14.60	0.64

Table 3.5: Table with an overview of the processing conditions and key electrical parameters obtained from experiment 1.

As shown in Figure 3.7 a thickness increase of the i-SiO$_x$ buffer layer does not improve the blue response of the high-bandgap amorphous silicon solar cells. The ion bombardment has most likely destroyed or penetrated the thicker buffer layer and the loosely bound boron atoms have most likely been partially deposited in the intrinsic absorber layer of the solar cells. The diffusion of boron into the absorber can not be proven without any doubt due to the lack of a SIMS (Secondary Ion Mass Spectrometry) measurement, which was not performed due to time constraints, equipment availability and high costs. However, the poor response in the 400 nm to 600 nm wavelength range indicates that most likely more charge carriers are lost due to recombination at the front of the solar cell than is to be expected from a good functioning cell. The high V_{oc} of the solar cells indicates actual high band-gap a-Si:H solar cells have been made, however, their relatively low currents or around 14 mA/cm^2 and low fill factors indicate room for improvement.

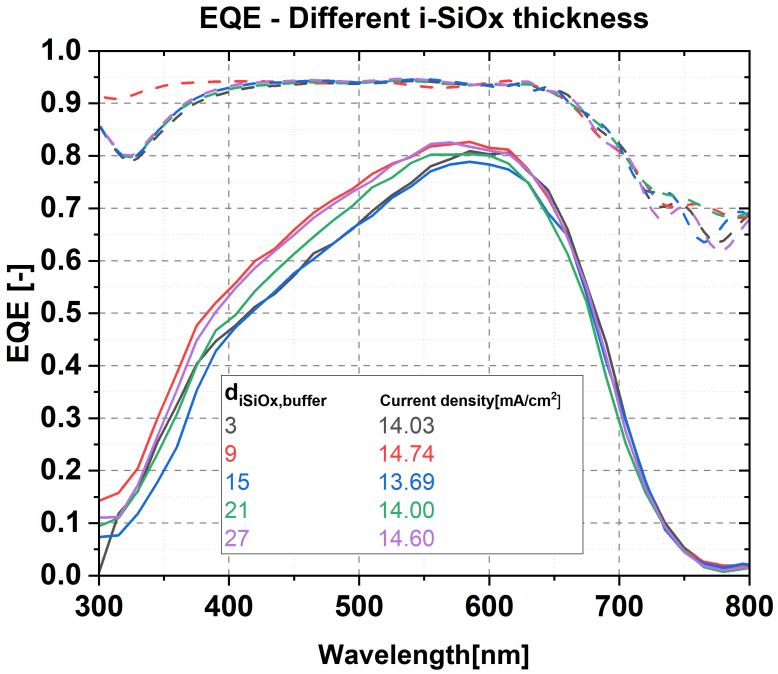

Figure 3.7: The EQE and 1-R measurements of the samples with increasing i-SiO_x buffer layer thicknesses.

As was demonstrated in Figure 3.7 a thicker buffer layer of i-SiO_x was shown to be ineffective in improving the spectral response of the high-bandgap amorphous silicon solar cells deposited with a VHF plasma. This suggests that the deposition conditions used are arguably too violent as the buffer layer did not act as such. In the second experiment, it was decided to change processing conditions in the VHF chamber used to deposit the high-bandgap amorphous silicon. The reason to go for lower power settings and different pressures is that the ion bombardment will be quenched, which should keep the doped P-layer on the substrate intact, thus preventing boron cross-contamination.

3.3.2. Series 1 of experiment 2, power and pressure series for high bandgap a-Si:H solar cells processed in a VHF-PECVD chamber.

A complex process involving power, pressure, electrode distance and gas flows needs to be tuned to obtain a stable plasma in the deposition chamber [49]. In the next experiment both the electrode distance and gas flows are fixed and only the applied power and pressure are changed as seen in Table 3.6. The parameters chosen for the experiment were obtained by performing a visual check over a range of different power and pressure combinations to verify what the lowest power/pressure combinations are for which a (stable) plasma could be achieved. The results of these visual observations are shown in Figure 3.8, where the purple dots show a ”Good plasma”, the purple stars show a ”Flickering plasma” and the crosses indicate ”No plasma”.

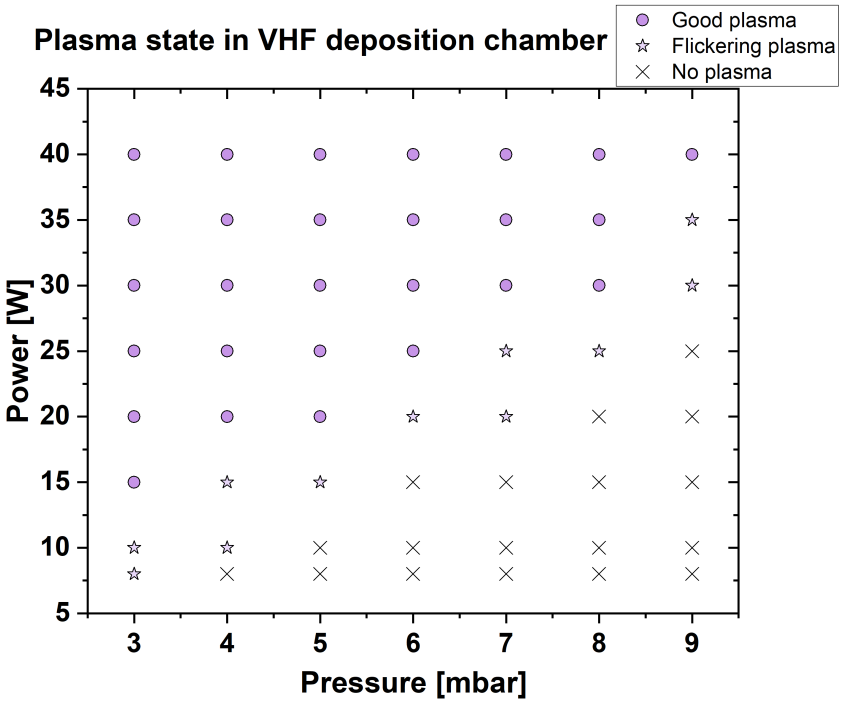

Figure 3.8: Plasma state based on visual observations where ”Good plasma”, ”Flickering plasma” and ”no plasma” are indicators

Based on Figure 3.8 the decision was made to make a power and pressure series of the lowest power for each pressure that can generate a visually stable plasma. An overview of the processing parameters for the power/pressure series can be seen in Table 3.6

Pressure [$mbar$]	VHF Power [W]	SiH4 flow [$Sccm$]	H2 flow [$Sccm$]	Substrate
9	40	6	60	Asahi
8	30	6	60	Asahi
7	30	6	60	Asahi
6	25	6	60	Asahi
5	20	6	60	Asahi
4	20	6	60	Asahi
3	15	6	60	Asahi

Table 3.6: Table with an overview of the processing conditions of series 1 of experiment 2.

The key electrical properties obtained from the samples processed with the condition shown in 3.7 are split into two separate Figures to keep a clear overview. In Figure 3.9 the EQE of respectively the [7$mbar$/30W], [8$mbar$/30W] and the [9$mbar$/40W] are shown. In Figure 3.10 the EQE of respectively the [3$mbar$/15W], [4$mbar$/20W], [5$mbar$/20W] and [6$mbar$/25W] are shown.

Pressure [$mbar$]	VHF Power [W]	VoC [V]	Jsc [mA/cm^2]	FF[$-$]
9	40	0.83	11.87	0.59
8	30	0.74	13.08	0.57
7	30	0.77	13.40	0.25
6	25	0.90	13.69	0.66
5	20	0.86	14.75	0.60
4	20	0.89	15.36	0.69
3	15	0.89	14.63	0.66

Table 3.7: Table with an overview of the electrical performance of Series 1.

Figure 3.9 shows the [7$mbar$/30W], [8$mbar$/30W] and the [9$mbar$/40W] samples all have a good blue response, however, when the electrical properties are considered from Table 3.7 it can be concluded that for these processing parameters, it was not possible to create a high bandgap absorber layer as the Voc's are lower than for normal aSi. The ion bombardment was quenched enough here to prevent boron atoms from being released from the P-layer back into the plasma where they could be redeposited in the intrinsic absorber layer. However, also the properties of the deposited film are changed when the power of the ion bombardment is changed, resulting in this case in the lower observed V_{oc}'s.

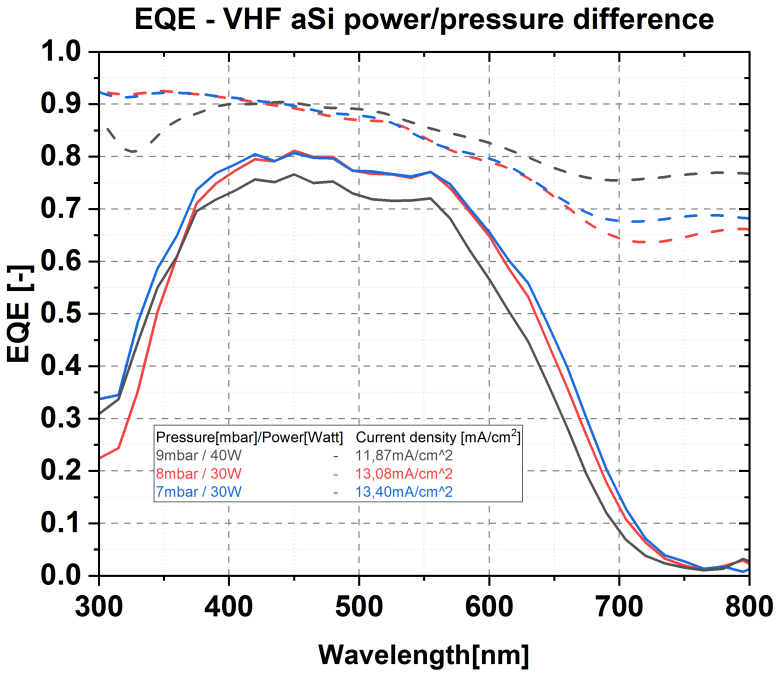

Figure 3.9: EQE and 1-R measurements of the [9$mbar$/40W],[8$mbar$/30W] and [7$mbar$/30W] samples from series 1.

Figure 3.10 shows a significant difference in the blue response of the processed cells. Firstly, the [3$mbar$/15W] sample, which reaches an EQE of 0.56 at 400nm shows the poorest spectral response. Secondly, the [4$mbar$/20W] and the [5$mbar$/20W] show similar responses below 400nm. However, at 400nm the [4$mbar$/20W] shows a spectral response of 0.68 whereas the [6$mbar$/25W] shows a slightly worse response of 0.65, for longer wavelengths the [4$mbar$/20W] sample shows an increasingly better response. The sample that stands out here is the [5$mbar$/20W], it shows the best obtained EQE value of 0.75 at 400nm and a current density of 14.75 mA/cm^2. The other cells show worse performance at 400 nm as the [3$mbar$/15W] sample only has an obtained EQE of 0.55 and the [4$mbar$/20W] and [5$mbar$/20W] of 0.68 and 0.64 respectively. This indicates that the most favourable condition from this experiment is [5$mbar$/20W] as the other samples seem to be suffering from boron cross-contamination. The V_{oc} of the [5$mbar$/20W] sample is, however, the lowest at just 0.86V, therefore it can not be considered high-bandgap a-Si:H. The results of 3.7 show that the most interesting pressures seem to

be between 3 and 6 $mbar$ as most of these samples show relatively good EQE's, current density, FF and the highest obtained V_{oc}'s of the series.

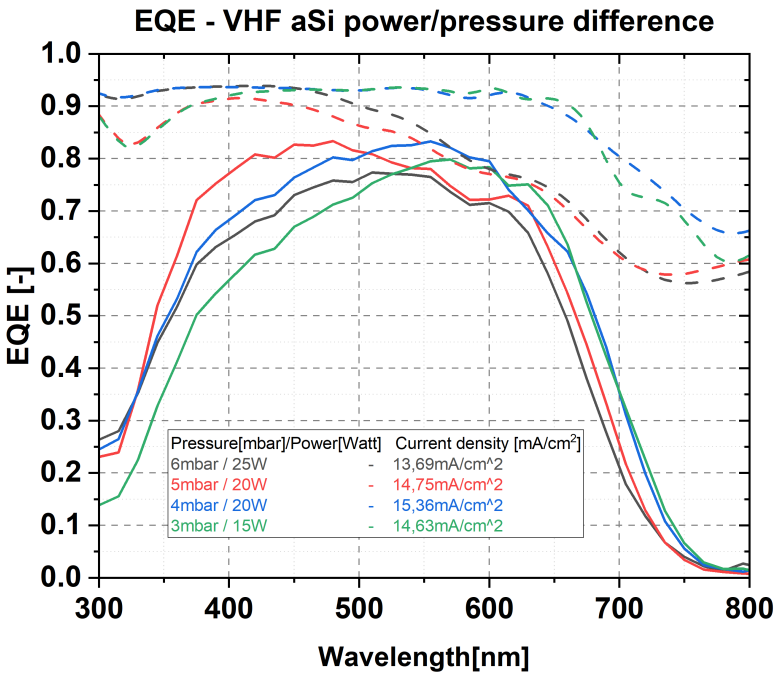

Figure 3.10: EQE and 1-R measurements of the [6$mbar$/25W],[5$mbar$/20W],[4$mbar$/20W] and [3$mbar$/15W] samples from series 1.

3.3.3. Series 2 of experiment 2, power and pressure series for high bandgap a-Si:H solar cells processed in a VHF-PECVD chamber.

After characterization of the samples processed with the parameters from 3.6, it was chosen to explore deposition conditions under higher applied power. As it is desired to avoid ion bombardment with high applied power, a choice was made to only slightly increase the power by 5W for the pressures ranging from 3 to 6 $mbar$ as these samples show the most potential due to their higher V_{oc} and in case of the [5$mbar$/20W] good response in the blue region of the solar spectrum. Higher applied power can improve the stability of the plasma and thus the quality of the deposited layer. The trade-off here is that this could also lead to a more violent ion bombardment at the surface of the substrate. A new set of samples was deposited to find more favourable deposition conditions. The processing parameters for the next set of experiments are shown in Table 3.8.

Pressure [$mbar$]	VHF Power [W]	SiH4 flow [$Sccm$]	H2 flow [$Sccm$]	Substrate
7	35	6	60	Asahi
6	30	6	60	Asahi
5	25	6	60	Asahi
4	25	6	60	Asahi
3	20	6	60	Asahi
5	28	6	60	Asahi

Table 3.8: Table with an overview of the processing conditions of series 2 of experiment 2.

The key electrical properties obtained from the samples processed with the condition shown in 3.9 are split into two separate Figures to keep a clear overview. In Figure 3.11 the EQE of respectively the [7$mbar$/35W] and the [6$mbar$/30W] samples are shown. In Figure 3.12 the EQE of respectively the

[3$mbar$/20W], [4$mbar$/25W] and [5$mbar$/25W] are shown.

Pressure [$mbar$]	VHF Power [W]	VoC [V]	Jsc [mA/cm^2]	FF[$-$]
7	35	0.90	13.36	0.66
6	30	0.89	14.55	0.66
5	25	0.91	14.60	0.68
4	25	0.88	14.59	0.58
3	20	0.91	15.43	0.63
5	28	0.91	14.75	0.65

Table 3.9: Table with an overview of the electrical performance of Series 2.

In Figure 3.11 the results of the deposition at [6$mbar$/30W] and [7$mbar$/35W] are shown. Both samples show good response till 500 nm after which the [6$mbar$/30W] sample becomes significantly better leading to a higher total current density of 14.55mA/cm^2 when compared to the 13.56mA/cm^2 of the [7$mbar$/35W]. However, when looking at the overall results from the second part of the experiment as shown in 3.9 it can be seen that the [5$mbar$/25W] is performing better, with both higher V_{oc} and a higher obtained current density.

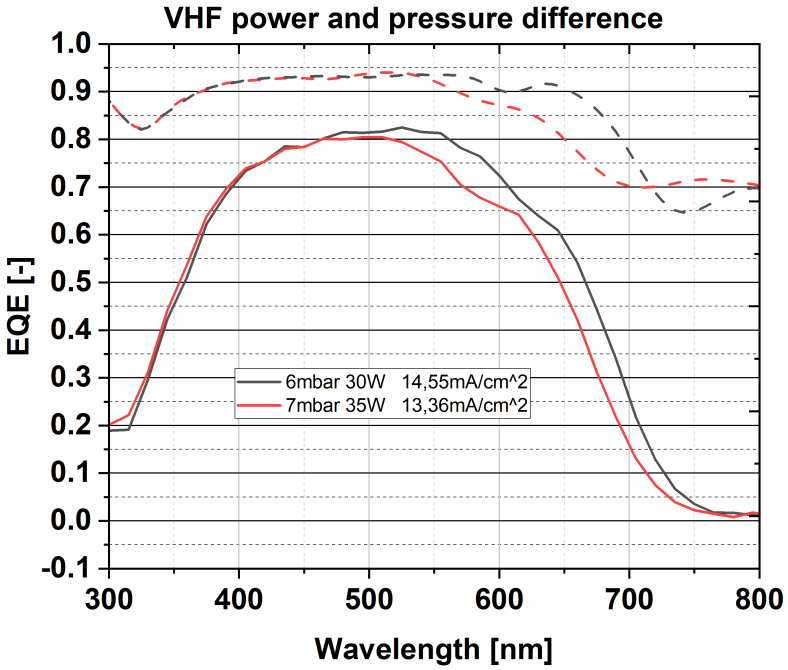

Figure 3.11: EQE and 1-R measurements of the [7$mbar$/35W] and [6$mbar$/30W] samples from series 2.

In Figure 3.12 the spectral response of the [3$mbar$/20W], [4$mbar$/25W] and [5$mbar$/25W] are shown. Especially the [3$mbar$/20W) sample shows a poor response in the blue region with the [4$mbar$/25W] performing better, albeit both have poor spectral responses at 400nm of 0.6 and 0.52 respectively. The [5$mbar$/25W] sample shows the most promising response in the blue region which makes it the most interesting option for tandem cell applications. To explore further possibilities of a 5$mbar$ processing regime it was chosen to proceed with a sample with higher applied power at 5$mbar$ of 28W to explore the maximum applied power for a high-quality absorber layer.

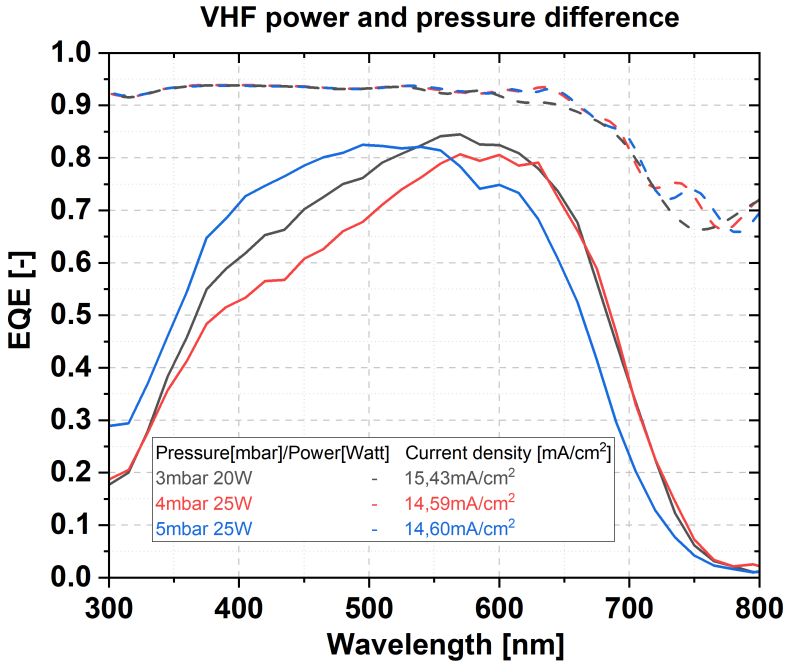

Figure 3.12: EQE and 1-R measurements of the [5$mbar$/25W],[4$mbar$/25W] and [3$mbar$/20W] samples from series 2.

3.3.4. Series 3 of experiment 2, power series for high bandgap a-Si:H solar cells processed in a VHF-PECVD chamber.

The optical performance of the samples processed at 5$mbar$ and 20,25 and 28W are shown in 3.13 and a clear trend can be observed where the highest applied power of 28W shows the worst blue response, followed by the 25W sample and finally the 20W sample showing the best spectral response in the blue region. For comparison, the 20W sample achieves a spectral response of 0.77, whereas the 25W achieves 0.70 and the 28W drops to 0.59 thus showing a trend. This can be explained by the energy of the ions bombarding the surface of the substrate on which the p P-layer has been deposited before the deposition of the intrinsic absorber layer. As the power increases the energy of the ion bombardment increases as in this experiment pressure and frequency are kept constant. The lowest energetic ions, when 20W of power is applied, have the least energetic impact on the P-layer and thus cause the least amount of boron contamination in the intrinsic absorber layer. The highest energetic ions, when 28W of power is applied, have the most energetic impact and thus cause the most amount of boron contamination in the intrinsic absorber layer leading to a loss of blue response of this sample. However, the electrical performance of the solar cells must also be considered here, since the 20W sample also has the lowest V_{oc} of just 0.86V it can thus not be considered as high bandgap aSi. This means that the 5 mbar and 25W with an obtained Voc of 0.91V should be considered the best-performing high bandgap aSi solar cell obtained in the experiments.

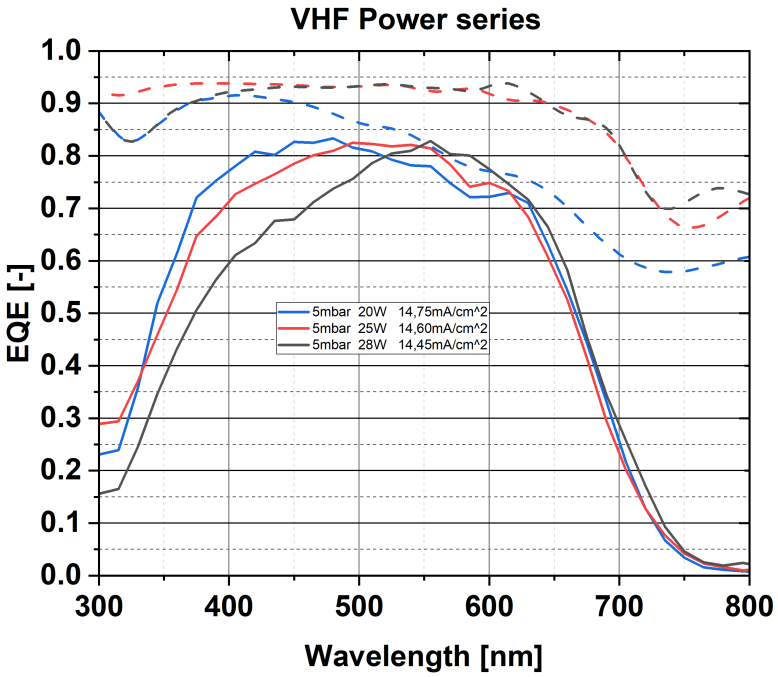

Figure 3.13: EQE and 1-R measurements of the [5$mbar$/20W],[5$mbar$/25W] and [5$mbar$/28W] samples from series 3.

3.4. conclusion

In experiment 1 the potential of an i-SiOx buffer layer was explored to prevent boron contamination of the intrinsic absorber layer of a high-bandgap a-Si:H solar cell. A series of buffer layers, varying in thickness from 3 nm to 27 nm with steps of 6nm were processed and characterized. From the results obtained, it can be concluded that independent of the thickness of the i-SiO_x buffer layer, the blue response of all the cells was compromised and therefore the buffer layer did not succeed in preventing boron contamination of the intrinsic absorber layer.
In experiment 2 the applied power and pressure in the deposition chamber were changed to prevent boron contamination of the intrinsic absorber layer through reducing the energy of the ion bombardment. The lowest applied power and pressure combinations were found for which plasmas could be ignited for a VHF frequency of 40.68MHz. Two series of power and pressure combinations were processed, the first series consisted of the absolute lowest power/pressure combinations which showed there is a likely optimum between 3 and 6$mbar$. After increasing the applied power by 5W for these power/pressure combinations it was found that at [5$mbar$/25W] the best-performing cell was found. To explore if higher applied power would further improve the cell a [5$mbar$/28W] was processed, this showed however that 28W is too much power and the ion bombardment causes too much boron contamination of the intrinsic absorber layer. The [5$mbar$/25W] gave the best performance of the cells processed when considering both optical and electrical performance with a V_{oc} of 0.91V, FF of 0.68 and a J_{sc} of 14.60 mA/cm^2.

4

High-efficiency single junction a-Si:H and nc-Si:H solar cells for tandem applications

In this Chapter, various methods to improve single junction a-Si:H and nc-Si:H will be discussed, which can also be adapted for use in a-Si:H/nc-Si:H tandem solar cells. Light trapping properties of different textures will be examined by the use of solar cells deposited on different textured substrates, both 1-R curves and obtained J_{sc}'s from EQE measurements will be compared. Similar measurements will be performed for different configurations of a so-called bilayer TCO, where the thickness of the IOH layer will be kept constant and the thickness of the i-ZnO layer is varied, the goal is to obtain the highest absorption and highest possible J_{sc}'s by better light trapping. Finally, the use of an i-ZnO back reflector is examined, which is also varied in thickness to see if better reflection at the back of the solar cells can be obtained, which is another method of increasing J_{sc}'s. First, a literature review will show previous research done on achieving high J_{sc} by the use of textured glass substrates, thickness of TCO and back reflector. Second, the measurements of several experiments will be shown to highlight which substrate, TCO and thickness of the back reflector are performing best. Third, a conclusion is presented based on the results and motivation for the final chosen substrate is presented.

4.1. Literature review

In this section, a literature review on micro and nano-featured glass substrates is presented as well as the use of TCO material in the record module. The use of i-ZnO is investigated as part of a bilayer TCO as well as the its use as a back reflector.

4.1.1. Micro and nano-features on glass substrates

Comparisons between EAZO(nano-features), EG(micro-features) and MST(combination of micro and nano features) glass textures have been made for use on nc-Si:H solar cells, where EG textures (comparable to ITO tex) have been found to deliver the highest V_{oc} and J_{sc}. Micro-featured glass substrates are optically inferior to nano-featured glass substrates for light scattering at low angles. The electrical performance of nc-Si:H cells deposited on Micro-features, however, outperformed those deposited on nano-featured substrates. Micro-features are relatively large with respect to the thickness of nc-Si:H layers and even more so for a-Si:H layers, therefore, these textures have been found not to degrade the electrical performance of solar cells. Nano-features are relatively small with respect to the thickness of a-Si:H layers, however, they can degrade the electrical performance of solar cells by causing cracks. These cracks are likely cause by the extra roughness these nano-features add to the substrate, whereas micro-textures are relatively smooth as they are relatively large when compared to the thickness of a-Si:H layers. Combinations of micro and nano features can improve light scattering, however, so far no gain in solar cell performance has been observed [4].

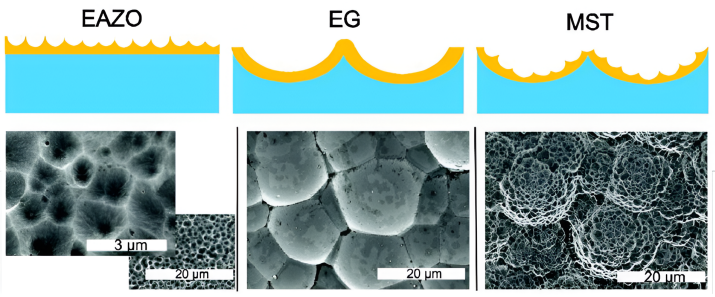

Figure 4.1: The textures with nano-features (EAZO), micro-feature (EG) and double texture (MST) and their parameters used by Tan et al. [4].

Figure 4.1 shows the schematic cross section and top down SEM images of the textures used Tan et al. [4]. Thick absorber layers are mentioned to be ineffective in acquiring both high V_{oc} as well as FF. To still obtain high currents, the glass texture is of vital importance. A trade off between light scattering by nano-features on glass and their impact on V_{oc} and FF shows there is trade off for nc-Si:H cells between light trapping and electrical performance [4].

4.1.2. Record a-Si:H/nc-Si:H solar module

The record cell produced by TEL solar, earlier discussed in Section 3.1.2 uses a very thick 2μ front ZnO:B (Boron doped Zinc oxide) TCO as single layer TCO in combination with a 1.9μ ZnO:B thick back TCO layer. The front TCO, deposited using an LPCVD process, has good light-scattering properties with haze values reported at 45-50%. The use of boron-doped Zinc oxide is reported to play a significant role in parasitic absorption in both front and back layers in the produced modules, a trade-off is made between the conductivity of the single-layer TCO and the optical transmission.

4.1.3. IOH and i-ZnO as Bilayer TCO

The use of a bilayer TCO made of i-ZnO and IOH is proposed by prior research at Delft University of Technology. The characteristics of multiple TCO materials made with RF sputtering were researched and a bilayer, made out of a thin IOH layer as TCO_1 and a thick i-ZnO layer as TCO_2 has been shown to maximize the optoelectrical performance when compared to the use of single TCO layers. Several scattering mechanisms are proposed that could have an impact on the scattering effect of the i-ZnO layer, such as phonon scattering, grain boundary scattering and charged center scattering. Ideal deposition conditions of 25C° and 1.5W/cm^2 for the IOH and 200C° and 2.0W/cm^2 for the i-ZnO are proposed when using RF sputtering [50],[51].

4.1.4. i-ZnO as back reflector

A back reflector made of i-ZnO has been simulated to reduce plasmonic absorption from silver back contacts. For an effective back reflector, the refractive index of the material used should be very different to the material the light travels through before reaching the back reflector as described by the Fresnel equation. i-ZnO should work as a better back reflector when compared to AZO (Aluminium doped Zinc oxide), as i-ZnO absorbs less light due to the lower presence of free charge carriers as the Zinc-oxide is not doped [52], [53].

4.2. Experiments

In this section, the experimental setup of experiment 3 is presented which compares different glass textures which are used as substrates for the deposition of nc-Si:H solar cells. Experiment 4 is presented to find the impact of various thicknesses of i-ZnO as a bilayer on a-Si:H solar cells deposited on MST textured glass substrates is explained. The experimental setup for experiment 5, on the thickness of i-ZnO as part of a bilayer TCO on MST textured glass substrates is presented and finally, experiment 6, where i-ZnO is used as a back reflector is presented.

All i-ZnO layers are processed in an RF-Sputtering chamber at 13.56MHz, the other processing parameters can be found in 4.1. The thickness of deposited layers is measured by Spectral Ellipsometry, deposition times are then extrapolated as required to deposit the desired thickness.

Pressure [$mbar$]	RF Power [W]	Ar flow [$Sccm$]	Heater temperature [$C°$]
2.6	200	20	200

Table 4.1: Table with an overview of the processing conditions of the i-ZnO layer used in Chapter 2.

4.2.1. Experiment 3: Micro and nano-textured glass substrates for nc-Si:H solar cells

In experiment 3, a comparison is made between differently textured glass substrates on which a nc-Si:H solar cell is deposited. The textures used for this experiment are MST (modulated surface texture), i-ZnO texture and ITO texture, where i-ZnO and ITO are used as sacrificial material for the etching process. Images obtained from Atomic Force Measurements and Scanning Electron Microscopy are shown in Figure 4.2.

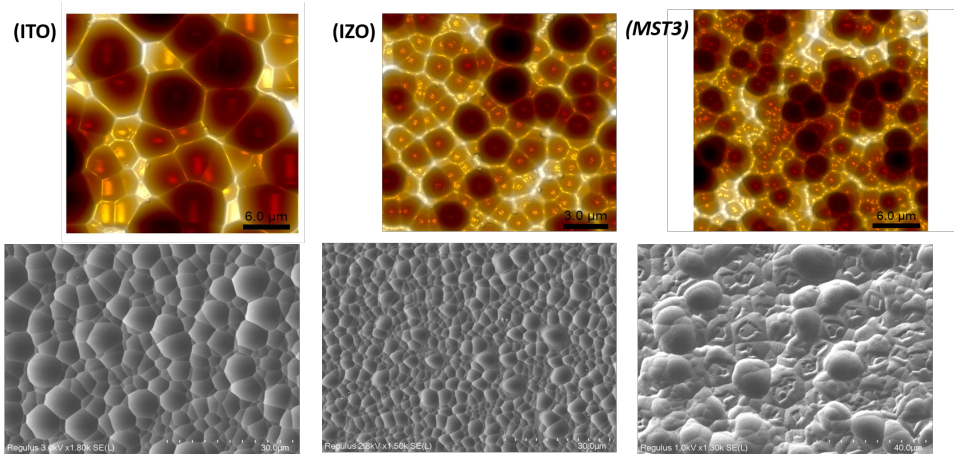

Figure 4.2: Top down AFM (Atomic force measurement) and SEM (Scanning Electron Microscope) images of the ITO,i-ZnO and MST texture used, not that the scale on the i-ZnO AFM is twice as small as on the ITO or MST textures [54]

A 150nm layer of IOH in combination with a thin i-ZnO buffer is used as TCO. Four p-i-n solar cells were deposited with the structure made of p-nc-SiO_x/i-nc-Si/n-nc-SiO_x, on the different textures. The devices use 2800nm i-nc-Si absorber layers made in a VHF-PECVD chamber at 40.68MHz with power, pressure and gas flows shown in Table 4.2. All doped layers are processed under the same conditions, the full list of deposition conditions for this experiment can be found in Appendix B.3. A 500nm i-ZnO back reflector is added to the back of the cells, the processing conditions for the i-ZnO back reflector are shown in Table 4.1. A schematic cross-section of the solar cell design is shown in Figure 4.3. The substrates are solely processed on separate holders in succession under the same deposition conditions. This experiment aims to find the best-performing substrates for nc-Si:H solar cells, both good optical and electrical properties are required to obtain high-performance nc-Si:H solar cells as shown by [4]. The performance of nc-Si:H solar cells is closely related to the performance of a-Si:H/nc-Si:H solar cells as both designs utilise the same part of the solar spectrum.

Pressure [$mbar$]	VHF Power [W]	SiH4 flow [$Sccm$]	H2 flow [$Sccm$]	SC [%]	Substrate
3.9	40	3.2	120	2.6	varying

Table 4.2: Table with an overview of the processing conditions of the i-nc-Si:H absorber layer used for the texture experiment 3.

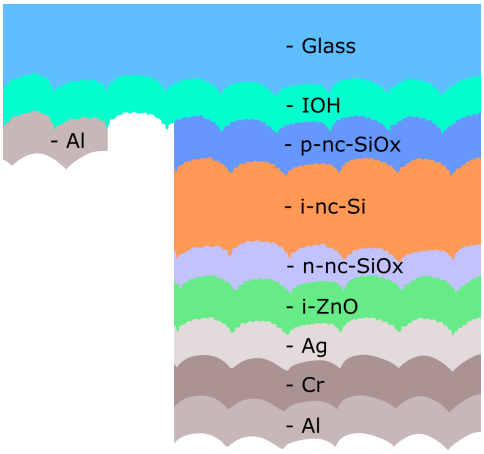

Figure 4.3: A schematic cross-section of the nc-Si:H solar cell design used in experiment 3.

4.2.2. Experiment 4: Shunt and front TCO configuration for a-Si:H solar cells on MST textured glass substrates

In experiment 4, a comparison is made between the performance of a-Si:H solar cells deposited on two MST textured substrates. Two MST textured substrates with 150nm IOH are used, on which i-ZnO layers of 3nm, 300nm,600nm or 900nm are deposited. Two a-Si:H solar cells were deposited using a RF-PECVD chamber at 13.56MHz with the p-i-n structure made of p-nc-SiOx/i-a-Si/n-nc-SiOx. Power, pressure and gas flows used for the 300nm i-a-Si:H are shown in Table 4.3. A 120nm i-ZnO back reflector is used, deposition conditions can be found in Table 4.1. The full list of deposition conditions for this experiment can be found in Appendix B.4. A schematic cross-section of the solar cell design is shown in Figure 4.5. The substrates are processed on two separate holders in succession. This experiment aims to show the performance of a-Si:H on MST textured substrates processed at TU Delft as in tandem configuration the a-Si:H cells showed to be underperforming in EQE (spectral response) measurements. Measurement errors in obtained EQE measurements are however easy to make for tandem solar cells when bias light or bias light intensities are incorrect. Furthermore, a lot of the processed tandem cells have a so-called energy barrier, where incorrect band alignment causes an S-shaped JV curve. Single junction a-Si:H cells were therefore deposited on MST textured glass substrates to better evaluate their performance. Another reason to look at a-Si:H solar cells on MST textured glass substrates is that initially an a-Si:H cell was completely shunted, which means it acts as a resistor rather than showing diode-like behaviour. Inspection with a SEM showed a possible shunt location as shown in Figure 4.4. .

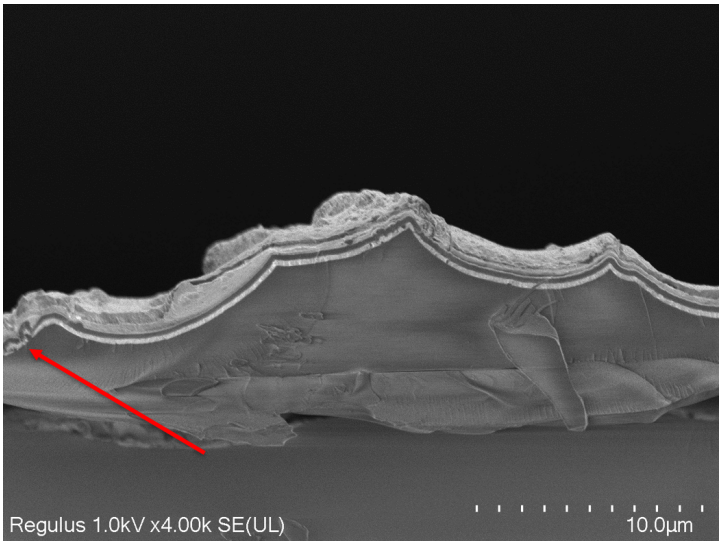

Figure 4.4: A cross-section of the shunted a-Si:H solar cell with a possible shunt location shown by the red arrow.

Pressure [$mbar$]	RF Power [W]	SiH4 flow [$Sccm$]	H2 flow [$Sccm$]	Substrate
0.7	2.8	40	0	MST

Table 4.3: Table with an overview of the processing conditions of the i-a-Si:H absorber layer used for the texture experiment 4.

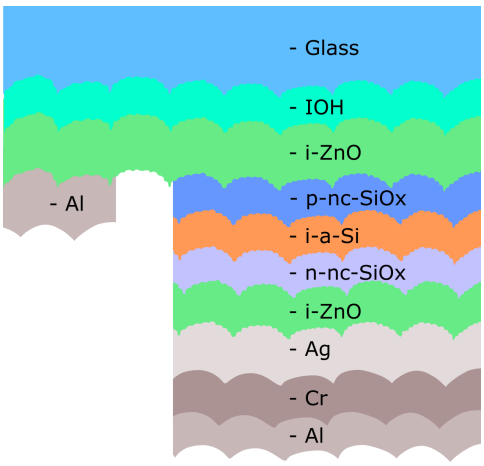

Figure 4.5: A schematic cross-section of the a-Si:H solar cell design used in experiment 4

4.2.3. Experiment 5: Thickness of i-ZnO as part of a bilayer TCO for nc-Si:H solar cells on MST textured glass substrates

In experiment 5, a comparison is made between different thicknesses of i-ZnO as part of a bilayer TCO on which a nc-Si:H solar cell is deposited. Four MST textured substrates were processed on two separate holders after the deposition of different thicknesses of i-ZnO on the front side of the substrates. Four MST textured substrates with 150 nm of IOH, on which i-ZnO layers of 500nm, 1000nm, 1500nm and 2000nm are deposited. Four p-i-n solar cells were deposited with the structure made of p-nc-SiOx/i-nc-Si/n-nc-SiOx, using 2800nm i-nc-Si absorber layers. The absorber layers are made in a VHF-PECVD chamber at 40.68MHz with power, pressure and gas flows used shown in Table 4.4. A 500nm i-ZnO back reflector is used, deposition conditions can be found in Table 4.1. The full list of deposition conditions for this experiment can be found in Appendix B.5. A schematic cross-section of the solar cell design is shown in **??**. The substrates are solely processed on four holders in succession. A bilayer configuration with 150nm of IOH and 500nm of i-ZnO was proposed to keep the thickness

similar to the TCO used at Hyet Solar for their solar foils [51]. In this experiment, thicker layers of i-ZnO are deposited to evaluate their effectiveness as an increase in scattering or a loss of electrical performance might be observed. A very thick layer of ZnO:B was reported to have a significant amount of parasitic absorption, the use of i-ZnO as part of a bilayer TCO might reduce the parasitic absorption. The downside of using intrinsic material instead of a doped zinc oxide can be compensated by the use of a bilayer TCO, to reduce the trade-off that normally has to be made for single layer TCO's.

Pressure [$mbar$]	VHF Power [W]	SiH4 flow [$Sccm$]	H2 flow [$Sccm$]	SC [%]	Substrate
3.9	40	3.2	133	2.2	MST

Table 4.4: Table with an overview of the processing conditions of the i-nc-Si:H absorber layer used for the texture experiment 5.

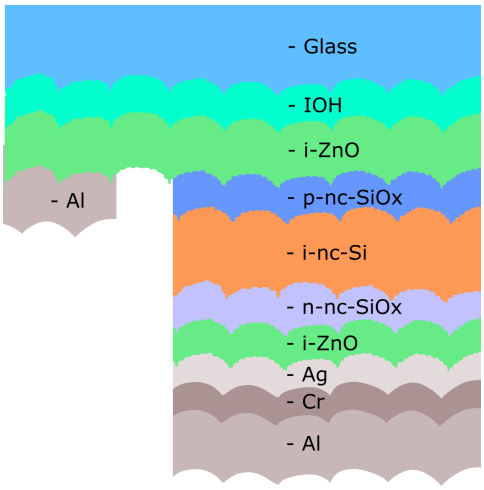

Figure 4.6: A schematic cross-section of the nc-Si:H solar cell design used in experiments 5 and 6

4.2.4. Experiment 6: Thickness variation of an i-ZnO back reflector for nc-Si:H solar cells on MST textured glass substrates

In experiment 6, a comparison is made between i-ZnO layers of varying thickness which is used as a back reflector. A 150nm layer of IOH in combination with a 2μ i-ZnO buffer is used as TCO. Three MST textured substrates were processed on the same holder on which p-i-n solar cells were deposited with the structure made of p-nc-SiOx/i-nc-Si/n-nc-SiOx, using 2800nm i-nc-Si absorber layers made in a VHF-PECVD chamber at 40.68MHz with power, pressure and gas flows used shown in Table 4.5. After deposition of the solar cells, i-ZnO layers of 60nm, 240 nm and 500nm were deposited, using the conditions shown in Appendix 4.1. The full list of deposition conditions for this experiment can be found in Table B.6. In this experiment, the effect of the various thicknesses of i-ZnO used as a back reflector is examined. The record efficiency module, shown in 3.1.2 features a 1.9μ back TCO which is likely chosen as a back reflector. The thick back TCO layer is mentioned to play a significant role in the total parasitic absorption of the solar module. The use of i-ZnO compared to the ZnO:B should help to minimize the parasitic absorption here as well. A schematic cross-section of the solar cell design is shown in 4.6. Simulations were only performed for an i-ZnO layer with a thickness of 80nm, the series processed should highlight any trends, if present. All three substrates were processed on a single holder for the deposition of the silicon layers.

Pressure [$mbar$]	VHF Power [W]	SiH4 flow [$Sccm$]	H2 flow [$Sccm$]	SC [%]	Substrate
3.9	40	3.2	133	2.2	varying

Table 4.5: Table with an overview of the processing conditions of the i-nc-Si:H absorber layer used for the texture experiment 6.

4.3. Results and discussion

In this section, the results and a discussion of experiment 3, where different glass substrates are compared, is presented. The results alongside a discussion of experiment 4 are presented, which tries to find the impact of various thicknesses of i-ZnO as a bilayer on a-Si:H solar cells deposited on MST textured glass substrates. The outcome of experiment 5 is shared and the results are discussed. Finally, experiment 6, which compares various thicknesses of i-ZnO used as a back reflector is presented and discussed.

4.3.1. Experiment 3: Micro and nano-textured glass substrates for nc-Si:H solar cells.

The key electrical characteristics of samples from experiment 3 are shown in Table 4.6 and show the difference obtained by performing several depositions of nc-Si:H single junction solar cells with intrinsic-nc-Si:H absorber layers of 3000nm processed in a VHF-PECVD chamber. From these first results, similar performance differences can be observed as shown by [4], where an ITO textured glass substrate outperforms the black MST3 texture as seen in both 4.7 and 4.8. The crystallinity ratio of the samples was determined by fitting raman spectroscopy measurements, the fits and normalized curves can be found in Appendix D.0.1.

Substrate type	**TCO/thickness[nm]**	**VoC [V]**	**Jsc [mA/cm^2]**	**FF[$-$]**	**X**[%]	η[%]
MST3	IOH/150	0.528	24.37	0.58	66	7.46
i-ZnO	IOH/150	0.533	23.94	0.58	66	7.40
ITO	IOH/150	0.541	25.21	0.62	57	8.46
MST3	IOH/150	0.536	22.23	0.60	57	7.15

Table 4.6: Table with an overview of the processing conditions and key electrical parameters obtained from experiment 1, the X is crystallinity in % and η shows the efficiency.

A higher J_{sc} of 25.21[mA/cm^2] was obtained for the ITO textured substrate compared to 24.37[mA/cm^2] for the MST textured substrate. Furthermore, a higher V_{oc} of 0.541V was obtained for the ITO textured substrate compared to 0.528V for the MST textured substrate. The i-ZnO textured substrate showed the lowest obtained current density at 23.94[mA/cm^2] with a V_{oc} of 0.533V. An extra reference MST3, the green sample in Figure 4.7 and 4.8, was processed to verify the results obtained for the MST3 substrate. This, however, did not improve the performance of the MST3 substrate. In table 4.6 the crystallinity of the samples is shown, noticeable are the higher crystallinity ratios for the MST and i-ZnO textured samples, therefore, they have a slightly lower V_{oc}. The nano-features on these textures are likely causing the i-nc-Si:H to be more crystalline due to the roughness of the surface being higher. Furthermore, their presence is likely also the reason for the drop in FF as the nano-features can cause cracks in the layer [4].

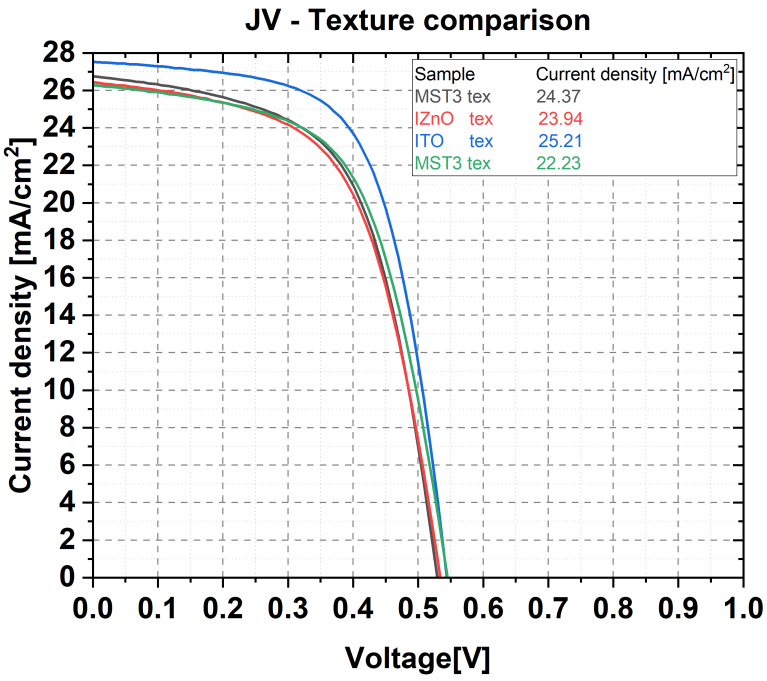

Figure 4.7: JV curves of the MST, i-ZnO and ITO textures from experiment 3.

Figure 4.7 shows the obtained JV curves from experiment 3, which shows a slight performance benefit for the ITO textured substrate when compared to the other textures. The obtained J_{sc}'s are calculated from EQE measurement and are therefore different to the J_{sc}'s from Figure 4.7. Similar trends can be observed both from the JV measurement and the EQE measurement, as in both cases the ITO textured substrate has better performance. Due to the slightly higher J_{sc} and V_{oc} of the ITO textured substrate as observed by [4], a possible cause for the loss in electrical performance are small cracks in the deposited layers.

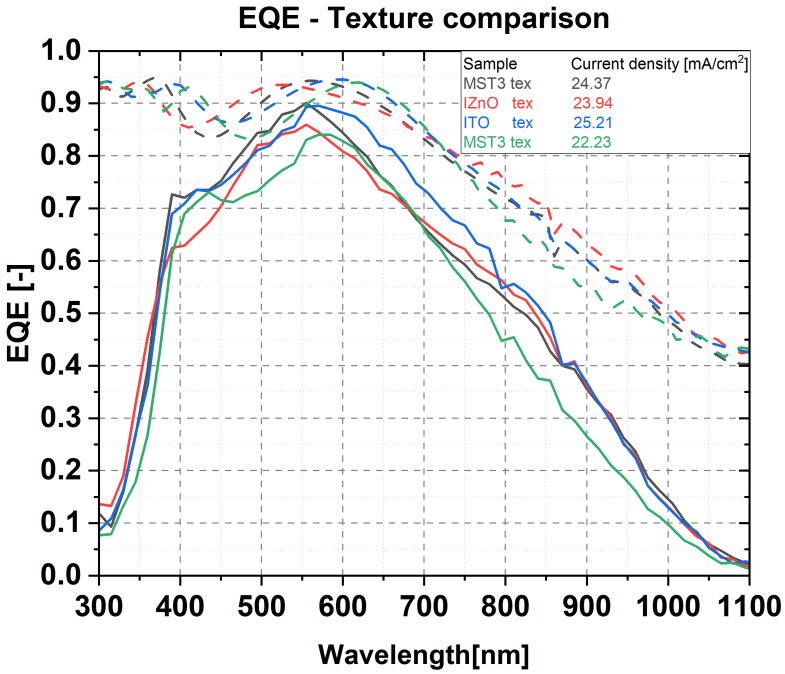

Figure 4.8: EQE measurements of the MST, i-ZnO and ITO textures from experiment 3.

Since the extra processed MST3 sample performed significantly worse than the sample processed in the initial batch, it was excluded from the reverse bias measurement shown in 4.9. The rear bias measurements were performed under a rear bias voltage of -2V to increase the potential difference between the p-doped front side and the n-doped rear side of the solar cells to extract as many charge carriers as possible. Reverse bias measurements can show the total amount of charge carriers absorbed and are a good indication of recombination processes in the solar cells.

Substrate type	J_{sc} [mA/cm^2]	J_{sc} RB [mA/cm^2]	FF[$-$]	X[%]	η[%]
MST3	24.37	26.00	0.58	66	7.46
i-ZnO	23.94	25.52	0.58	66	7.40
ITO	25.21	25.83	0.62	57	8.46

Table 4.7: Table with an overview of the key electrical parameters obtained from 0V bias and -2V reverse bias (RB) measurements of samples from experiment 3, the X is crystallinity in % and η shows the efficiency.

As can be seen from Table 4.7 the reverse bias measurements show that a bigger increase in J_{sc} can be obtained from MST textured substrates under reverse bias than from either the i-ZnO and ITO textured substrates. The ITO textured substrated only boosted the measured J_{sc} by 0.62 mA/cm^2, whereas considerably larger increases can be found in the current density from the i-ZnO and ITO textures of 1.56mA/cm^2 and 1.63mA/cm^2 respectively. This could be explained by nano features present on both the i-ZnO and ITO textures that could cause defects in the films as shown by [4]. The reverse bias measurements show the ability of MST textured substrates to scatter light more effectively, as the highest obtained J_{sc} is measured on the MST sample. The increase in measured J_{sc} can be explained by both the presence of micro and nano texture on the MST substrate which are both effective at scattering both lower and higher wavelengths, whereas the ITO texture will only be more effective at scattering higher wavelengths. The relatively large increase in measured J_{sc} shows more recombination processes are present in solar cells deposited on MST substrates. Showing the electrical performance of solar cells degrade when deposited on MST textured substrates. The reverse bias measurements highlight the potential of MST textured substrates as higher J_{sc}'s can be obtained if both electrical and optical properties can be combined.

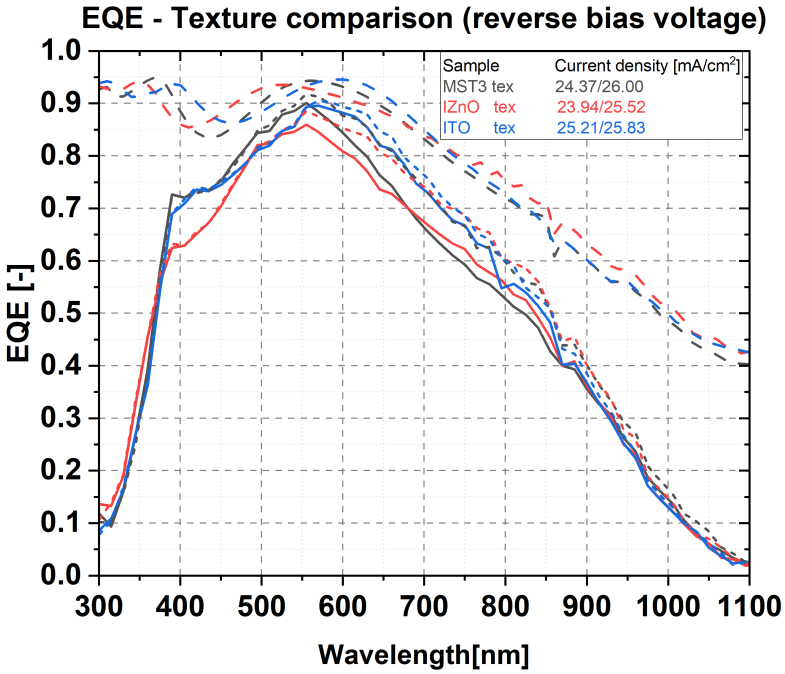

Figure 4.9: EQE measurements together with -2V reverse bias of the MST, i-ZnO and ITO textures from experiment 3.

4.3.2. Experiment 4: Shunt and front TCO configuration for a-Si:H solar cells on MST textured glass substrates

The key electrical characteristics of samples from experiment 4 are shown in Table 4.8 and show the difference obtained by performing several depositions of a-Si:H single junction solar cells on su with intrinsic-a-Si:H absorber layers of 300nm processed in an RF-PECVD chamber.

Substrate	i-ZnO[nm]	V_{oc} [V]	J_{sc} [mA/cm^2]	FF[$-$]	Efficiency[%]
MST3	3	0.862	10.59	0.67	6.12
MST3	300	0.856	11.50	0.68	6.69
MST3	600	0.857	12.13	0.68	7.07
MST3	900	0.829	12.09	0.66	6.61

Table 4.8: Table with an overview of the key electrical parameters obtained measurements of samples from experiment 4, η shows the efficiency.

Figure 4.10 show the obtained JV-curves from experiment 4, which shows an increase in obtained J_{sc} when using an i-ZnO layer when compared to the substrate with just a thin buffer layer. The cells processed on substrate A showed the biggest difference in measured current density can be found between the cells with a buffer layer and the cells with 300nm of i-ZnO as an increase of 0.91mA/cm^2 was measured. These cells were processed on half substrate which was part buffer layer and the other part had the 300nm thick i-ZnO. This was done to limit the difference in texture and thus limit the variables in the experiment. The cells on substrate B with 600nm and 900nm of i-ZnO were also processed together on the same substrate, again to minimise differences in the random texture. A slight difference of just 0.03mA/cm^2 is shown in obtained J_{sc}'s for the substrate B samples. Such a small difference can not be attributed to the difference in thickness of the i-ZnO, but rather to slight differences in substrate/layer homogeneity or measurement error. The difference in measured J_{sc} of the 300nm cell on substrate A and the 600/900nm cells from substrate B is larger with an increase of around 0.60mA/cm^2.

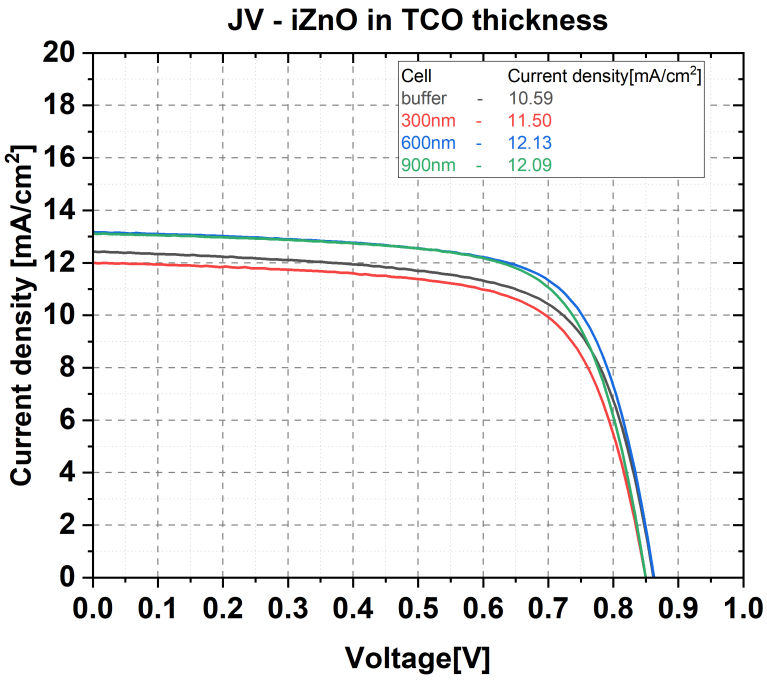

Figure 4.10: JV curves of the a-Si:H solar cells on MST textured glass substrates with different i-ZnO thickness as part of bilayer TCO from experiment 4.

The increase in J_{sc} seen in experiment 4, suggests that thick i-ZnO layers could improve scattering performance when used on MST textured glass substrates when compared to a single layer of IOH with the i-ZnO buffer layer. Measured EQE and 1-R curves, shown in 4.11, further support this as the difference between trapped light and obtained EQE is smaller when using the thicker i-ZnO. The difference in the 1-R curves does show the textures are possibly quite different even though the cells were made in pairs on single substrates. Rather large interference fringes from destructive and constructive interference between reflected and incoming light can be seen past 450nm. These large oscillations are a clear indication that light is not scattered effectively. The trend suggests that the thicker i-ZnO layers of 300-900nm are more effective at light scattering as higher current densities are obtained.

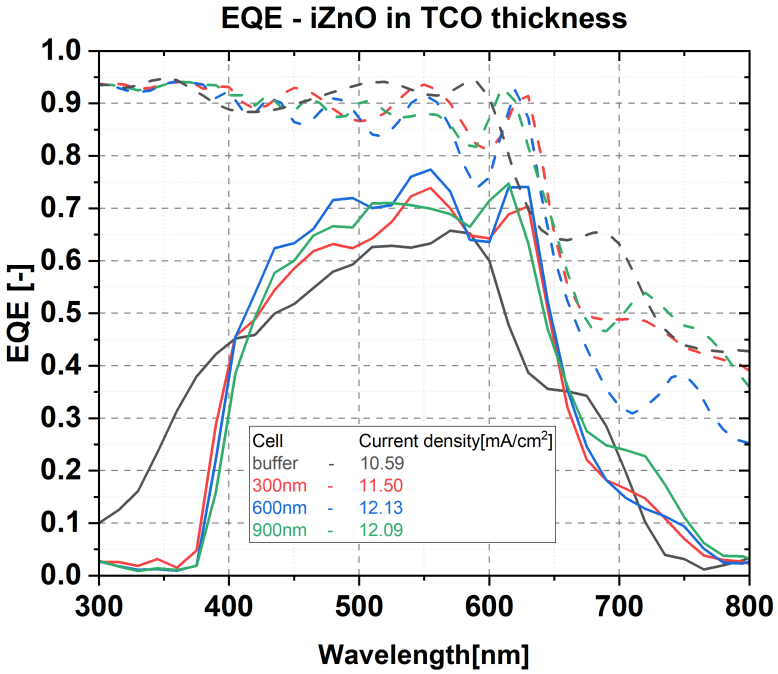

Figure 4.11: EQE measurements of the a-Si:H solar cells on MST textured glass substrates with different i-ZnO thickness as part of bilayer TCO from experiment 4.

An important difference in the obtained EQE measurements is the parasitic absorption of the i-ZnO for wavelengths below 375nm, where the bandgap of the i-ZnO is low enough to absorb all light. As seen in Figure 2.1, a relatively low photon flux is present below 375nm, however for optimal efficiencies preferably no parasitic absorption is present. The better optical scattering of the i-ZnO and the flattening of the substrate for higher quality layers for the a-Si:H solar cells do make for better solar cell performance in general.

4.3.3. Experiment 5: Thickness of i-ZnO as part of a bilayer TCO for nc-Si:H solar cells on MST textured glass substrates

The key electrical characteristics of samples from experiment 4 are shown in Table 4.8 and show the difference obtained by performing several depositions of nc-Si:H single junction solar cells with intrinsic-a-Si:H absorber layers of 2800nm processed in a VHF-PECVD chamber. From the results, a slight increase in obtained J_{sc} can be seen between the 500nm and 1000nm samples, which are processed on the same holder. A slight decrease can be observed when increasing the thickness from 1500nm to 2000nm, these samples were also processed on the same holder. Since first an increase in obtained current was measured between the 500nm thick i-ZnO layer and the 1000nm one. After which a decrease in current was observed when increasing the thickness from 1500nm to 2000nm, there seems to be an optimum thickness for the i-ZnO around 1000nm. The difference in crystallinity can not explain the differences in measured V_{oc}'s, as all samples show a crystallinity between 61 and 63%. The sample with a 500nm i-ZnO layer does have the highest V_{oc},J_{sc} and FF, suggesting that the thicker 1000-2000nm i-ZnO layers do affect the electrical performance of the solar cells. The thicker i-ZnO layers could have a flattening effect on the micro-sized features present on the substrates. This texturing is needed for the growth of nc-Si:H, which is sensitive to the slope distribution of the substrate. As the V_{oc} and FF are mostly affected, without a change in crystallinity, small cracks might again be formed due to the texture being too flat. The overall electrical performance of the 1000nm sample shows a slight decrease compared to the 500nm sample, the opposite trend can be observed for the 2000nm sample which has a higher FF and higher V_{oc} than the 1500nm sample. In general, the thicker i-ZnO layers seem to hurt the electrical performance of the solar cells and after 1000nm the scattering benefit seems to disappear. The crystallinity ratio of the samples was determined by fitting Raman

spectroscopy measurements, the fits and normalized curves can be found in Appendix D.0.2.

Substrate	i-ZnO[nm]	V_{oc} [V]	J_{sc} [mA/cm^2]	FF[$-$]	X[%]	η[%]
MST3	500	0.531	23.51	0.58	61	7.24
MST3	1000	0.514	23.97	0.55	63	6.78
MST3	1500	0.493	23.18	0.51	61	5.83
MST3	2000	0.510	22.49	0.54	63	6.19

Table 4.9: Table with an overview of the key electrical parameters obtained measurements of samples from experiment 5, the X is crystallinity in % and η shows the efficiency.

Figure 4.12 shows the JV-curves obtained from measuring the samples from experiment 5, the big differences in JV-curves might be explained by slight differences in the surface area of the back contacts. When processing the solar cells, the substrates are placed on a hard mask after which the back contacts are deposited by electron beam evaporation and thermal evaporation. During the etching process the MST surfaces are subjected to chemicals which etch away the glass, in this exothermic process, heat is released. When examining the substrates, a slight curve in the glass can be seen, which could be the reason why the size of the back contacts might vary slightly. When the substrates are on the mask and part of the glass is slightly lifted from the mask, there is the possibility that silver is deposited outside the mask area. This could create a larger back contact, thus increasing the effective area of the solar cell. When calculating the J_{sc} in mA/cm^2 with the area of the mask, a higher current will be obtained if the area of the cell is larger than expected. The EQE measurements mitigate the processing variable by only measuring an area smaller than the full surface area of the solar cell, here a more precise measurement can thus be obtained as the area measured is always the same.

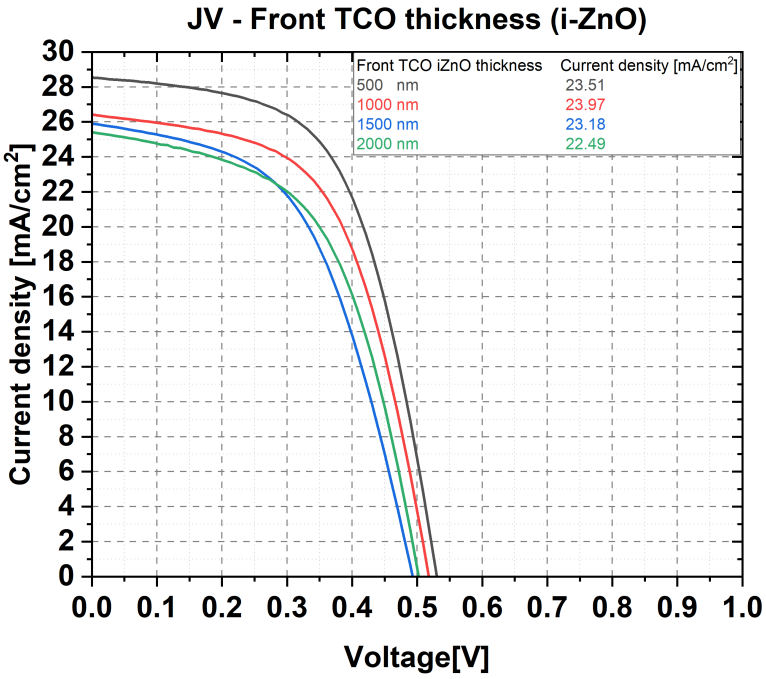

Figure 4.12: JV curves of the nc-Si:H solar cells on MST textured glass substrates with different i-ZnO thickness as part of bilayer TCO from experiment 5.

Figure 4.13 shows the optical response of the samples from experiment 5. Similar 1-R curves are shown, indicating that the substrates used are performing similarly as only small interference fringes are seen in all samples.

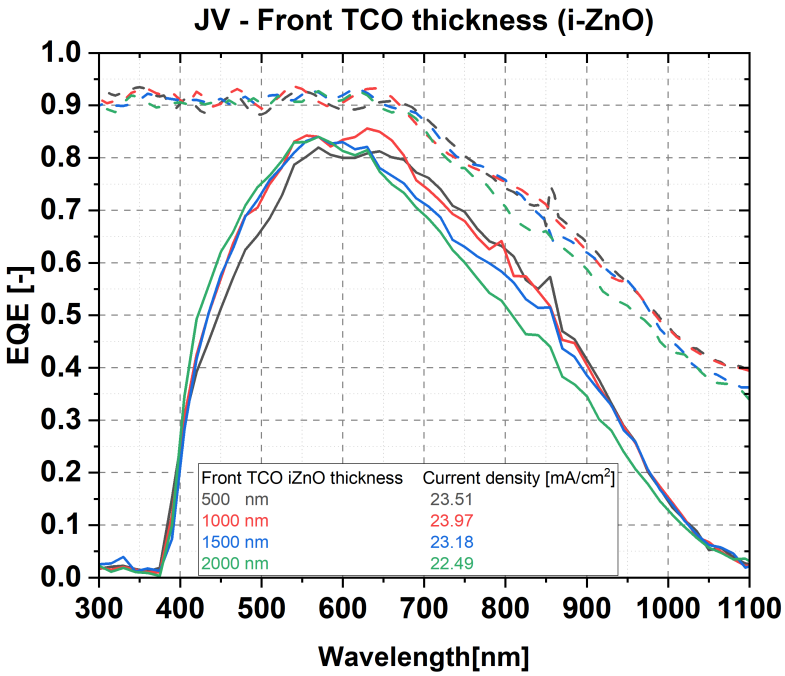

Figure 4.13: EQE measurements of the nc-Si:H solar cells on MST textured glass substrates with different i-ZnO thickness as part of bilayer TCO from experiment 5.

4.3.4. Experiment 6: Thickness variation of an i-ZnO back reflector for nc-Si:H solar cells on MST textured glass substrates

The key electrical characteristics of samples from experiment 6 are shown in Table 4.8 and show the difference obtained by performing several depositions of nc-Si:H single junction solar cells MST textured substrates with a 150nm IOH/2000nmi-ZnO bilayer with intrinsic-nc-Si:H absorber layers of 2800nm processed in a VHF-PECVD chamber. The crystallinity ratio of the samples was determined by fitting Raman spectroscopy measurements, the fits and normalized curves can be found in Appendix D.0.3.

Substrate	i-ZnO BR[nm]	V_{oc} [V]	J_{sc} [mA/cm^2]	FF[$-$]	X[%]	η[%]
MST3	60	0.537	22.14	0.62	57	8.37
MST3	240	0.535	22.95	0.63	64	8.42
MST3	500	0.536	23.52	0.63	70	8.59

Table 4.10: Table with an overview of the key electrical parameters obtained measurements of samples from experiment 6, the X is crystallinity in % and η shows the efficiency.

The significant difference in crystallinity is noteworthy, however, as the V_{oc}, J_{sc} and FF are all very close such a big difference is unexpected. If indeed the samples with thicker back reflectors are more crystalline, lower V_{oc}'s would be expected. Since this is not the case the difference could be caused by an inhomogeneity of the i-nc-Si:H layer as the fits in Appendix D.0.3 indeed show a difference in the crystallinity ratio. As can be seen from Table4.10 a slight increase in obtained J_{sc} can be seen as the thickness of the i-ZnO back reflector is increased. Since V_{oc} and FF are very similar, a slight increase in efficiency can therefore be seen in ultimate efficiency as well. Very similar JV curves were obtained from measurements and are shown in Figure 4.14, likely due to the random texture of the substrate being very similar in overall characteristics. When considering the 1-R curves from Figure 4.15 it seems indeed likely that the substrates are very similar as only minor differences can be seen. Another factor contributing to the small difference between substrates is that they are processed on the same holder, allowing for the most similar silicon deposition. Therefore it can be said that even though J_{sc}'s obtained from measurements are fairly close to each other, differences could still be attributed to the back reflector thickness.

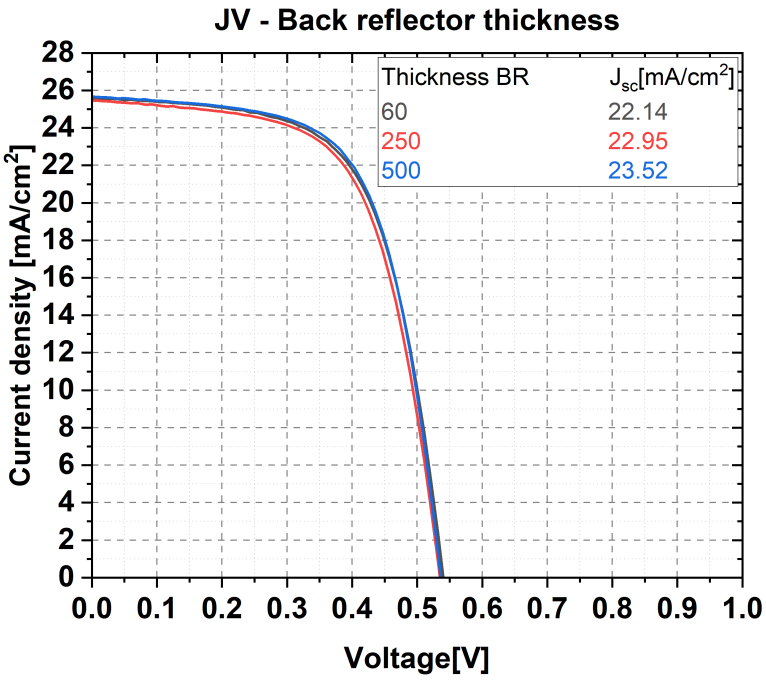

Figure 4.14: JV curves of the nc-Si:H solar cells on MST textured glass substrates with different back reflector thickness experiment 6.

Increases in the spectral response for both cells with 240nm and 500nm are shown in Figure 4.15. For the sample with the 240nm back reflector an increase in both shorter wavelengths (400-650nm) can be seen and for wavelengths larger than 800nm improvements are observed. A similar trend is visible for the sample with the 500nm back reflector between (400-650nm) as well as past 800nm. Especially an increase after 800nm is most likely due to the effect of the back reflector as mostly photons with higher wavelengths will reach the back reflector. The increase observed between (400-650nm) was not observed in simulations [52], however, a slight increase might still be caused by the back reflector from photons not absorbed whilst passing through the absorber layer for the first time. The back reflector could extent the optical path length for these photons to enable them to be absorbed.

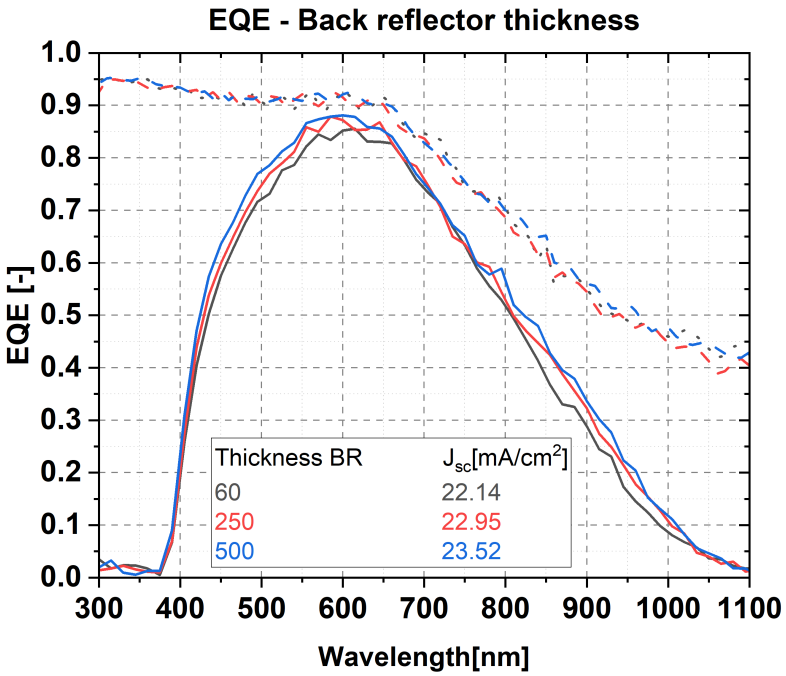

Figure 4.15: EQE measurements of the nc-Si:H solar cells on MST textured glass substrates with different back reflector thickness of experiment 6.

4.4. conclusion

In experiment 3, a difference between differently textured glass substrates is shown in obtained JV-curves, EQE measurements and EQE measurements in reverse bias. The measurements show that the ITO textured substrate performs best when measured under normal conditions, whereas the MST textured substrate performs best under reverse bias. The difference could be explained by the absence of nano-textures on the ITO texture, which could cause cracks in the deposited films, leading to a loss of current. The higher current densities obtained from reverse bias measurements under reverse bias conditions show that light scattering is more effective on MST textured substrate, their electrical performance due to higher recombination does reduce the overall performance of those types of substrate. The ITO texture, with a current density of 25.21mA/cm^2 was found to be the best performing substrate.
In experiment 4, the effect of using various thicknesses of i-ZnO as part of a bilayer TCO was shown for a-Si:H cells on MST substrates. An increase in obtained current was shown for using i-ZnO layers thicker than 300nm due to light scattering by the i-ZnO layer. A better spectral response was obtained when using a 300nm or thicker layer of i-ZnO as the i-ZnO most likely smoothens the surface on which the a-Si:H solar cell is deposited. Parasitic absorption is becoming noticeable for the thick i-ZnO layers below 375nm, the scattering effect of the i-ZnO is, however, dominant as higher current densities are obtained. Thicker i-ZnO layers as part of a bilayer TCO improve the electrical and optical performance of a-Si:H solar cells on MST textured glass substrates.
In experiment 5, the effect of using various thicknesses of i-ZnO as part of a bilayer TCO was shown for nc-Si:H cells on MST substrates. Since the nc-Si:H solar cells are a lot thicker, their electrical performance is not influenced as much as the a-Si:H cells. Only substrates with a thick (500nm) to very thick (2000nm) i-ZnO layer were used in the bilayer configuration, which showed that for similar substrates there was no trend visible for thicker bilayers. The performance differences were most likely caused by a difference in silicon depositions as shown in measured V_{oc}. A thick 1μ layer of i-ZnO as part of a bilayer TCO was found to work best for nc-Si:H cells on MST textured glass substrates.
In experiment 6, a back reflector of various thicknesses of i-ZnO was shown to improve the current density in the nc-Si:H solar cells. Improvements in both shorter (400-650nm) as well as improvements past 800nm are shown, where most likely the higher EQE in the higher wavelengths can be attributed to the back reflector as mostly larger wavelengths will reach the back reflector. An increase was not

expected in the (400-650nm) wavelength range, however, it could be explained by an increase in back-reflected photons that were not absorbed when passing through the absorber layer for the first time. Thicker i-ZnO back reflectors were found to improve the current densities of nc-Si:H solar cells deposited on MST textured glass substrates.

5

Efficiency and reproducibility improvements of a-Si:H/nc-Si:H tandem solar cells

In this Chapter, various methods that could improve the efficiency of a-Si:H/nc-Si:H tandem solar cells will be discussed. Several obstacles in the development of these tandem devices will be shown such as arguments for the use of certain textures, optical tricks to enhance light absorption of the solar cell and recommendations on how to improve the performance of a-Si:H/nc-Si:H tandem solar cells.

5.1. Literature review

Extensive experimental research and simulations have been performed on thin-film silicon multi-junction solar cells, most of which are focused on a-Si:H/nc-Si:H tandem cells. Several key performance parameters and performance enhancement techniques will be shown in this section such as a Silicon nitride anti-reflection coating, texture and TCO combinations and the functioning of the solar cells based on a n-nc-SiO_x/p-nc-SiO_x tunnel recombination junction.

5.1.1. Silicon oxide tunnel recombination junction

Comprehensive studies have been performed on different two-terminal multi-junction devices to gain insights into how silicon oxide tunnel recombination junctions function. Ideally, TRJ's function as an ohmic contact with non-rectifying behavior. When the TRJ is incorrectly designed or deposited, p-n junction behaviour can be observed, resulting in an energy barrier which significantly impacts the performance of the device. The sensitivity of the electrical performance of tandem devices to dopant concentrations in the TRJ, energy band-alignment and interface defects are shown. Furthermore, differences in amorphous and crystalline growth by the use of different substrates are shown as well as the performance dependency on the thickness of the nanolayers [55]. Note that the a-Si:H/nc-Si:H tandem solar cells are deposited in a n-i-p (substrate) configuration, which differs in deposition order from p-i-n (superstrate) configuration.

5.1.2. Texture for a-Si:H/nc-Si:H tandem solar cells

As highlighted in 4, the textured glass substrates used in the processing of nc-Si:H tandem solar cells play a vital role in light scattering and the electrical performance of the deposited devices. Tandem solar cells need effective light scattering in all wavelengths between 300-1100nm as equal currents need to be obtained from the top and bottom cells for 2 terminal devices to make them as efficient as possible. The potential of MST textured glass substrates was highlighted but did not yet outperform micro-textured glass substrates most likely due to cracks in the deposited films [4]. The potential for MST textured substrates is highlighted as being able to increase stabilized efficiencies of a-Si:H top cells by increasing their J_{sc} when using RF-sputtering to create the textured glass. On EG (micro-featured) glass textures a $V_{oc}xFF$ of 1.464x0.759V was reported to be one of the highest efficiency a-Si:H/nc-Si:H solar cells. A recommendation to go for higher aspect ratios is mentioned as a way to overcome the difficulties micro-featured glass has with scattering light in lower angles. The large feature size should enable these higher aspect ratios to be used, without causing cracks that harm the electrical performance of the solar cells.

5.1.3. Anti-reflection coating

An anti-reflection coating between the interface of glass and the TCO made of Silicon nitride is proposed to decrease light reflection by the use of refractive index grading between the glass and TCO. The

refractive index of SiN_x is reported to be tunable between 1.6 and 2.7, where values ranging from 1.7-2.0 are suitable for ARCs between glass and TCOs. Reductions in reflection of 1.6% were reported when used between glass and ZnO for an optimised SiN_x coating resulting in a 2% gain in efficiency for a thin-film silicon solar cell. The SiN_x layers were deposited using a PECVD chamber and tested with spectral ellipsometry [56]. Prior research at TU delft showed a refractive index of around 1.7 as is shown in the Figure C.1 in the black dotted line. For a ratio of 0.1:50 (SiH_4/N_2), as shown in the green line, a refractive index close to the optimal refractive index can be achieved when IOH is used as TCO. This refractive index grading will reduce the reflection as can be calculated from the Fresnel equation shown in Equation 5.1.

$$R = \left| \frac{n_1 - n_2}{n_1 + n_2} \right|^2 \tag{5.1}$$

The refractive index grading is schematically shown in Figure 5.1, where the refractive index of glass (n=1.5), SiN_x (n=1.7) and IOH (n=1.9) are shown. Reflection should be minimized, as then more light will reach the absorber layers of the solar cells which can excite more electrons to increase current densities.

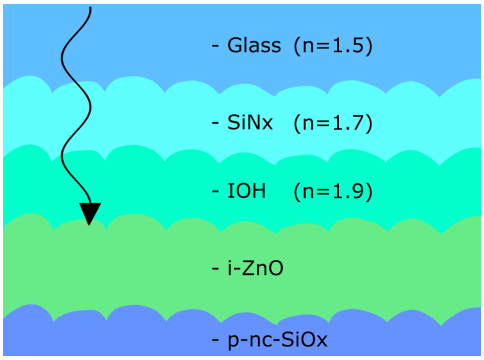

Figure 5.1: A schematic cross-section of the refractive index grading of a glass, SiN_x and IOH stack.

5.2. Experiments

In this section, the experimental setup of experiment 7, in which the thickness of the p-layer in the TRJ is varied will be presented. A comparison between MST textured glass and Asahi substrates is made for different thicknesses of the front p-layer in experiment 8, the experimental setup will be presented. Finally, the experimental setup of experiment 9 will be discussed, where a single layer TCO is compared to a bilayer and a SiN_x ARC is used on both TCO configurations.

Pressure [$mbar$]	RF Power [W]	Ar flow [$Sccm$]	Heater temperature [$C°$]
2.6	200	20	200

Table 5.1: Table with an overview of the processing conditions of the i-ZnO layer used in Chapter 3.

5.2.1. Experiment 7: p-SiO_x thickness in the Tunnel Recombination Junction of a-Si:H/nc-Si:H solar cells on MST textured glass substrates

In experiment 7, initially, a comparison attempt was made between different thicknesses of the second p-doped layer in the tunnel recombination junction. All MST substrates use a 150nm IOH layer that functions as the front electrode. Three MST textured substrates were deposited using both RF- and VHF-PECVD chambers with a p-i-n structure made of p-nc-SiO_x/i-a-Si/n-nc-SiO_x for the top cell and p-nc-SiO_x/i-nc-Si/n-nc-SiO_x for the bottom cell. The i-a-Si:H absorber layers have a thickness of 300nm and the i-nc-Si:H absorber layers have a thickness of 2800nm. To determine the performance of the MST substrates only an i-ZnO buffer layer was used between the IOH and the p-nc-SiO_x. A 60nm i-ZnO back reflector is used, deposition conditions can be found in Table 5.1. The full list of deposition conditions for this experiment can be found in Appendix B.7. The aim was to improve the yield of working solar cells that show good JV characteristics, therefore the thickness of the p+ layer in the TRJ

was adopted. The thickness of the p-layers in the TRJ can significantly impact the obtained V_{oc}, EQE and thus J_{sc} and Fill Factor. The processing parameters for the i-a-Si:H and i-nc-Si:H absorber layers are shown in Table 5.2 and Table 5.3. A schematic cross-section of the solar cell design is shown in Figure 5.2.

Pressure [$mbar$]	RF Power [W]	SiH4 flow [$Sccm$]	H2 flow [$Sccm$]	Substrate
0.7	2.8	40	0	MST

Table 5.2: Table with an overview of the processing conditions of the i-a-Si:H absorber layer used in experiment 7.

Pressure [$mbar$]	VHF Power [W]	SiH4 flow [$Sccm$]	H2 flow [$Sccm$]	SC [%]	Substrate
4	40	3.2	120	2.6	MST

Table 5.3: Table with an overview of the processing conditions of the i-nc-Si:H absorber layer used in experiment 7.

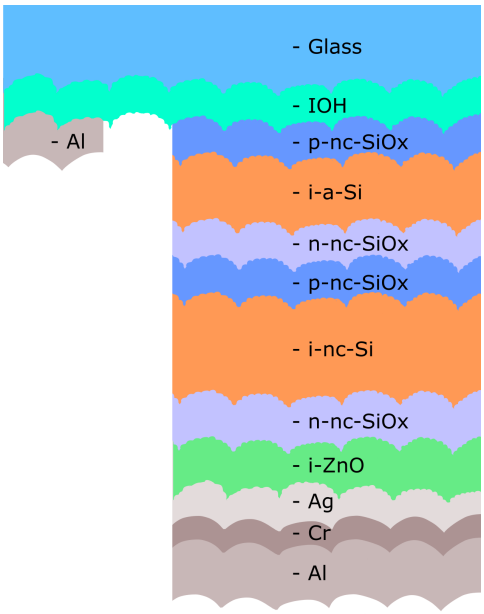

Figure 5.2: A schematic cross-section of the a-Si:H/n-Si:H solar cell used in experiment 7.

5.2.2. Experiment 8: Front p-SiO_x thickness MST vs Asahi comparison

In experiment 8, a comparison is made between various front p-layer thicknesses as a possible cause for the inconsistent JV measurement. The influence of the glass texture on the deposition thickness will be largest at the first deposited p-layer, hence it was chosen to change the thickness of this layer to examine if this was the cause for the fluctuating electrical performance of the solar cells. Here, it is chosen to use MST substrates with a thick 1000nm i-ZnO layer together with a 150nm IOH layer. Deposition times of the p-layer are multiplied as noted by 1x,1.5x and 2. The 1x deposition time should give 5nm, 12nm and 3nm for the p+,p and i-SiO_x layers respectively. The deposition conditions for the i-ZnO as part of the bilayer TCO are shown in Table 5.1. A schematic cross-section of the solar cell design used is shown in Figure 5.3. The reasoning is that texturing will have an influence on layer thickness as the effective surface area of the glass substrates increases by texturing. This has the most influence on the deposition rate of the p-layer as this is the first silicon layer in the solar cell stack. Another factor is that the deposited p-layers are only tens of nanometres thick and features of the glass texture can be of the same order of magnitude. By using a thick i-ZnO layer, the effect of the nano-features of the glass should be mitigated. Calculating actual deposition rates of doped nc-SiO_x layers is possible, but only for depositions on flat glass, which is a requirement for optical characterisation methods such as spectral ellipsometry. Actual deposition thicknesses can therefore only be extrapolated, adding to the complexity of processing devices on randomly textured glass. Asahi substrates were added to each of

the three holders as reference substrates as these have proven to be more reliable, albeit at the cost of less scattering at larger wavelengths. The i-a-Si:H absorber layers have a thickness of 300nm and the i-nc-Si:H absorber layers have a thickness of 2800nm. The processing parameters for the i-a-Si:H and i-nc-Si:H absorber layers are shown in Table 5.4 and Table 5.5. The full list of deposition conditions for this experiment can be found in Appendix B.8.

Pressure [$mbar$]	RF Power [W]	SiH4 flow [$Sccm$]	H2 flow [$Sccm$]	Substrate
0.7	2.8	40	0	MST

Table 5.4: Table with an overview of the processing conditions of the i-a-Si:H absorber layer used in experiment 8.

Pressure [$mbar$]	VHF Power [W]	SiH4 flow [$Sccm$]	H2 flow [$Sccm$]	SC [%]	Substrate
4	40	3	140	2.1	MST /Asahi

Table 5.5: Table with an overview of the processing conditions of the i-nc-Si:H absorber layer used in experiment 8.

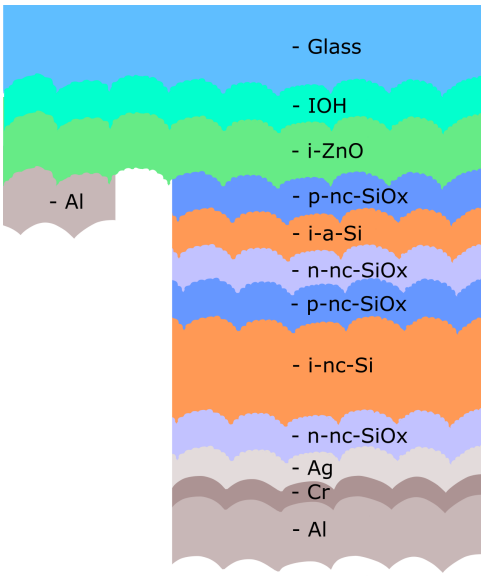

Figure 5.3: A schematic cross-section of the a-Si:H/nc-Si:H solar cell used in experiment 8, note that the same design was applied on the Asahi substrates.

5.2.3. Experiment 9: Anti-reflection coating and bilayer comparison of a-Si:H/nc-Si:H solar cell comparison on ITO textured glass substrates

In experiment 9, a comparison is made between a-Si:H/nc-Si:H solar cells deposited on ITO textured glass with differences in the thickness of i-ZnO as part of a bilayer TCO. Another part of the experiment was the addition of an optimised SiN_x anti-reflection coating based on n and k data obtained from spectral ellipsometry. The anti-reflection coating was developed by Leo Adachi, who researched the optimal parameters and corresponding processing conditions of the SiN_x at TU Delft. This experiment aimed to show progress made in the development of the a-Si:H/nc-Si:H solar cells researched at TU Delft. The ITO texture was chosen as it showed the overall best combination of optical and electrical performance for substrates currently produced at TU Delft. Another aim of this experiment was to integrate the anti-reflection coating and evaluate the performance of the a-Si:H/nc-Si:H solar cells. After the best-performing substrate, with the highest overall current density was obtained, further current matching should highlight the best efficiencies that can be achieved with the recipe under development. Four ITO textured substrates were used for this experiment, on which the SiN_x ARC was applied to two of them. The SiN_x has a thickness of 80nm and a refractive index of n=1.7 at 600nm, the entire refractive index curve is shown in Appendix C.1. During processing, two out of these four initial substrates were lost, therefore ITO textured glass from a different processing batch had to be used due to time

limitations. ITO textured substrates with 150nm IOH in combination with a thin buffer layer of i-ZnO or a 1μ thick layer were used as front TCO, deposited using the conditions shown in Table 5.1. The i-a-Si:H absorber layers have a thickness of 300nm and the i-nc-Si:H absorber layers have a thickness of 2800nm. A 60nm back reflector was added using the same deposition conditions from 5.1. The processing parameters for the i-a-Si:H and i-nc-Si:H absorber layers are shown in Table 5.6 and Table 5.7. The full list of deposition conditions for this experiment can be found in Appendix B.9. A schematic cross-section of the solar cell design used is shown in 5.4.

Pressure [$mbar$]	RF Power [W]	SiH4 flow [$Sccm$]	H2 flow [$Sccm$]	Substrate
0.7	2.8	40	0	MST

Table 5.6: Table with an overview of the processing conditions of the i-a-Si:H absorber layer used in experiment 9.

Pressure [$mbar$]	VHF Power [W]	SiH4 flow [$Sccm$]	H2 flow [$Sccm$]	SC [%]	Substrate
4	40	3	133	2.2	ITO

Table 5.7: Table with an overview of the processing conditions of the i-nc-Si:H absorber layer used in experiment 9.

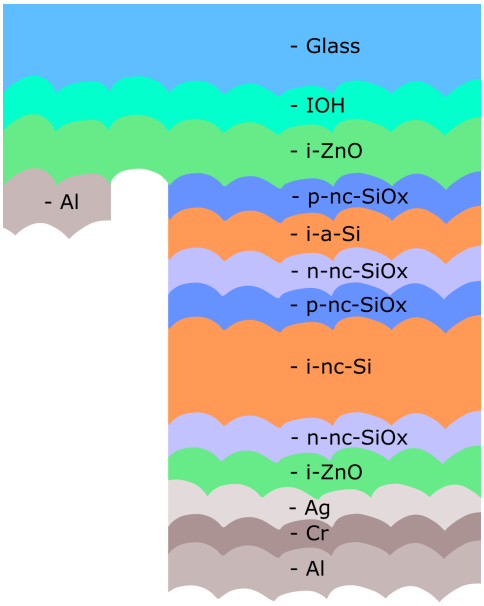

Figure 5.4: A schematic cross-section of the a-Si:H/nc-Si:H solar cell design used in experiment 9, note the SiN_x is not shown between the glass and IOH interface as not all samples have the anti-reflection coating.

5.3. Results and discussion

In this section, the results of the thickness variation of the p-layer in the TRJ of experiment 7 will be presented and discussed. The outcome of experiment 8 will be presented and a reasoning for the results will be given. Finally, experiment 9, which compares the bilayer to a single layer and the use of a SiN_x ARC are presented with a discussion on the obtained results.

5.3.1. Experiment 7: p-SiO_x thickness in the Tunnel Recombination Junction of a-Si:H/nc-Si:H solar cells on MST textured glass substrates

The key electrical characteristics of samples from experiment 7 are shown in Table 5.8, the differences seen here in the electrical performance of the a-Si:H/nc-Si:H solar cells are very significant. These differences can not be explained by the difference in thickness of the p-layer alone. The crystallinity ratio of the samples was determined by fitting Raman spectroscopy measurements, the fits and normalized curves can be found in Appendix D.0.4.

Substrate	V_{oc} [V]	J_{sc} Bot[mA/cm^2]	J_{sc} Top[mA/cm^2]	FF[$-$]	X[%]	η[%]
MST3	1.28	7.84	11.00	0.42	65	4.20
MST3	1.36	10.03	11.27	0.65	64	8.9
MST3	1.36	9.17	11.87	0.47	63	5.9

Table 5.8: Table with an overview of the key electrical parameters obtained measurements of samples from experiment 7, the X is crystallinity in % and η shows the efficiency.

In Figure 5.5 the JV-curves of the samples processed in experiment 7 are shown, they show the rather large difference also shown in Table 5.8. At first, an optimum value for the thickness of the p-window layers seems to be achieved, as the cell with an 18nm p-window layer has the highest fill factor of 0.65. A closer look at the obtained EQE measurements, as shown in Figure 5.8, suggest that other variables are at play.

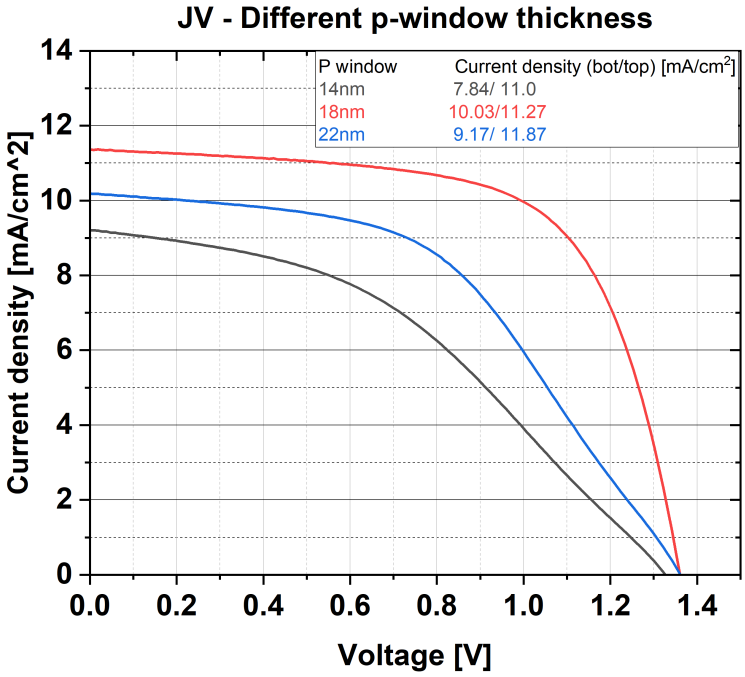

Figure 5.5: JV curves of the a-Si:H/nc-Si:H solar cells with p-window (TRJ) thickness variations of experiment 7.

In Figure 5.8 the EQE measurements of the cells are shown, especially the combination of the obtained 1-R curves (dashed lines) and the EQE of the corresponding solar cell are interesting. The obtained 1-R curves show the presence of rather large fringes coming from constructive and destructive interference of waves in the solar cell. These fringes show the texture is not scattering effectively, which can in turn be seen in the EQE's of all samples. Whenever there is a dip or a peak in the 1-R curve, there is also a dip or a peak in the EQE of the corresponding cell. The obtained EQE measurements therefore are limited in certain areas of the solar spectrum, which for these samples is especially noticeable in the spectral response of the bottom cells. The 22nm sample, for example, is significantly limited between 650nm and 800nm as a large dip in the EQE is shown. Such large dips will in turn limit the obtained current density from that cell, significantly decreasing the efficiency of the cell. Similar results are shown for the other top and bottom cells of all samples.

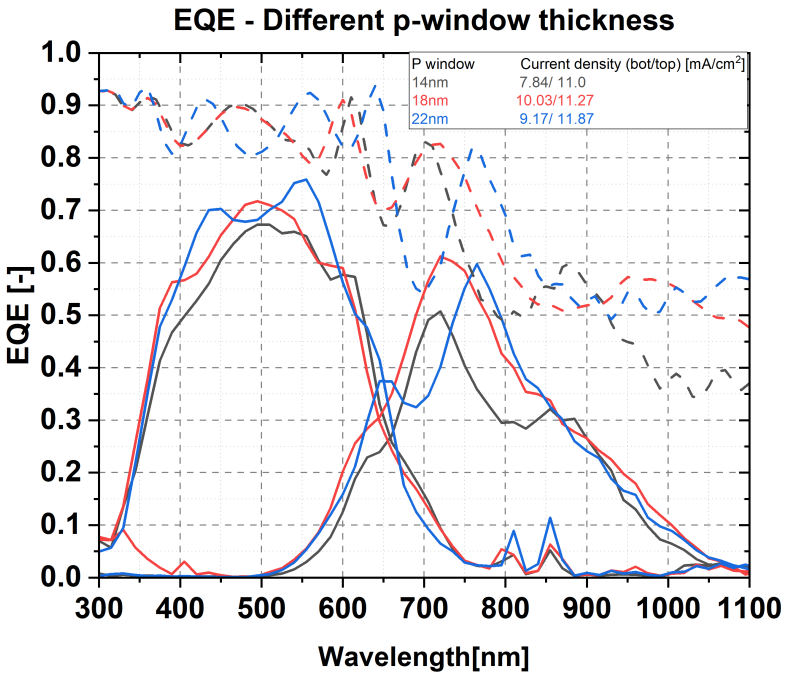

Figure 5.6: EQE measurements of the a-Si:H/nc-Si:H solar cells with p-window (TRJ) thickness variations of experiment 7

The spectral response and texturing might explain the difference in obtained J_{sc}, however, a big difference in electrical performance is also shown in Figure 5.5. The performance of tunnelling junctions is especially dependent on the thickness of the deposited p-layers as shown in literature [55]. The inhomogeneity of the texture can result in inhomogeneous layer deposition, which can reduce the efficiency of the tunnelling junction. To decrease the impact of the texture on the performance of the solar cells a thick i-ZnO layer could be used to flatten out the texture.

5.3.2. Experiment 8: Front p-SiO_x thickness MST vs Asahi comparison

The key electrical characteristics of samples from experiment 8 are shown in Table 5.9, for comparison, a reference cell deposited on an Asahi substrate was processed alone on a holder. In particular, the optical performance of the cells deposited on these substrates will be analysed, as the electrical performance of the solar cells is significantly worse when compared to the reference cell. Some noticeable differences can however be obtained from the EQE measurements performed, as in all cells a clear trend can be observed below 500nm. Here, the spectral response is significantly decreasing as the thickness of the p-layers increases. This can be explained by p-layers starting to act more as absorber layers as they become thicker, thus allowing for more absorption in the 300-500nm wavelength range. Since the p-layers are doped, most light absorbed here will be lost due to recombination processes thus reducing the spectral response of the solar cell in the lower wavelengths. The crystallinity ratio of the samples was determined by fitting raman spectroscopy measurements, the fits and normalized curves can be found in Appendix D.0.5.

Substrate	V_{oc} $[V]$	J_{sc} Bot$[mA/cm^2]$	J_{sc} Top$[mA/cm^2]$	FF$[-]$	X[%]	η[%]
Asahi A	1.283	9.34	13.77	0.61	69	7.31
MST3 A	1.288	10.70	10.93	0.56	79	7.71
Asahi B	1.330	6.69	13.16	0.48	66	4.27
MST3 B	1.299	10.13	10.31	0.45	74	5.92
Asahi C	1.266	10.25	12.35	0.55	76	7.14
MST3 C	1.288	11.23	9.95	0.48	77	6.15
Asahi Ref	1.261	10.65	13.05	0.66	75	8.86

Table 5.9: Table with an overview of the key electrical parameters obtained measurements of samples from experiment 8, the X is crystallinity in % and η shows the efficiency.

The performance difference between the samples processed on Asahi substrates and the reference cell, which also uses an Asahi substrate, is significant. An explanation for this is most likely the difference in thickness of the Asahi substrate when compared to the thickness of MST textured glass substrates. In the deposition chamber, the plasma will behave slightly differently when a gap is present between the substrate and the holder, which acts as the rear electrode in the PECVD chamber. An image showing the difference in colouration of the front side of MST substrates can be found in Appendix E.1.

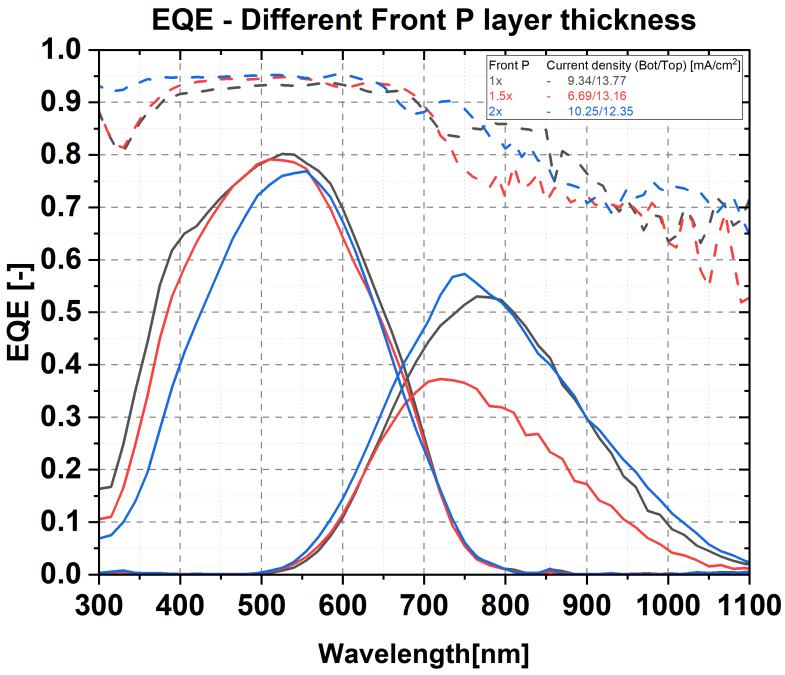

Figure 5.7: EQE measurements of the Asahi substrates with varying front p-layer thickness.

Figure 5.8 shows the 1-R curves obtained from the samples processed on Asahi substrates, these are significantly smoother and overall higher in absolute value. This shows that even though a $1000nm$ i-ZnO layer was added, the scattering on the MST substrates is overall worse than the Asahi substrates. Interestingly, the 1-R curves are also lower in the higher wavelengths, where the MST texture should outperform the Asahi substrate. This is another indication the MST substrate as processed, does not provide enough consistency. Earlier experiments have shown good 1-R curves were obtainable from the MST substrates, as is shown in Figure 4.15. These differences are likely the cause of the double texturing steps required to make MST textured substrates, where twice sacrificial layers need to be deposited and etched to obtain the double texture. Deposition of both layers happens via RF-sputtering, which is a less consistent process than the LPCVD used by [4].

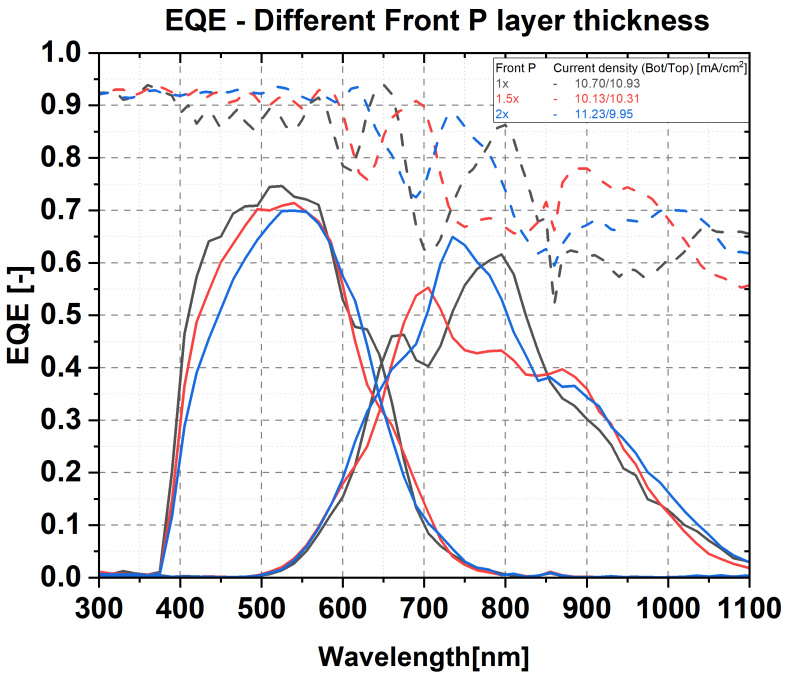

Figure 5.8: EQE measurements of the MST substrates with varying front p-layer thickness.

The Reference cell processed in the same run as the samples from experiment 8 are shown in Figure 5.9. The reference cell shows decent performance and is top cell limited, as is to be expected from an Asahi substrate with no optical enhancements such as scattering TCO layers, anti-reflective coating or thick back reflectors.

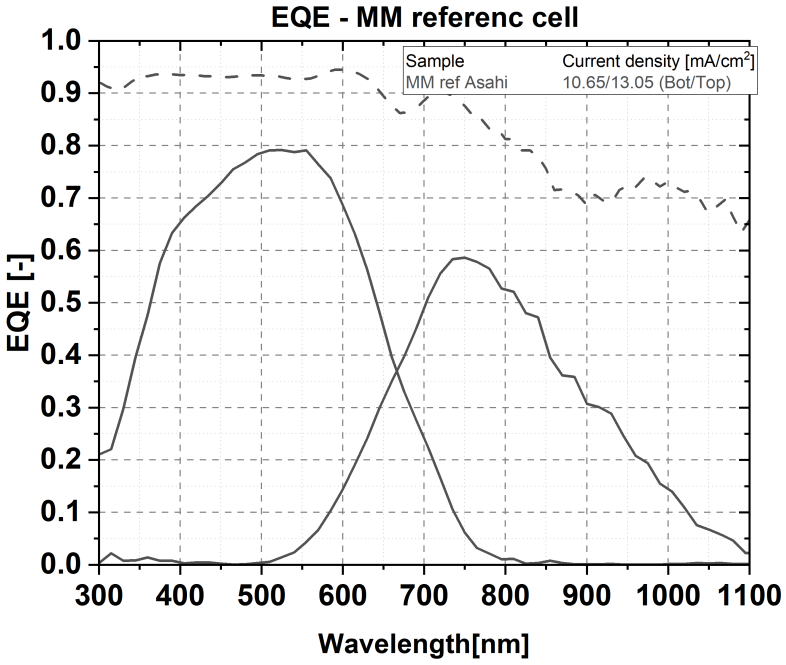

Figure 5.9: EQE measurements of the reference cell on an Asahi substrate from the same run.

5.3.3. Experiment 9: Anti-reflection coating and bilayer comparison of a-Si:H/nc-Si:H solar cell comparison on ITO textured glass substrates

The electrical characteristics of the samples from experiment 9 show a significant energy barrier, as can be seen in Figure 5.10. The optical response from these samples was however measurable, so the focus will be the functioning of the anti-reflection coating and the use of an i-ZnO bilayer TCO on ITO textured samples. The crystallinity ratio of the samples was determined by fitting Raman spectroscopy measurements, the fits and normalized curves can be found in Appendix D.0.6.

Substrate	V_{oc} $[V]$	J_{sc} Bot$[mA/cm^2]$	J_{sc} Top$[mA/cm^2]$	FF$[-]$	X[%]	η[%]
Bilayer	1.223	11.76	12.23	0.38	71	7.31
Bilayer + ARC	1.217	10.36	10.63	0.47	74	7.71
Buffer	1.305	11.57	12.77	0.24	81	4.27
Buffer + ARC	1.294	10.03	11.36	0.21	69	5.92
Asahi Reference cell	1.310	10.03	14.65	0.70	79	9.35

Table 5.10: Table with an overview of the key electrical parameters obtained measurements of samples from experiment 9, the X is crystallinity in % and η shows the efficiency.

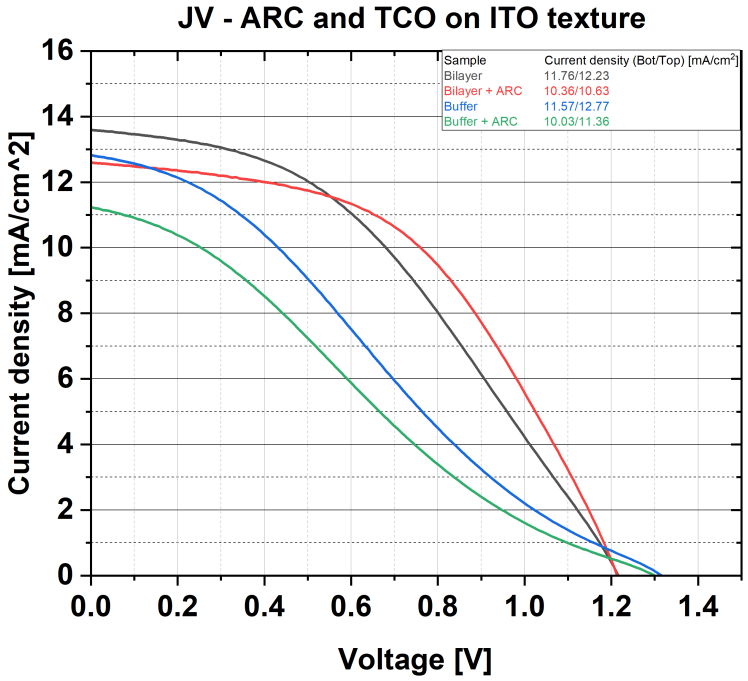

Figure 5.10: JV curves of the a-Si:H/nc-Si:H solar cells from experiment 9.

The optical properties of the samples from experiment 9 were measured both with Reflectance and EQE(spectral response) measurements, reverse bias measurements were also performed at -2V reverse bias. All obtained J_{sc} values were obtained by applying either a $0.35V$ (top cell) or $0.65V$ (bottom cell) forward bias on the solar cells to measure actual short circuit current conditions as is explained in Section 2.7.2. In Figure 5.11 the obtained spectral response of the ITO textured substrate with a $1000nm$ i-ZnO layer is shown. A total current density of 23.99 mA/cm^2 was obtained from integrating the EQE curve, for the reverse bias measurements a total current density of 25.30 mA/cm^2 was obtained, an increase of around 5.5%. Increases over the entire wavelength range are shown in the reverse bias measurements, for both top and bottom cells. A decent 1-R curve (dashed line) is also shown, with some interference fringes between 600-800nm. The 1-R curve shows that a lot of light is absorbed in the 300-700nm wavelength range, however, for larger wavelengths a steep drop is shown. Suggesting light scattering is still not happening effectively enough at the larger wavelengths.

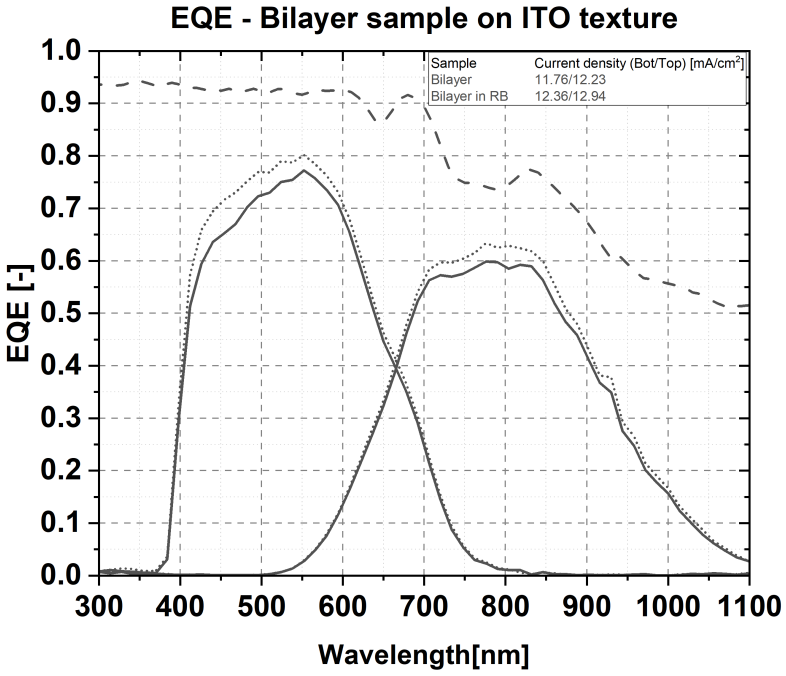

Figure 5.11: EQE measurements of the a-Si:H/nc-Si:H solar cell on an ITO textured glass substrate with a bilayer TCO.

In Figure 5.12 the obtained spectral response of the ITO textured substrate with anti-reflective coating and a 1000nm i-ZnO layer is shown. This sample was processed on the same holder as the bilayer on ITO texture sample, shown in 5.11, so very similar silicon layers should be present. A lower total current density is measured of 20.99 mA/cm^2, significantly lower than for the sample without the ARC. As expected a 1-R curve with higher overall values was measured, with even smaller interference fringes than for the sample without the ARC. This means that a large fraction of the incoming light is lost between the silicon solar cell layer and the glass at the front of the device. The reason for this could either be that the SiN_x got partially destroyed during the deposition of the IOH on top of the SiN_x, a porous SiN_x layer was deposited to achieve the desired refractive index of 1.7 as shown in (ref to appendix). Depositions of IOH on top of the SiN_x ARC were performed, as well as annealing steps. The SiN_xtested was processed under different conditions and had a higher refractive index, indicating it is a less porous material. Another option could be that the IOH deposition is very thick, when TCO's are deposited thicker than desired they can start absorbing light. Initially, all TCO layers of the four samples were processed in a single holder in the Zorro (RF-sputtering) tool, however, due to time constraints it was chosen not to produce all four substrates again after the loss of two substrates. Therefore, differences in the IOH thickness might play a role in the parasitic absorption observed. The difference in texture might also be partially at play for the difference in solar cell performance, however, as the 1-R curve shows smaller interference fringes than the sample without the ARC this is likely not a significant contribution. Interestingly, the reverse bias measurements only increase the total obtained current density from 20.99mA/cm^2 to 21.66mA/cm^2, which is a 3.2% increase. Especially the bottom cell showed a little extra gain in current density, suggesting most charge carriers are actually collected and thus a lot of parasitic absorption is indeed taking place.

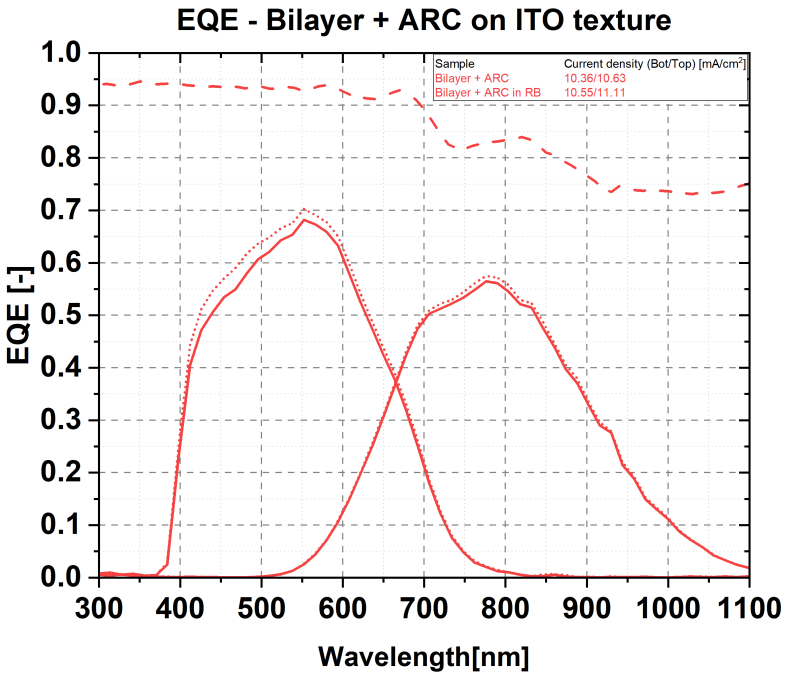

Figure 5.12: EQE measurements of the a-Si:H/nc-Si:H solar cell on an ITO textured glass substrate with a bilayer TCO and the SiN_x ARC.

In Figure 5.13 the obtained spectral response from the ITO textured substrate with only 150nm of IOH and a thin buffer layer of i-ZnO is shown. Here it is shown that without the i-ZnO more interference fringes are present in the 1-R curve, which is also directly noticeable in the EQE curves. A total current density of 24.34 mA/cm^2 was obtained from the EQE measurement, which surpasses the 23.99mA/cm^2 of the sample with the IOH/i-ZnO bilayer. However, due to the presence of large interference fringes the full potential of this substrate type will be lower. The optical performance of the bottom cell is already more limited as is visible by the large fringe at 700-800nm. Furthermore, the current limiting cell, in this case, the bottom cell, has a lower current at 11.57mA/cm^2 than the cell with the bilayer configuration at 11.76mA/cm^2. The reverse bias measurements show an increase from 24.34mA/cm^2 to 25.08mA/cm^2 which is a gain of 3.0%. Again, only a marginal increase can be seen in the current density gains of the bottom cell. Interestingly, the reverse bias measurement value of 25.08mA/cm^2 is lower than the sample with the bilayer TCO, which achieved a total current density of 25.30mA/cm^2 in reverse bias.

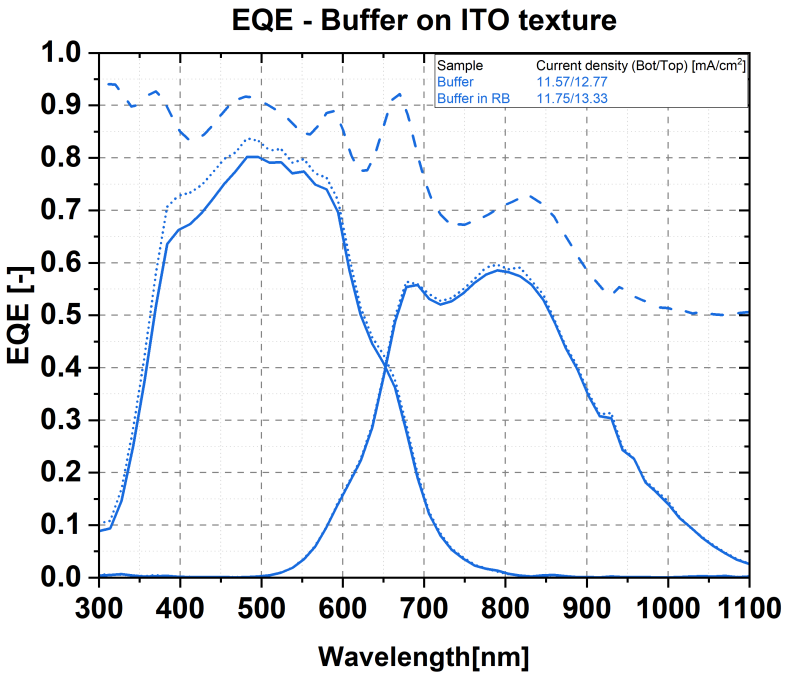

Figure 5.13: EQE measurements of the a-Si:H/nc-Si:H solar cell on an ITO textured glass substrate with a monolayer IOH TCO.

In Figure 5.14 the obtained spectral response from the ITO textured substrate with the SiN_x ARC, a 150nm IOH layer and a thin i-ZnO buffer layer is shown. Here, also large interference fringes are present, which are also noticeable in the obtained EQE measurement. A total current density of 21.39mA/cm^2 is obtained and a total current density of 22.13mA/cm^2 for the reverse bias measurement which is a gain of 3.5%. Just as for the sample with the bilayer and the SiN_x ARC, only a slight gain in current density was achieved for the reverse bias measurement. Again, this suggests that a lot of parasitic absorption takes place between the glass and the silicon layers, the same explanation as given for the bilayer sample is likely here.

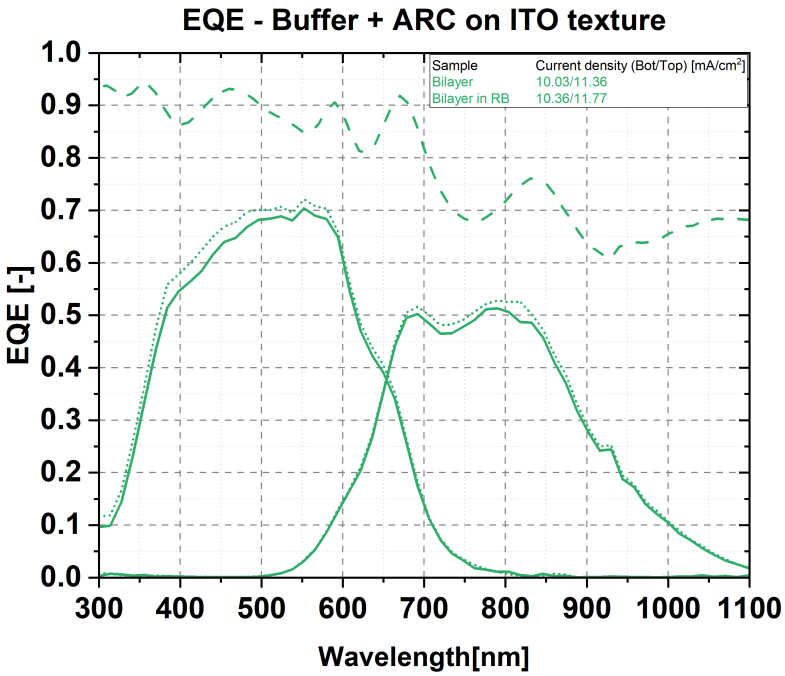

Figure 5.14: EQE measurements of the a-Si:H/nc-Si:H solar cell on an ITO textured glass substrate with a monolayer IOH TCO and the SiN_x ARC.

A comparison between the ITO textured substrates and the reference tandem cell, processed on an Asahi substrate is shown in Figure5.15. It is shown that the reference cell has similar 1-R values for between 400-700nm as the bilayer samples on ITO texture, interestingly, for higher wavelengths the Asahi substrate still performs better than the bilayer sample. This is surprising as the texture of the asahi substrates is designed to scatter light at shorter wavelengths, whereas the ITO texture should help with scattering in longer wavelengths. The only sample that had better absorption was the bilayer sample with the SiN_x ARC. However, as parasitic absorption likely plays a significant role in the higher obtained 1-R curve it can not be said with certainty this substrate will outperform the reference cell for light trapping. The sample with the bilayer and ARC does show potential to be the best substrate as it shows the absolute highest 1-R curve with the smallest interference fringes, however, more research into the cause of the parasitic absorption needs to be done to draw a decisive conclusion. Both bilayer samples show significant improvements in the 1-R curves as the interference fringes are substantially reduced between 300-700nm.

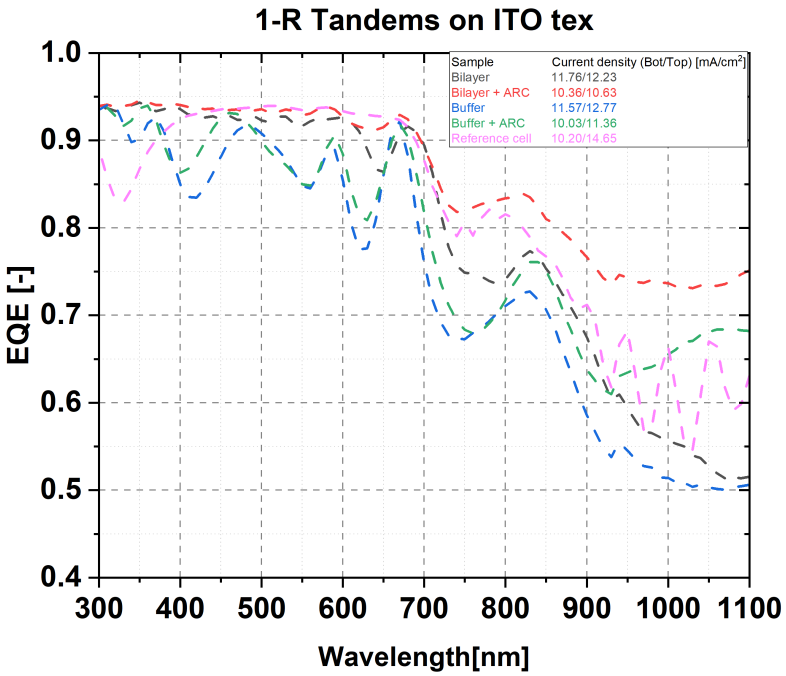

Figure 5.15: The 1-R curves of the a-Si:H/nc-Si:H solar cells on ITO textured glass, with monolayer, bilayer and with and without the SiN_x ARC. The 1-R of the Asahi reference cell is also shown as a comparison.

5.4. conclusion

In experiment 7, the sensitivity of the tunnel-recombination junction was shown for MST textured glass substrates on which a-Si:H/nc-Si:H solar cells were deposited. The slight difference in thickness of the p-layer is likely not enough to cause the large difference in fill factor for these samples. Large differences in the 1-R curves show a large variation in the light scattering by the textured glass, indicating that indeed the texture is likely too inhomogeneous.

In experiment 8, front p-layer thickness was investigated for MST textured substrates alongside Asahi substrates for reference. With EQE measurements it was shown that the front p-layer should not be increased in thickness, as more parasitic absorption is facilitated by doing so. Lower values in EQE measurements between 300-500nm were shown for the top cells of all substrates. The 1μ i-ZnO layer added to the substrate on top of the 105nm of IOH, to help with scattering, did not manage to get rid of the interference fringes.

In experiment 9, a comparison was made between different TCO combinations (1μ i-ZnO versus only a buffer layer) and the addition of a SiN_x anti-reflection coating. Better light absorption was achieved by adding the SiN_x layer, although lower EQEs were measured. Parasitic absorption in either the SiN_x or TCO is therefore most likely, as during deposition Nitrogen atoms might have been released into the TCO. Another possibility is that the IOH depositions were thicker than expected. A reference sample was shown to prove the recipe that was used can deliver working devices. The Asahi substrates have a premade TCO, therefore, these substrates are more reliable. Both samples with and without the SiN_x show poor JV characteristics and in experiment 7 it was shown that the recipe is transferable between Asahi and MST substrates. This suggests that most likely the IOH depositions are the reason for the poor JV characteristics of the cells. The highest overall current was obtained by the sample with only IOH as TCO without the SiN_x ARC of 24.34mA/cm^2. Optimal performance was achieved by the bilayer sample without the SiN_x ARC, as the 1-R curve has the smallest fringes. Most potential can be found in the bilayer sample with the SiN_x ARC, however, as there is a lot of parasitic absorption these issues will have to be addressed first.

5.5. recommendations

Good electrical properties of a-Si:H/nc-Si:H are vital if high efficiencies are to be obtained. My first recommendation would be to produce the in-house manufactured glass substrates at least several weeks before processing them in the PECVD cluster tool. As shown in experiment 9, the loss of substrates due to errors can make finding trends in the results rather difficult. Good quality control of the TCO layers deposited on these substrates could improve the reliability of the cells processed on them.

The SiN_x ARC seems to have a good influence on reducing the reflection and increasing the light trapped in the device. As experiment 9 showed, a good 1-R curve can be obtained for ITO textured glass in combination with this ARC. An experiment on the SiN_x with the 0.1:50 ratio where an IOH layer is deposited on top should be repeated to investigate the electrical properties. If a good working substrate is obtained, the experiment can be repeated to find out if and to what extent the SiN_x is working.

A high-energy bandgap top cell could be implemented on the tandem devices. As the demonstrated high-bandgap amorphous silicon processed in a VHF-PECVD chamber is very sensitive, a more tested way of making high-bandgap a-Si:H top cells is recommended. On the current setup of the PECVD tool, only one VHF chamber is available, which is also used for the nc-Si:H cell. Furthermore, the condition of the PECVD chambers is to be kept as stable as possible, the use of a single PECVD chamber for both absorber layers is therefore not ideal.

An external anti-reflection coating can be added to the front side of the glass with a refractive index of around 1.3 as was also used in the record module produced by TEL Solar of 12.34%. This could enable better 1-R curves than currently obtained.

A higher bandgap material replacing the i-ZnO is recommended to reduce parasitic absorption losses, the layer should have similar scattering properties to be a suitable candidate.

References

1. Contribution of Working Groups I, I., III to the Sixth Assessment Report of the Intergovernmental Panel on Climate Change [Core Writing Team, H. L. & (eds.)], J. R. Summary for Policymakers. *Climate Change 2023: Synthesis Report,* pp. 1–34 (2023).
2. Perez, R. & Perez, M. A fundamental look at energy reserves for the planet. **50,** 3 (Jan. 2009).
3. Victoria, M. *et al.* Solar photovoltaics is ready to power a sustainable future. *Joule* **5,** 1041–1056 (2021).
4. Tan, H. Materials and Light Management for High-Efficiency Thin-Film Silicon Solar Cells. *TU Delft repository* **143,** 1–150. https://repository.tudelft.nl/islandora/object/uuid:847f7430-26d3-4034-bc9c-32f394bd9495?collection=research (2015).
5. Core Writing Team, H. L. & (eds.), J. R. Summary for Policymakers. In: Climate Change 2023: Synthesis Report. *IPCC,* 1–34 (2023).
6. IEA. CO2 Emissions in 2022. https://www.iea.org/reports/co2-emissions-in-2022 (2023).
7. https://www.seia.org/initiatives/solar-technologies#:~:text=There%20are%20three%20primary%20technologies,(SHC)%20systems%2C%20which%20collect.
8. Tiedje, T., Yablonovitch, E., Cody, G. & Brooks, B. Limiting efficiency of silicon solar cells. *Electron Devices, IEEE Transactions on* **31,** 711–716 (June 1984).
9. Yoshikawa, K. *et al.* Exceeding conversion efficiency of 26 percent by heterojunction interdigitated back contact solar cell with thin film Si technology. *Solar Energy Materials and Solar Cells* **173.** Proceedings of the 7th international conference on Crystalline Silicon Photovoltaics, 37–42. ISSN: 0927-0248. https://www.sciencedirect.com/science/article/pii/S092702481730332X (2017).
10. IEA. World Energy Outlook 2020. https://www.iea.org/reports/world-energy-outlook-2020 (2020).
11. Tayebeh Ameri, N. L. & Brabecab, C. J. Highly efficient organic tandem solar cells: a follow up review. *Energy Environmental Science* **6** (May 2013).
12. S.Philipps, W. W. Photovoltaics report. https://www.ise.fraunhofer.de/content/dam/ise/de/documents/publications/studies/Photovoltaics-Report.pdf (Feb. 2023).
13. Saga, T. Advances in crystalline silicon solar cell technology for industrial mass production. *NPG Asia Materials* **2.** ISSN: 1884-4057. https://doi.org/10.1038/asiamat.2010.82 (2010).
14. Schwinde, S., Berg, M. & Kunert, M. New potential for reduction of kerf loss and wire consumption in multi-wire sawing. *Solar Energy Materials and Solar Cells* **136,** 44–47. ISSN: 0927-0248. https://www.sciencedirect.com/science/article/pii/S0927024814006679 (2015).
15. Matsui, T. *et al.* High-efficiency thin-film silicon solar cells realized by integrating stable a-Si:H absorbers into improved device design. *Japanese Journal of Applied Physics* **54,** 08KB10 (Aug. 2015).
16. laboratory, N. R. E. Does the world have enough materials for PV to help address climate change? https://www.nrel.gov/docs/fy05osti/37656.pdf (June 2005).
17. Solar, H. *Vopak and Hyet solar collaborate on 1MW Thin-Film Storage Tank Application* Apr. 2020. https://www.hyetsolar.com/news/vopak-and-hyet-solar-collaborate-on-1mw-thin-film-storage-tank-application/.
18. Solar, H. *Cost effective* https://www.hyetsolar.com/benefits/cost-effective-2/.
19. Solar, H. *Energy efficient* https://www.hyetsolar.com/news/energy-efficient/.
20. Solar, H. *LCOE Hyet Solar: Hyet solar* https://www.hyetsolar.com/cost-effective/.
21. Smets, A., Jäger, K., Isabella, O., van Swaaij, R. & Zeman, M. *Solar Energy: The physics and engineering of photovoltaic conversion, technologies and systems"* English. ISBN: 978-1-906860-32-5 (UIT Cambridge Limited, 2016).

22. Linge, C. A. R. Modeling of the Intermediate Band Tandem Solar Cell Using the AM1.5 Spectra. *Norwegian University of Science and Technology Department of Physics* (May 2011).
23. A.Neamen, D. *Semiconductor Physics and Devices* English. ISBN: 978-0-07-352958-5. https://www.academia.edu/83254025/Semiconductor_physics_and_devices_4th_edition_Neamen_Donald_ (Raghu Srinivasan, 2012).
24. Kang, H. Crystalline Silicon vs. Amorphous Silicon: the Significance of Structural Differences in Photovoltaic Applications. *IOP Conference Series: Earth and Environmental Science* **726,** 012001 (Apr. 2021).
25. Kang, H. Crystalline Silicon vs. Amorphous Silicon: the Significance of Structural Differences in Photovoltaic Applications. *IOP Conference Series: Earth and Environmental Science* **726,** 012001. https://dx.doi.org/10.1088/1755-1315/726/1/012001 (Apr. 2021).
26. Wagner, B. R. H. Potential of amorphous silicon for solar cells. **69,** 155–167. https://doi.org/10.1007/s003390050986 (Aug. 1999).
27. Zeman, M. *Thin film silicon solar cells* 2016. https://ocw.tudelft.nl/wp-content/uploads/Solar-Cells-R5-CH7_Thin_film_Si_solar_cells.pdf.
28. Yan, B., Yue, G., Yang, J. & Guha, S. On the bandgap of hydrogenated nanocrystalline silicon intrinsic materials used in thin film silicon solar cells. *Solar Energy Materials and Solar Cells* **111,** 90–96. ISSN: 0927-0248. https://www.sciencedirect.com/science/article/pii/S0927024812005843 (2013).
29. Shah, A. in *McEvoy's Handbook of Photovoltaics (Third Edition)* (ed Kalogirou, S. A.) Third Edition, 235–307 (Academic Press, 2018). ISBN: 978-0-12-809921-6. https://www.sciencedirect.com/science/article/pii/B9780128099216000082.
30. Schropp, R. in *Nanostructured Materials for Solar Energy Conversion* (ed Soga, T.) 131–166 (Elsevier, Amsterdam, 2006). ISBN: 978-0-444-52844-5. https://www.sciencedirect.com/science/article/pii/B9780444528445500068.
31. Doyle, J. R., Doughty, D. A. & Gallagher, A. Silane dissociation products in deposition discharges. *Journal of Applied Physics* **68,** 4375–4384. ISSN: 0021-8979. eprint: https://pubs.aip.org/aip/jap/article-pdf/68/9/4375/8015492/4375_1_online.pdf. https://doi.org/10.1063/1.346186 (Nov. 1990).
32. Van Elzakker, G. *Hydrogenated amorphous silicon solar cells deposited from silane diluted with hydrogen* 6-06-2010. http://resolver.tudelft.nl/uuid:c1ba2f21-65c9-4c22-9f70-54a0fd7cf4bb (2023).
33. Babal, P. *Doped nanocrystalline silicon oxide for use as (intermediate) reflecting layers in thin-film silicon solar cells* 29-10-2014. https://doi.org/10.4233/uuid:448b63f4-2128-409e-bbd8-866e720116ed (2023).
34. Bashir, A., Awan, T. I., Tehseen, A., Tahir, M. B. & Ijaz, M. in *Chemistry of Nanomaterials* (eds Awan, T. I., Bashir, A. & Tehseen, A.) 51–87 (Elsevier, 2020). ISBN: 978-0-12-818908-5. https://www.sciencedirect.com/science/article/pii/B9780128189085000032.
35. Feb. 2020. https://www.teamwavelength.com/photodiode-basics/.
36. Zielke, D. *Suppressing loss channels in the bulk and at the surface of crystalline silicon solar cells* PhD thesis (Oct. 2016). https://www.researchgate.net/publication/347086483_Suppressing_loss_channels_in_the_bulk_and_at_the_surface_of_crystalline_silicon_solar_cells#fullTextFileContent.
37. Hierrezuelo-Cardet, P. *et al.* External quantum efficiency measurements used to study the stability of differently deposited perovskite solar cells. *Journal of Applied Physics* **127,** 235501 (June 2020).
38. Cheng, T.-H. & Lin, S.-H. Detail Analysis of External Quantum Efficiency Measurement for Tandem Junction Solar Cells. *ECS Transactions* **64,** 47. https://dx.doi.org/10.1149/06415.0047ecst (Aug. 2014).
39. Van Swaaij, R. *1st lecture (PV measurement)* 2023. https://brightspace.tudelft.nl/d2l/le/content/499967/viewContent/3078058/View (2023).

40. Kudelski, A. Analytical applications of Raman spectroscopy. *Talanta* **76,** 1–8. ISSN: 0039-9140. https://www.sciencedirect.com/science/article/pii/S0039914008001641 (2008).
41. Fujiwara, H. & Collins, R. W. *Spectroscopic ellipsometry for photovoltaics* (Springer, 2018).
42. Zhou, W., Apkarian, R., Wang, Z. L. & Joy, D. Fundamentals of scanning electron microscopy (SEM). *Scanning microscopy for nanotechnology: techniques and applications,* 1–40 (2007).
43. Fischer, M. *et al.* High pressure processing of hydrogenated amorphous silicon solar cells: Relation between nanostructure and high open-circuit voltage. *Applied Physics Letters* **106,** 043905 (Jan. 2015).
44. Cashmore, J. S. *et al.* Record 12.34% stabilized conversion efficiency in a large area thin-film silicon tandem (MICROMORPH™) module. *Progress in Photovoltaics: Research and Applications* **23,** 1441–1447. eprint: https://onlinelibrary.wiley.com/doi/pdf/10.1002/pip.2642. https://onlinelibrary.wiley.com/doi/abs/10.1002/pip.2642 (2015).
45. Smets, A. H. M., Kessels, W. M. M. & van de Sanden, M. C. M. The effect of ion-surface and ion-bulk interactions during hydrogenated amorphous silicon deposition. *Journal of Applied Physics* **102,** 073523. ISSN: 0021-8979. eprint: https://pubs.aip.org/aip/jap/article-pdf/doi/10.1063/1.2786873/14996659/073523_1_online.pdf. https://doi.org/10.1063/1.2786873 (Oct. 2007).
46. Kawamura, E., Vahedi, V., Lieberman, M. A. & Birdsall, C. K. Ion energy distributions in rf sheaths; review, analysis and simulation. *Plasma Sources Science and Technology* **8,** R45. https://dx.doi.org/10.1088/0963-0252/8/3/202 (Aug. 1999).
47. Bugnon, G. *et al.* Silicon oxide buffer layer at the p–i interface in amorphous and microcrystalline silicon solar cells. *Solar Energy Materials and Solar Cells* **120,** 143–150. ISSN: 0927-0248. https://www.sciencedirect.com/science/article/pii/S092702481300442X (2014).
48. Kroll, U. *et al.* High-efficiency p-i-n a-Si:H solar cells with low boron cross-contamination prepared in a large-area single-chamber PECVD reactor. *Thin Solid Films* **451-452.** Proceedings of Symposium D on Thin Film and Nano-Structured Materials for Photovoltaics, of the E-MRS 2003 Spring Conference, 525–530. ISSN: 0040-6090. https://www.sciencedirect.com/science/article/pii/S0040609003015748 (2004).
49. Martinu, L., Zabeida, O. & Klemberg-Sapieha, J. in *Handbook of Deposition Technologies for Films and Coatings (Third Edition)* (ed Martin, P. M.) Third Edition, 392–465 (William Andrew Publishing, Boston, 2010). ISBN: 978-0-8155-2031-3. https://www.sciencedirect.com/science/article/pii/B9780815520313000090.
50. Kalpoe, P. *Transparent conductive oxide bi-layer as front contact for multijunction thin film silicon photovoltaic cells* 2023. http://resolver.tudelft.nl/uuid:f487531b-685f-4f2a-b59e-cd66ae7082ed.
51. Saitta, F. *et al. Transparent Conductive Oxide Bi-Layer as Front Contact for Multijunction Thin-Film Silicon Solar Cells* in *2023 IEEE 50th Photovoltaic Specialists Conference (PVSC)* (2023), 1–3.
52. Hendrix, L. *Optical modelling and characterization of transparent conductive oxides: Implementation of thin film solar cells* 2023. http://resolver.tudelft.nl/uuid:e66206dc-c72a-425b-a612-fd20ee17aa6d.
53. Springer, J. *et al.* Absorption loss at nanorough silver back reflector of thin-film silicon solar cells. *Journal of Applied Physics* **95** (Feb. 2004).
54. Padmakumar, G. & Smets, A. Texturing Methods on Glass for Enhanced Optical Performance in Indirect Band Gap Thin Film Solar Cells (2024).
55. de Vrijer, T. *et al.* The fundamental operation mechanisms of nc-SiOX≥0:H based tunnel recombination junctions revealed. *Solar Energy Materials and Solar Cells* **236,** 111501. ISSN: 0927-0248. https://www.sciencedirect.com/science/article/pii/S0927024821005390 (2022).
56. Iwahashi, T. *et al.* Silicon nitride anti-reflection coating on the glass and transparent conductive oxide interface for thin film solar cells and modules. *Journal of Applied Physics* **118,** 145302. ISSN: 0021-8979. eprint: https://pubs.aip.org/aip/jap/article-pdf/doi/10.1063/1.4932639/15170586/145302_1_online.pdf. https://doi.org/10.1063/1.4932639 (Oct. 2015).

Appendix A - JV-curves

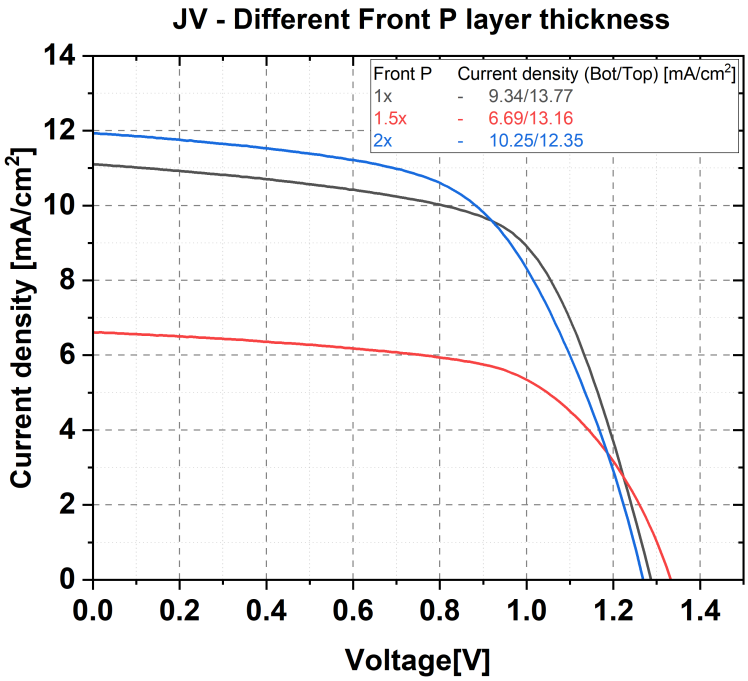

Figure A.1: JV-curves of the Asahi substrates with varying front p-layer thickness from experiment 8.

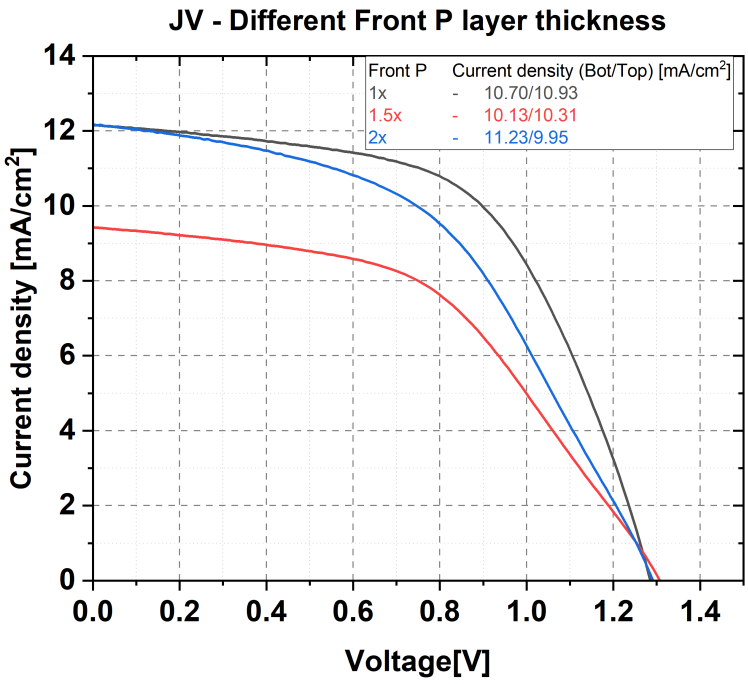

Figure A.2: JV-curves of the MST substrates with varying front p-layer thickness from experiment 8.

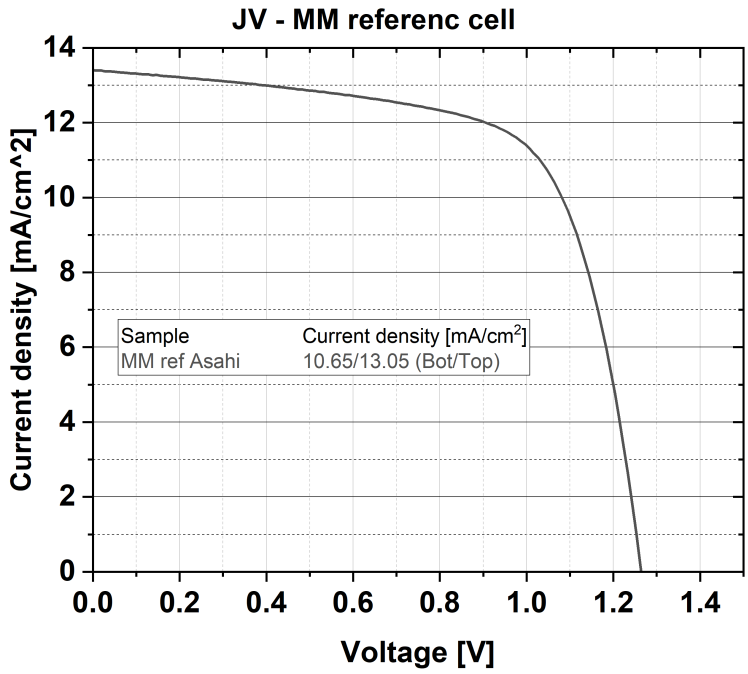

Figure A.3: JV-curve of the reference a-Si:H/nc-Si:H tandem cell from the run in which experiment 8 was done.

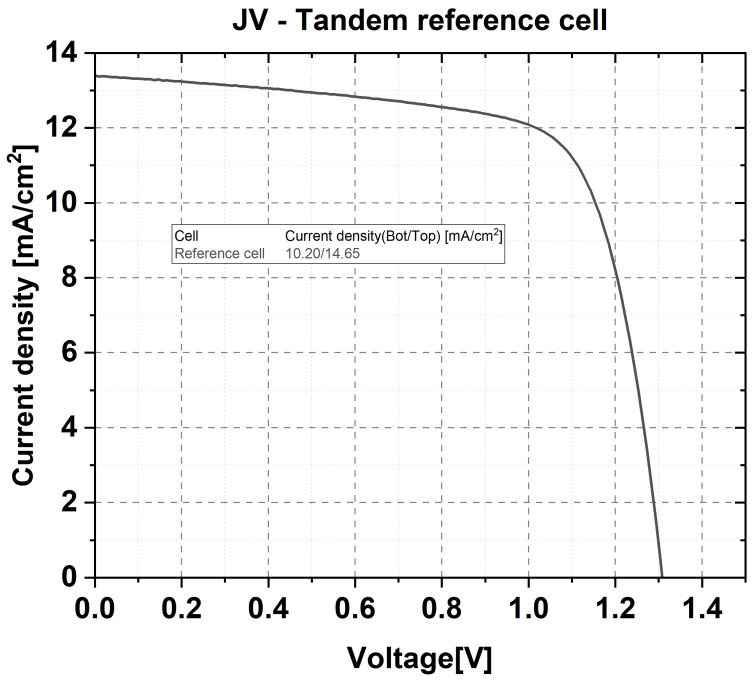

Figure A.4: JV-curve of the reference a-Si:H/nc-Si:H tandem cell from the run in which experiment 9 was done.

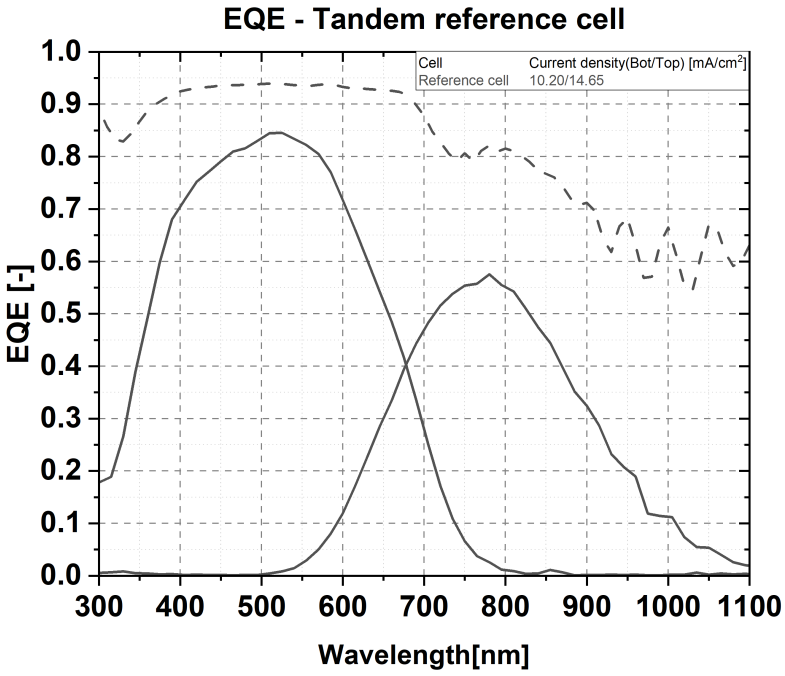

Figure A.5: EQE-measurement of the reference a-Si:H/nc-Si:H tandem cell from the run in which experiment 8 was done.

B

Appendix B - Processing parameters

B.1. Chapter 1 experiments

B.1.1. Experiment 1

DPC1(RF)	SiH4	B2H6/H2	B2H6/H2	CO2	H2	pressure	power	T_{heater}
unit	**[**$Sccm$**]**	**[**$Sccm$**]**	**[**$Sccm$**]**	**[**$Sccm$**]**	**[**$Sccm$**]**	**[**$mbar$**]**	**[**W**]**	**[**$C°$**]**
p1	0.8	0	50	1.2	170	2.2	12	300
p2	0.8	0	10	2.2	170	2.2	12	300
p3	0.8	0	0	2	170	2.2	12	300
DPC4(VHF)	**SiH4**	**H2**	**-**	**-**	**-**	**pressure**	**power**	**T_{heater}**
unit	**[**$Sccm$**]**	**[**$Sccm$**]**	**-**	**-**	**-**	**[**$mbar$**]**	**[**W**]**	**[**$C°$**]**
i-a-Si	6	60	0	0	0	4	40	170
DPC2(RF)	**SiH4**	**B2H6/H2**	**B2H6/H2**	**CO2**	**-**	**pressure**	**power**	**T_{heater}**
unit	**[**$Sccm$**]**	**[**$Sccm$**]**	**[**$Sccm$**]**	**[**$Sccm$**]**	**-**	**[**$mbar$**]**	**[**W**]**	**[**$C°$**]**
n1	40	11	0	0	0	0.6	4	300
n2	1	2	120	1.6	0	1.5	11	300
n3	1	2	120	0	0	1.5	11	300

Table B.1: Table with an overview of the full processing conditions of experiment 1, including all doped layers.

B.1.2. Experiment 2

DPC1(RF)	SiH4	B2H6/H2	B2H6/H2	CO2	H2	pressure	power	T_{heater}
unit	**[**$Sccm$**]**	**[**$Sccm$**]**	**[**$Sccm$**]**	**[**$Sccm$**]**	**[**$Sccm$**]**	**[**$mbar$**]**	**[**W**]**	**[**$C°$**]**
p1	0.8	0	50	1.2	170	2.2	12	300
p2	0.8	0	10	2.2	170	2.2	12	300
p3	0.8	0	0	2	170	2.2	12	300
DPC4(VHF)	**SiH4**	**H2**	**-**	**-**	**-**	**pressure**	**power**	**T_{heater}**
unit	**[**$Sccm$**]**	**[**$Sccm$**]**	**-**	**-**	**-**	**[**$mbar$**]**	**[**W**]**	**[**$C°$**]**
i-a-Si	6	54	0	0	0	5	28	170
DPC2(RF)	**SiH4**	**B2H6/H2**	**B2H6/H2**	**CO2**	**-**	**pressure**	**power**	**T_{heater}**
unit	**[**$Sccm$**]**	**[**$Sccm$**]**	**[**$Sccm$**]**	**[**$Sccm$**]**	**-**	**[**$mbar$**]**	**[**W**]**	**[**$C°$**]**
n1	40	11	0	0	0	0.6	4	300
n2	1	2	120	1.6	0	1.5	11	300
n3	1	2	120	0	0	1.5	11	300

Table B.2: Table with an overview of the full processing conditions of experiment 2, including all doped layers.

B.2. Chapter 2 experiments

B.2.1. Experiment 3

DPC1(RF)	SiH4	B2H6/H2	B2H6/H2	CO2	H2	pressure	power	T_{heater}
unit	**[**$Sccm$**]**	**[**$Sccm$**]**	**[**$Sccm$**]**	**[**$Sccm$**]**	**[**$Sccm$**]**	**[**$mbar$**]**	**[**W**]**	**[**$C°$**]**
p1	0.8	0	55	1.2	170	2.2	12	300
p2	0.8	0	10	2.2	170	2.2	12	300
p3	0.8	0	0	2	170	2.2	12	300
DPC4(VHF)	**SiH4**	**H2**	**SC**	**-**	**-**	**pressure**	**power**	**T_{heater}**
unit	**[**$Sccm$**]**	**[**$Sccm$**]**	**%**	**-**	**-**	**[**$mbar$**]**	**[**W**]**	**[**$C°$**]**
i-nc-Si (seed)	1.1	120	0.9	0	0	3.9	40	170
i-nc-Si (bulk)	3.2	120	2.6	0	0	3.9	40	170
DPC2(RF)	**SiH4**	**B2H6/H2**	**B2H6/H2**	**CO2**	**-**	**pressure**	**power**	**T_{heater}**
unit	**[**$Sccm$**]**	**[**$Sccm$**]**	**[**$Sccm$**]**	**[**$Sccm$**]**	**-**	**[**$mbar$**]**	**[**W**]**	**[**$C°$**]**
n1	40	11	0	0	0	0.6	4	300
n2	1	2	120	1.6	0	1.5	11	300
n3	1	2	120	0	0	1.5	11	300

Table B.3: Table with an overview of the full processing conditions of experiment 3, including all doped layers.

B.2.2. Experiment 4

DPC1(RF)	SiH4	B2H6/H2	B2H6/H2	CO2	H2	pressure	power	T_{heater}
unit	**[**$Sccm$**]**	**[**$Sccm$**]**	**[**$Sccm$**]**	**[**$Sccm$**]**	**[**$Sccm$**]**	**[**$mbar$**]**	**[**W**]**	**[**$C°$**]**
p1	0.8	0	55	1.2	170	2.2	12	300
p2	0.8	0	10	2.2	170	2.2	12	300
p3	0.8	0	0	2	170	2.2	12	300
DPC3(RF)	**SiH4**	**H2**	**-**	**-**	**-**	**pressure**	**power**	**T_{heater}**
unit	**[**$Sccm$**]**	**[**$Sccm$**]**	**-**	**-**	**-**	**[**$mbar$**]**	**[**W**]**	**[**$C°$**]**
i-a-Si (bulk)	40	0	0	0	0	0.7	2.8	300
DPC2(RF)	**SiH4**	**B2H6/H2**	**B2H6/H2**	**CO2**	**-**	**pressure**	**power**	**T_{heater}**
unit	**[**$Sccm$**]**	**[**$Sccm$**]**	**[**$Sccm$**]**	**[**$Sccm$**]**	**-**	**[**$mbar$**]**	**[**W**]**	**[**$C°$**]**
n1	40	11	0	0	0	0.6	4	300
n2	1	2	120	1.6	0	1.5	11	300
n3	1	2	120	0	0	1.5	11	300

Table B.4: Table with an overview of the full processing conditions of experiment 4, including all doped layers.

B.2.3. Experiment 5

DPC1(RF)	SiH4	B2H6/H2	B2H6/H2	CO2	H2	pressure	power	T_{heater}
unit	**[**$Sccm$**]**	**[**$Sccm$**]**	**[**$Sccm$**]**	**[**$Sccm$**]**	**[**$Sccm$**]**	**[**$mbar$**]**	**[**W**]**	**[**$C°$**]**
p1	0.8	0	55	1.2	170	2.2	12	300
p2	0.8	0	50	2.2	170	2.2	12	300
p3	0.8	0	0	2	170	2.2	12	300
DPC4(VHF)	**SiH4**	**H2**	**SC**	**-**	**-**	**pressure**	**power**	**T_{heater}**
unit	**[**$Sccm$**]**	**[**$Sccm$**]**	**%**	**-**	**-**	**[**$mbar$**]**	**[**W**]**	**[**$C°$**]**
i-nc-Si (seed)	1.1	120	0.9	0	0	3.9	40	170
i-nc-Si (bulk)	3	133	2.2	0	0	3.9	40	170
DPC2(RF)	**SiH4**	**B2H6/H2**	**B2H6/H2**	**CO2**	**-**	**pressure**	**power**	**T_{heater}**
unit	**[**$Sccm$**]**	**[**$Sccm$**]**	**[**$Sccm$**]**	**[**$Sccm$**]**	**-**	**[**$mbar$**]**	**[**W**]**	**[**$C°$**]**
n1	40	11	0	0	0	0.6	4	300
n2	1	2	120	1.6	0	1.5	11	300
n3	1	2	120	0	0	1.5	11	300

Table B.5: Table with an overview of the full processing conditions of experiment 5, including all doped layers.

B.2.4. Experiment 6

DPC1(RF)	SiH4	B2H6/H2	B2H6/H2	CO2	H2	pressure	power	T_{heater}
unit	**[**$Sccm$**]**	**[**$Sccm$**]**	**[**$Sccm$**]**	**[**$Sccm$**]**	**[**$Sccm$**]**	**[**$mbar$**]**	**[**W**]**	**[**$C°$**]**
p1	0.8	0	55	1.2	170	2.2	12	300
p2	0.8	0	50	2.2	170	2.2	12	300
p3	0.8	0	0	2	170	2.2	12	300
DPC4(VHF)	**SiH4**	**H2**	**SC**	**-**	**-**	**pressure**	**power**	**T_{heater}**
unit	**[**$Sccm$**]**	**[**$Sccm$**]**	**%**	**-**	**-**	**[**$mbar$**]**	**[**W**]**	**[**$C°$**]**
i-nc-Si (seed)	1.1	120	0.9	0	0	3.9	40	170
i-nc-Si (bulk)	3	133	2.2	0	0	3.9	40	170
DPC2(RF)	**SiH4**	**B2H6/H2**	**B2H6/H2**	**CO2**	**-**	**pressure**	**power**	**T_{heater}**
unit	**[**$Sccm$**]**	**[**$Sccm$**]**	**[**$Sccm$**]**	**[**$Sccm$**]**	**-**	**[**$mbar$**]**	**[**W**]**	**[**$C°$**]**
n1	40	11	0	0	0	0.6	4	300
n2	1	2	120	1.6	0	1.5	11	300
n3	1	2	120	0	0	1.5	11	300

Table B.6: Table with an overview of the full processing conditions of experiment 6, including all doped layers.

B.3. Chapter 3 experiments

B.3.1. Experiment 7

DPC1(RF)	**SiH4**	**B2H6/H2**	**B2H6/H2**	**CO2**	**H2**	**pressure**	**power**	**T_{heater}**
unit	**[**$Sccm$**]**	**[**$Sccm$**]**	**[**$Sccm$**]**	**[**$Sccm$**]**	**[**$Sccm$**]**	**[**$mbar$**]**	**[**W**]**	**[**$C°$**]**
p1	0.8	0	55	1.2	170	2.2	12	300
p2	0.8	0	10	2.2	170	2.2	12	300
p3	0.8	0	0	2	170	2.2	12	300
DPC3(RF)	**SiH4**	**H2**	**-**	**-**	**-**	**pressure**	**power**	**T_{heater}**
unit	**[**$Sccm$**]**	**[**$Sccm$**]**	**-**	**-**	**-**	**[**$mbar$**]**	**[**W**]**	**[**$C°$**]**
i-a-Si	40	0	0	0	0	0.7	2.8	300
DPC2(RF)	**SiH4**	**B2H6/H2**	**B2H6/H2**	**CO2**	**-**	**pressure**	**power**	**T_{heater}**
unit	**[**$Sccm$**]**	**[**$Sccm$**]**	**[**$Sccm$**]**	**[**$Sccm$**]**	**-**	**[**$mbar$**]**	**[**W**]**	**[**$C°$**]**
n1	40	11	0	0	0	0.6	4	300
n2	1	2	120	1.6	0	1.5	11	300
DPC1(RF)	**SiH4**	**B2H6/H2**	**B2H6/H2**	**CO2**	**H2**	**pressure**	**power**	**T_{heater}**
unit	**[**$Sccm$**]**	**[**$Sccm$**]**	**[**$Sccm$**]**	**[**$Sccm$**]**	**[**$Sccm$**]**	**[**$mbar$**]**	**[**W**]**	**[**$C°$**]**
p1	0.8	0	55	2.2	170	2.2	12	300
p2	0.8	0	10	2.2	170	2.2	12	300
p3	0.8	0	0	1.6	170	2.2	12	300
DPC4(VHF)	**SiH4**	**H2**	**SC**	**-**	**-**	**pressure**	**power**	**T_{heater}**
unit	**[**$Sccm$**]**	**[**$Sccm$**]**	**%**	**-**	**-**	**[**$mbar$**]**	**[**W**]**	**[**$C°$**]**
i-nc-Si(seed)	1.1	120	0.9	0	0	4	40	170
i-nc-Si(bulk)	3.2	120	2.6	0	0	4	40	170
DPC2(RF)	**SiH4**	**B2H6/H2**	**B2H6/H2**	**CO2**	**-**	**pressure**	**power**	**T_{heater}**
unit	**[**$Sccm$**]**	**[**$Sccm$**]**	**[**$Sccm$**]**	**[**$Sccm$**]**	**-**	**[**$mbar$**]**	**[**W**]**	**[**$C°$**]**
n1	40	11	0	0	0	0.6	4	300
n2	1	2	120	1.6	0	1.5	11	300
n3	1	2	120	0	0	1.5	11	300

Table B.7: Table with an overview of the full processing conditions of experiment 7, including all doped layers.

B.3.2. Experiment 8

DPC1(RF)	**SiH4**	**B2H6/H2**	**B2H6/H2**	**CO2**	**H2**	**pressure**	**power**	**T_{heater}**
unit	**[$Sccm$]**	**[$Sccm$]**	**[$Sccm$]**	**[$Sccm$]**	**[$Sccm$]**	**[$mbar$]**	**[W]**	**[$C°$]**
p1	0.8	0	55	1.2	170	2.2	12	300
p2	0.8	0	10	2.2	170	2.2	12	300
p3	0.8	0	0	2	170	2.2	12	300
DPC3(RF)	**SiH4**	**H2**	**-**	**-**	**-**	**pressure**	**power**	**T_{heater}**
unit	**[$Sccm$]**	**[$Sccm$]**	**-**	**-**	**-**	**[$mbar$]**	**[W]**	**[$C°$]**
i-a-Si	40	0	0	0	0	0.7	2.8	300
DPC2(RF)	**SiH4**	**B2H6/H2**	**B2H6/H2**	**CO2**	**-**	**pressure**	**power**	**T_{heater}**
unit	**[$Sccm$]**	**[$Sccm$]**	**[$Sccm$]**	**[$Sccm$]**	**-**	**[$mbar$]**	**[W]**	**[$C°$]**
n1	40	11	0	0	0	0.6	4	300
n2	1	2	120	1.6	0	1.5	11	300
DPC1(RF)	**SiH4**	**B2H6/H2**	**B2H6/H2**	**CO2**	**H2**	**pressure**	**power**	**T_{heater}**
unit	**[$Sccm$]**	**[$Sccm$]**	**[$Sccm$]**	**[$Sccm$]**	**[$Sccm$]**	**[$mbar$]**	**[W]**	**[$C°$]**
p1	0.8	0	55	2.2	170	2.2	12	300
p2	0.8	0	10	2.2	170	2.2	12	300
p3	0.8	0	0	1.6	170	2.2	12	300
DPC4(VHF)	**SiH4**	**H2**	**SC**	**-**	**-**	**pressure**	**power**	**T_{heater}**
unit	**[$Sccm$]**	**[$Sccm$]**	**%**	**-**	**-**	**[$mbar$]**	**[W]**	**[$C°$]**
i-nc-Si(seed)	1.1	120	0.9	0	0	4	40	170
i-nc-Si(bulk)	3	140	2.1	0	0	4	40	170
DPC2(RF)	**SiH4**	**B2H6/H2**	**B2H6/H2**	**CO2**	**-**	**pressure**	**power**	**T_{heater}**
unit	**[$Sccm$]**	**[$Sccm$]**	**[$Sccm$]**	**[$Sccm$]**	**-**	**[$mbar$]**	**[W]**	**[$C°$]**
n1	40	11	0	0	0	0.6	4	300
n2	1	2	120	1.6	0	1.5	11	300
n3	1	2	120	0	0	1.5	11	300

Table B.8: Table with an overview of the full processing conditions of experiment 8, including all doped layers.

B.3.3. Experiment 9

DPC1(RF)	**SiH4**	**B2H6/H2**	**B2H6/H2**	**CO2**	**H2**	**pressure**	**power**	**T_{heater}**
unit	**[**$Sccm$**]**	**[**$Sccm$**]**	**[**$Sccm$**]**	$Sccm$	**[**$Sccm$**]**	**[**$mbar$**]**	**[**W**]**	**[**$C°$**]**
p1	0.8	0	55	1.2	170	2.2	12	300
p2	0.8	0	10	2.2	170	2.2	12	300
p3	0.8	0	0	2	170	2.2	12	300
DPC3(RF)	**SiH4**	**H2**	**-**	**-**	**-**	**pressure**	**power**	**T_{heater}**
unit	**[**$Sccm$**]**	**[**$Sccm$**]**	**-**	**-**	**-**	**[**$mbar$**]**	**[**W**]**	**[**$C°$**]**
i-a-Si	40	0	0	0	0	0.7	2.8	300
DPC2(RF)	**SiH4**	**B2H6/H2**	**B2H6/H2**	**CO2**	**-**	**pressure**	**power**	**T_{heater}**
unit	**[**$Sccm$**]**	**[**$Sccm$**]**	**[**$Sccm$**]**	**[**$Sccm$**]**	**-**	**[**$mbar$**]**	**[**W**]**	**[**$C°$**]**
n1	40	11	0	0	0	0.6	4	300
n2	1	2	120	1.6	0	1.5	11	300
DPC1(RF)	**SiH4**	**B2H6/H2**	**B2H6/H2**	**CO2**	**H2**	**pressure**	**power**	**T_{heater}**
unit	**[**$Sccm$**]**	**[**$Sccm$**]**	**[**$Sccm$**]**	**[**$Sccm$**]**	**[**$Sccm$**]**	**[**$mbar$**]**	**[**W**]**	**[**$C°$**]**
p1	0.8	0	55	2.2	170	2.2	12	300
p2	0.8	0	10	2.2	170	2.2	12	300
p3	0.8	0	0	1.6	170	2.2	12	300
DPC4(VHF)	**SiH4**	**H2**	**SC**	**-**	**-**	**pressure**	**power**	**T_{heater}**
unit	**[**$Sccm$**]**	**[**$Sccm$**]**	**%**	**-**	**-**	**[**$mbar$**]**	**[**W**]**	**[**$C°$**]**
i-nc-Si(seed)	1.1	120	0.9	0	0	4	40	170
i-nc-Si(bulk)	3	133	2.2	0	0	4	40	170
DPC2(RF)	**SiH4**	**B2H6/H2**	**B2H6/H2**	**CO2**	**-**	**pressure**	**power**	**T_{heater}**
unit	**[**$Sccm$**]**	**[**$Sccm$**]**	**[**$Sccm$**]**	**[**$Sccm$**]**	**-**	**[**$mbar$**]**	**[**W**]**	**[**$C°$**]**
n1	40	11	0	0	0	0.6	4	300
n2	1	2	120	1.6	0	1.5	11	300
n3	1	2	120	0	0	1.5	11	300

Table B.9: Table with an overview of the full processing conditions of experiment 9, including all doped layers.

C

Appendix C - Anti-reflection coating parameters

C.1. Data SiN_x

C.1.1. n (refractive index) data

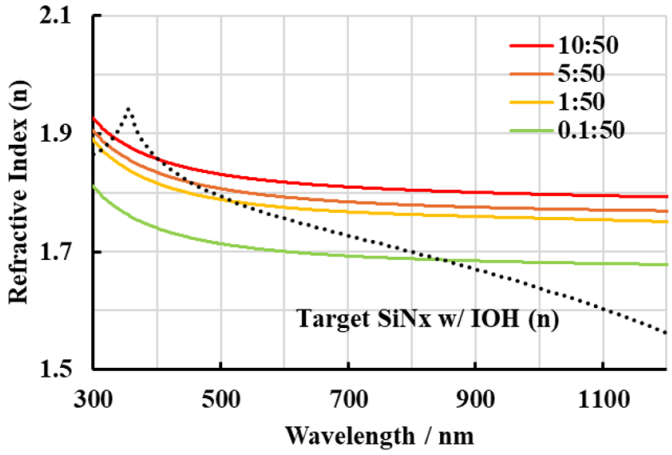

Figure C.1: N data and the target line as the black dotted line, measured by Leo Adachi on the SiN_x.

C.1.2. k (extinction coefficient) data

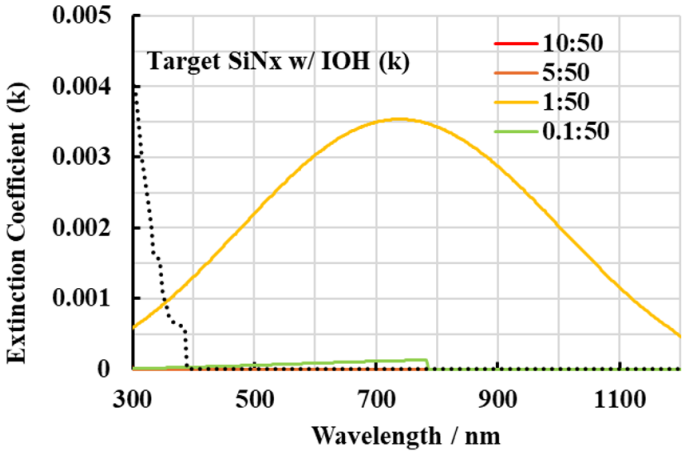

Figure C.2: K data and the target line as the black dotted line, measured by Leo Adachi on the SiN_x.

Appendix D - Normalised Raman spectroscopy plots

D.0.1. Normalised Raman plots Experiment 3

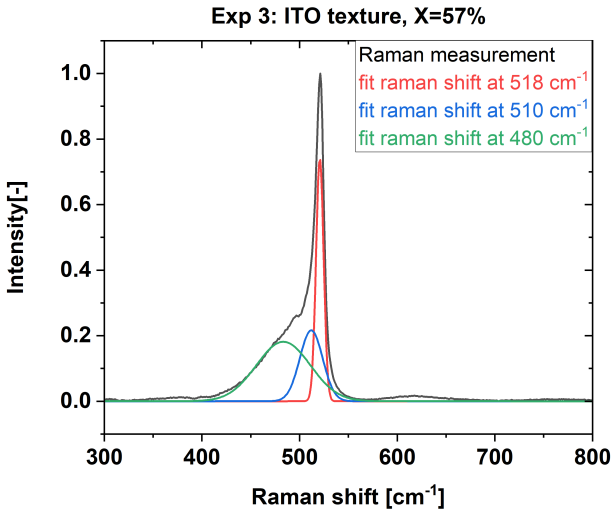

Figure D.1: Normalised Raman plot of ITO texture from experiment 3.

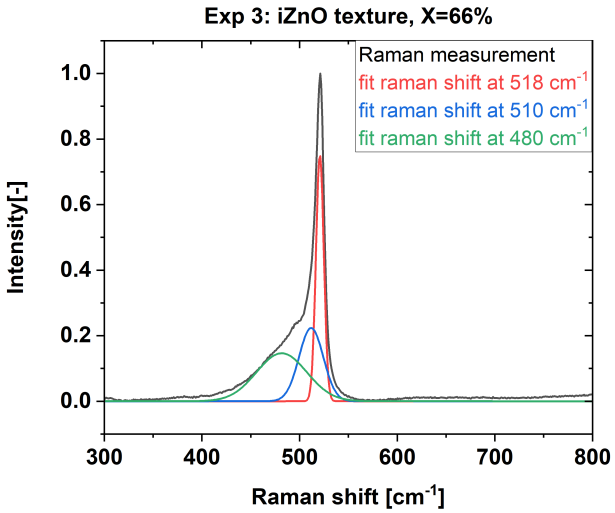

Figure D.2: Normalised Raman plot of iZnO texture from experiment 3.

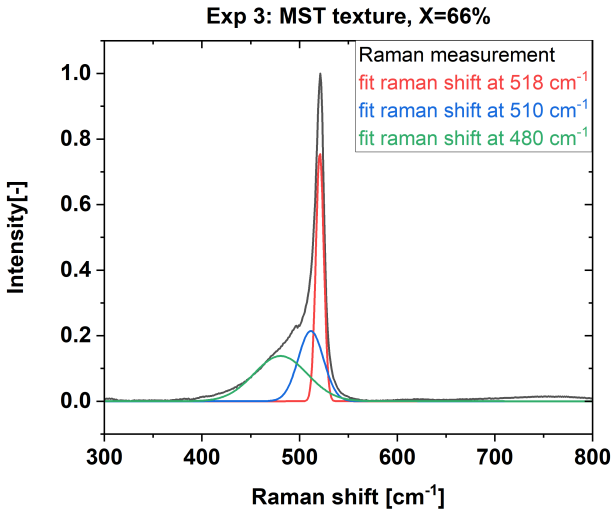

Figure D.3: Normalised Raman plot of MST texture from experiment 3.

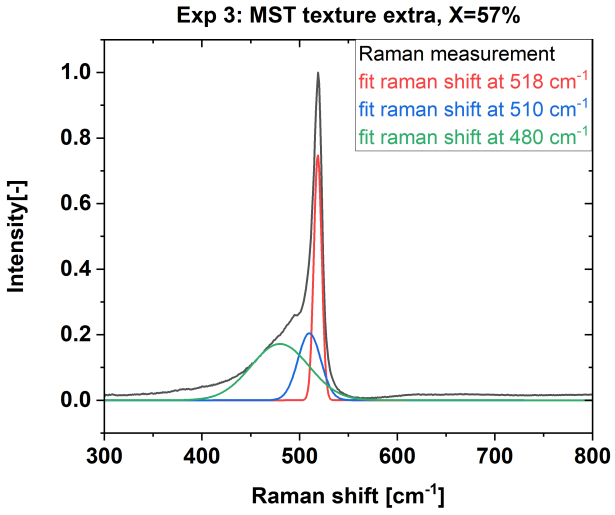

Figure D.4: Normalised Raman plot of the extra MST texture from experiment 3.

D.0.2. Normalised Raman plots Experiment 5

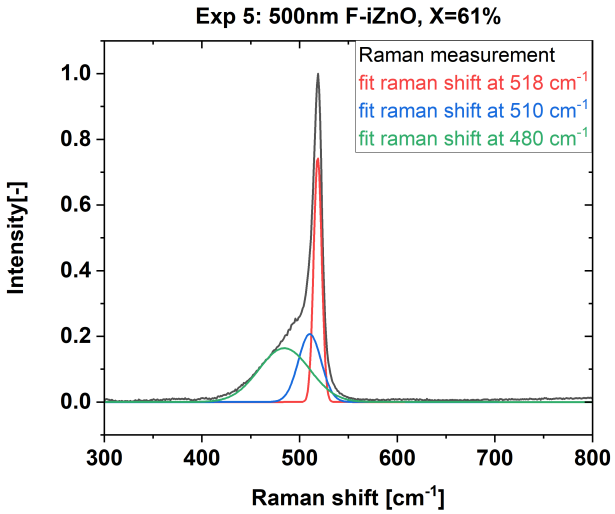

Figure D.5: Normalised Raman plot of the 500nm iZnO sample from experiment 5.

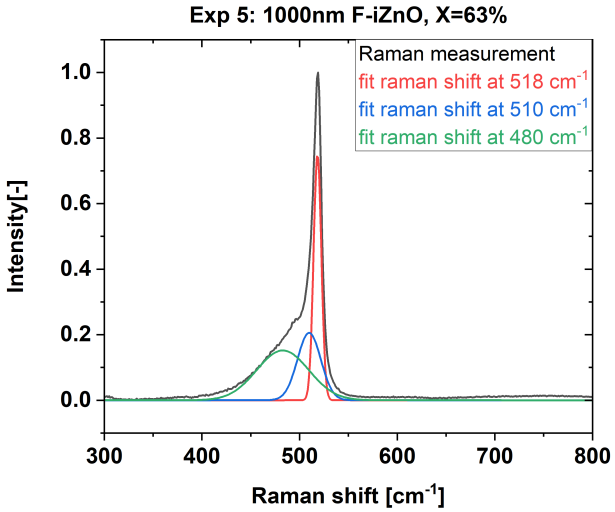

Figure D.6: Normalised Raman plot of the 1000nm iZnO sample from experiment 5.

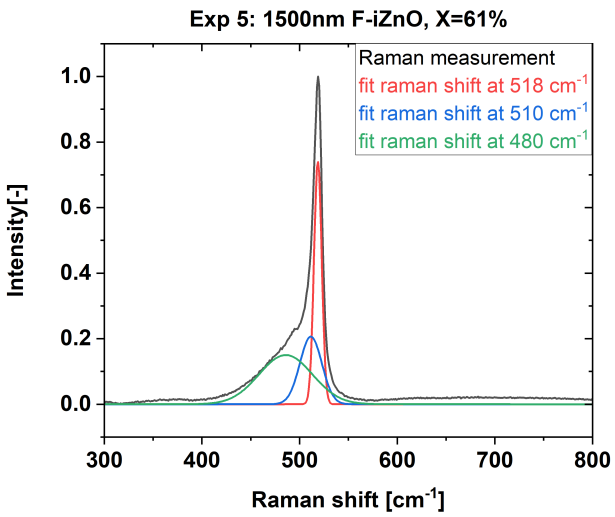

Figure D.7: Normalised Raman plot of the 1500nm iZnO sample from experiment 5.

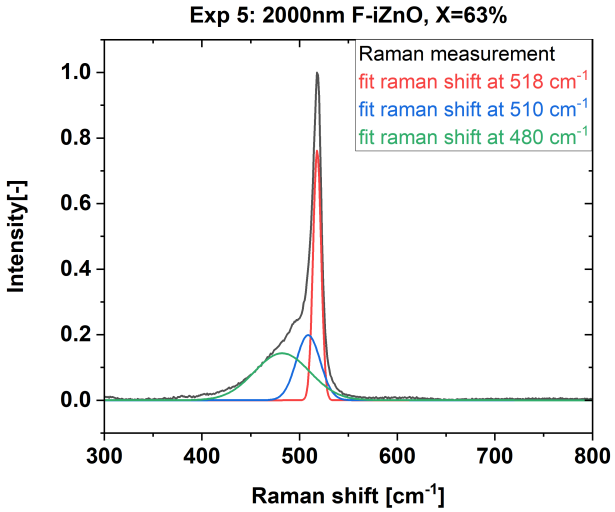

Figure D.8: Normalised Raman plot of the 2000nm iZnO sample from experiment 5.

D.0.3. Normalised Raman plots Experiment 6

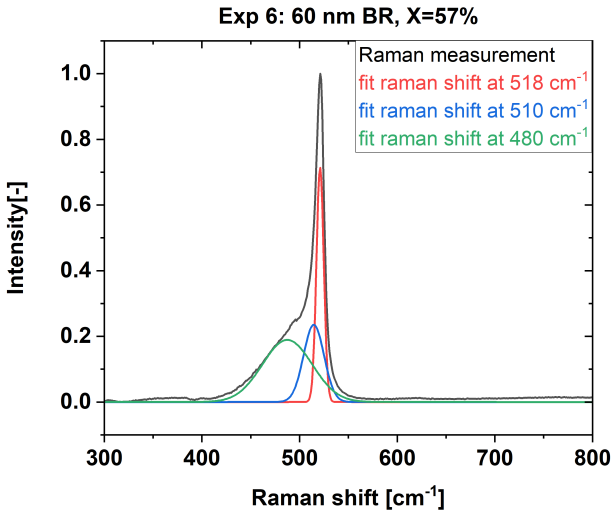

Figure D.9: Normalised Raman plot of the 60nm iZnO as back reflector sample from experiment 6.

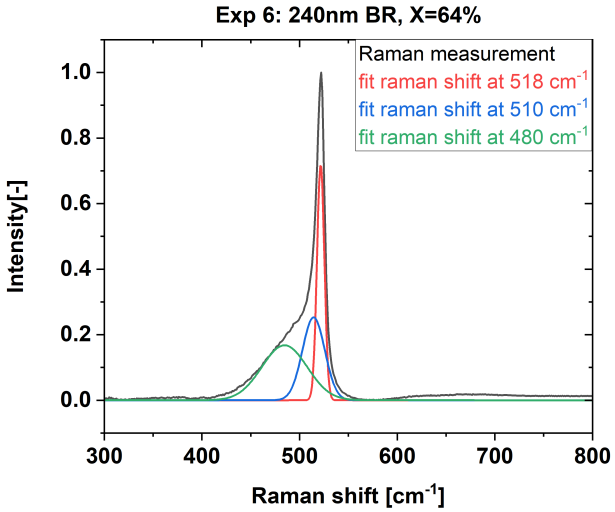

Figure D.10: Normalised Raman plot of the 2400nm iZnO as back reflector sample from experiment 6.

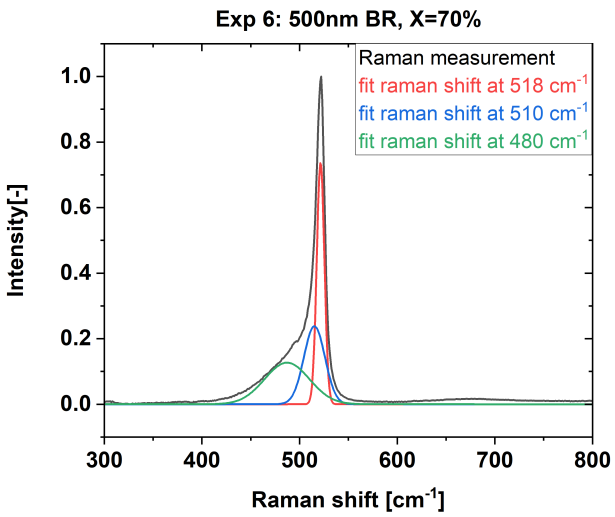

Figure D.11: Normalised Raman plot of the 500nm iZnO as back reflector sample from experiment 6.

D.0.4. Normalised Raman plots Experiment 7

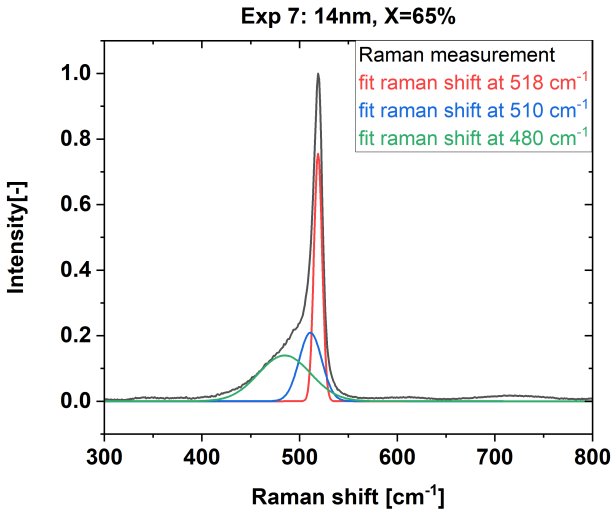

Figure D.12: Normalised Raman plot of the 14nm p-layer in the TRJ sample from experiment 7.

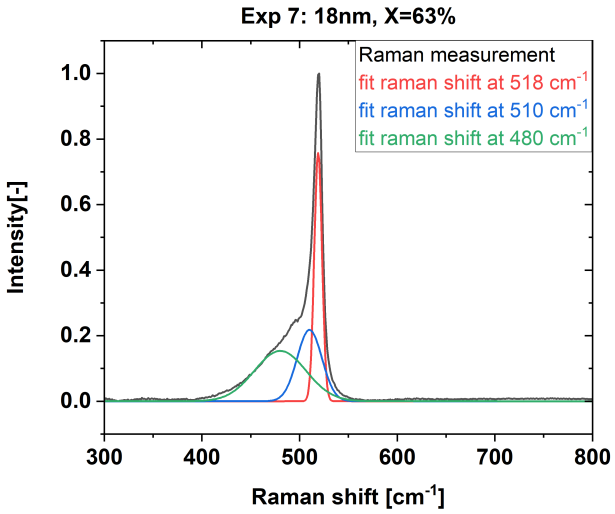

Figure D.13: Normalised Raman plot of the 18nm p-layer in the TRJ sample from experiment 7.

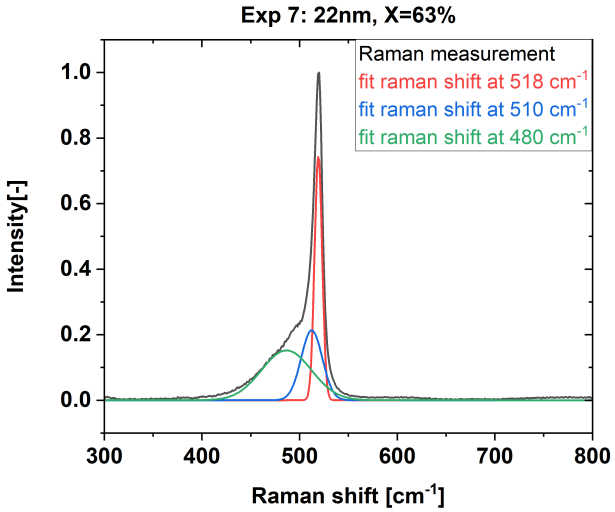

Figure D.14: Normalised Raman plot of the 22nm p-layer in the TRJ sample from experiment 7.

D.0.5. Normalised Raman plots Experiment 8

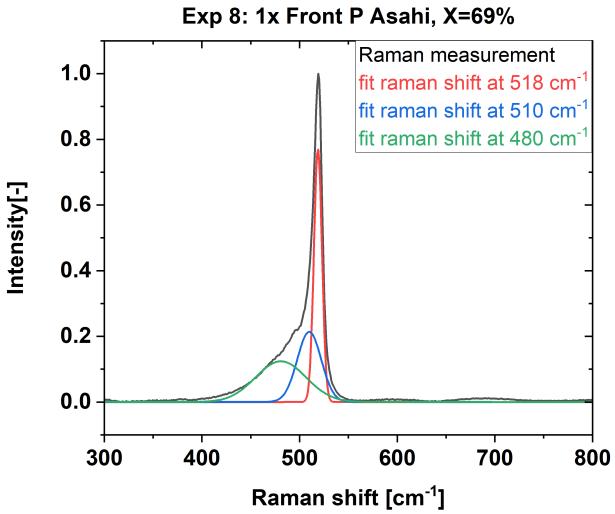

Figure D.15: Normalised Raman plot of the 1x front p-layer on Asahi from experiment 8.

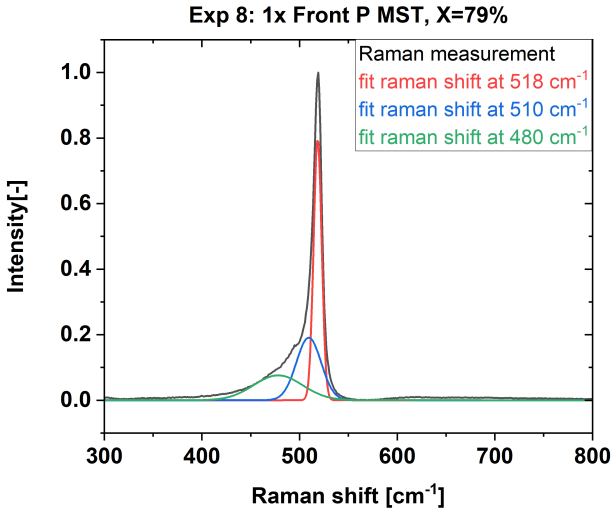

Figure D.16: Normalised Raman plot of the 1x front p-layer on MST from experiment 8.

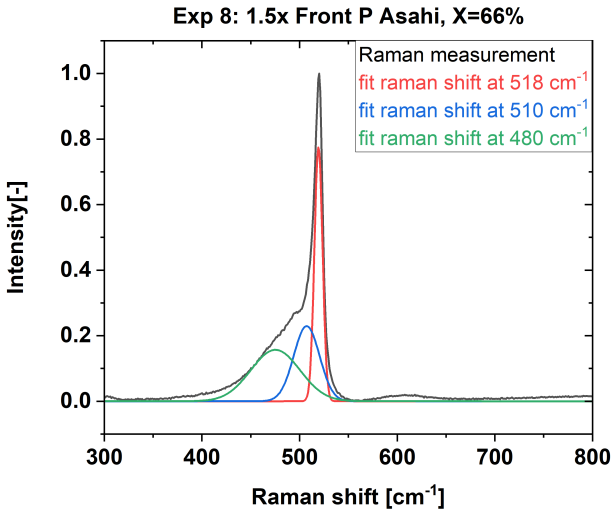

Figure D.17: Normalised Raman plot of the 1.5x front p-layer on Asahi from experiment 8.

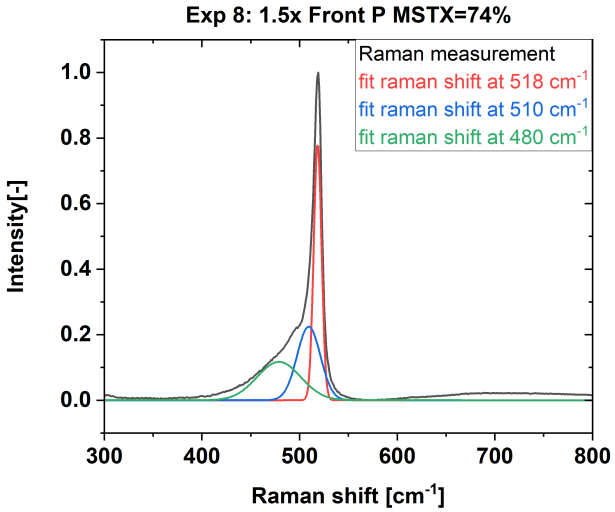

Figure D.18: Normalised Raman plot of the 1.5x front p-layer on MST from experiment 8.

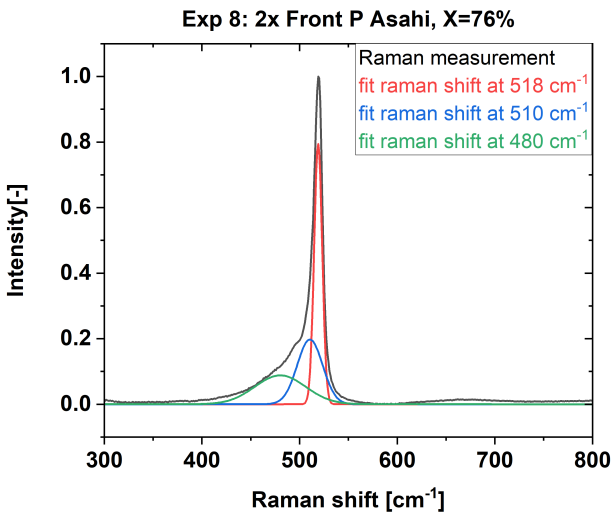

Figure D.19: Normalised Raman plot of the 2x front p-layer on Asahi from experiment 8.

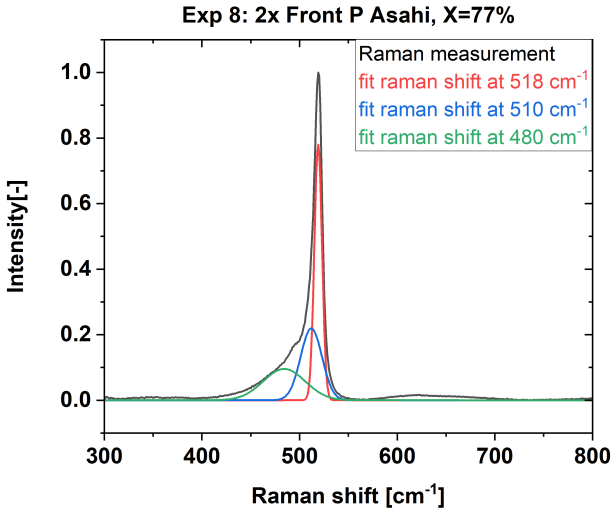

Figure D.20: Normalised Raman plot of the 2x front p-layer on MST from experiment 8.

D.0.6. Normalised Raman plots Experiment 9

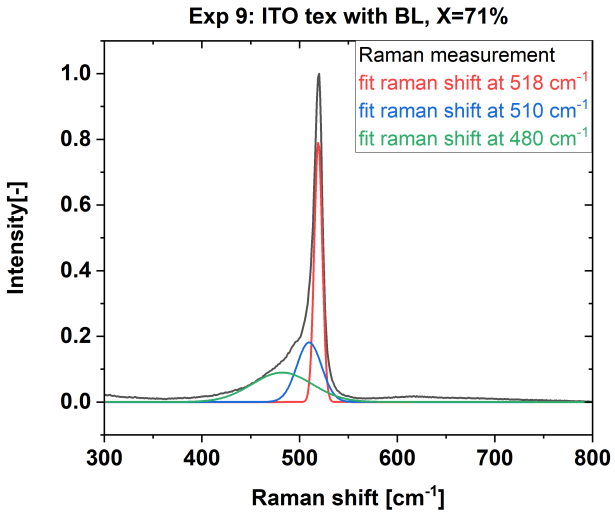

Figure D.21: Normalised Raman plot of ITO texture with bilayer TCO from experiment 9.

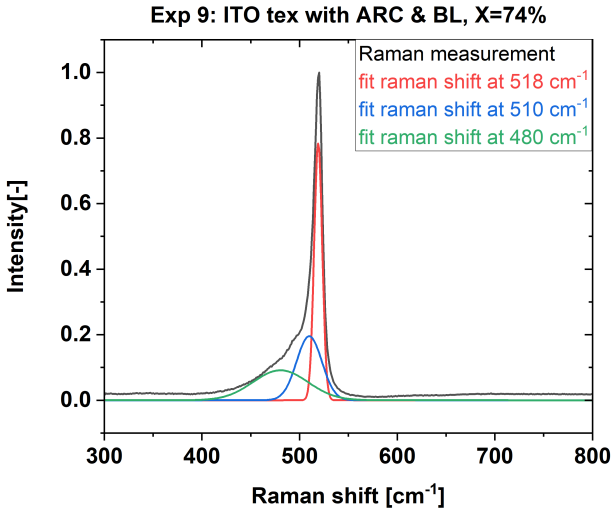

Figure D.22: Normalised Raman plot of ITO texture with bilayer and ARC TCO from experiment 9.

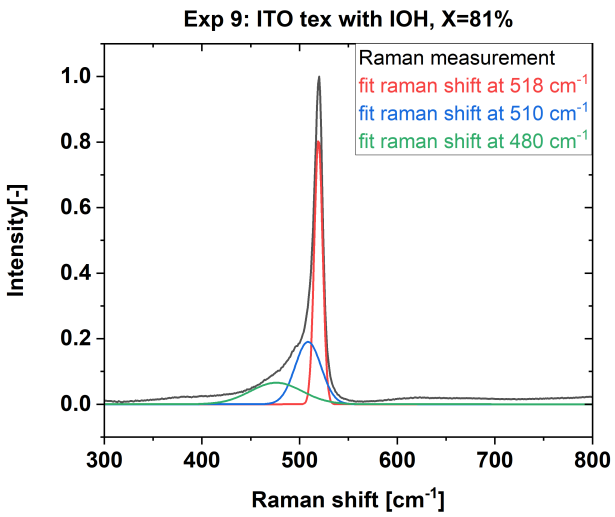

Figure D.23: Normalised Raman plot of ITO texture with single layer TCO from experiment 9.

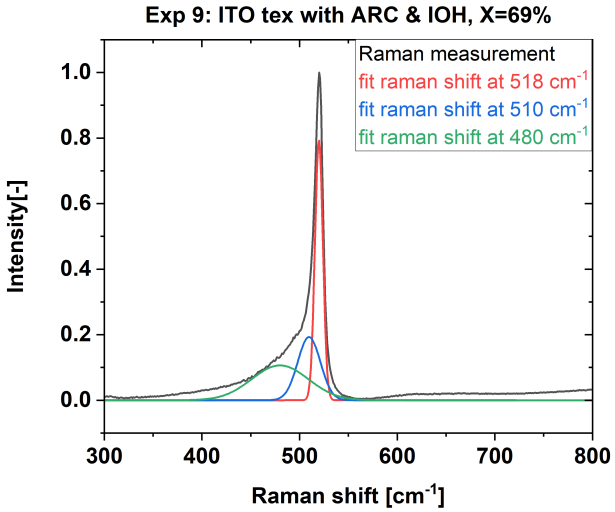

Figure D.24: Normalised Raman plot of ITO texture with single layer TCO and ARC from experiment 9.

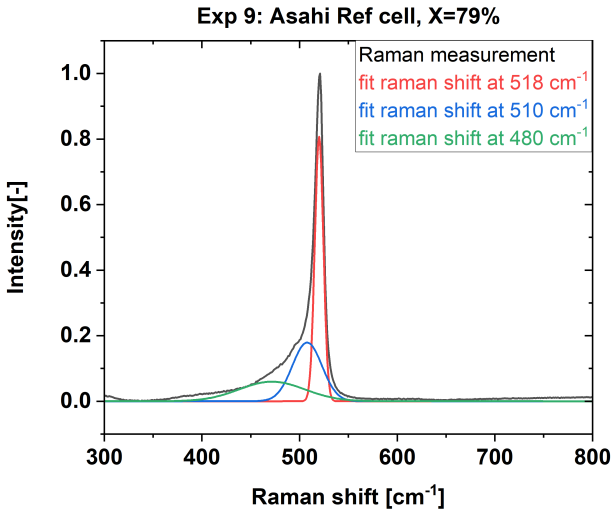

Figure D.25: Normalised Raman plot of reference a-Si:H/nc-Si:H cell on Asahi from experiment 9.

Appendix E - Images

E.0.1. Image of the MST textured samples next to the Asahi samples from experiment 8

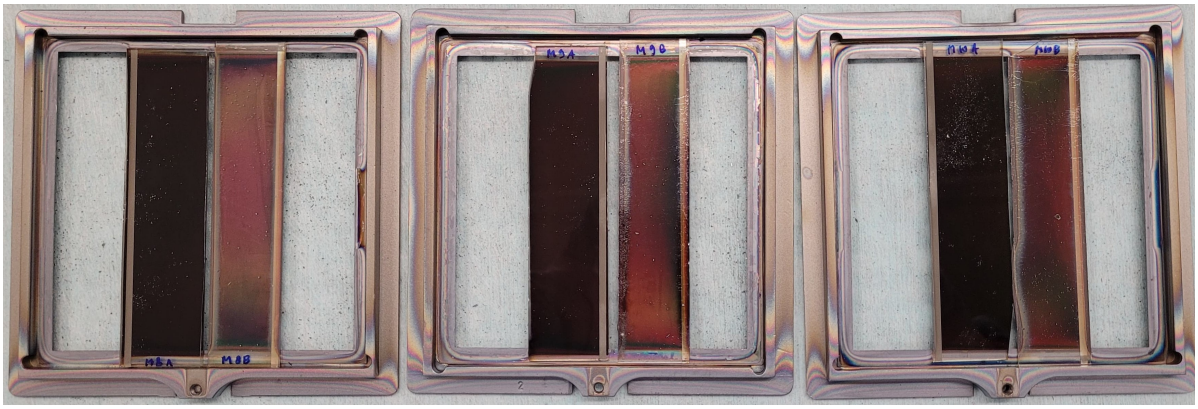

Figure E.1: Image showing a metallic like deposition on the front side of the MST textured substrates from experiment 8.